2014-09

A new approach for optimizing image collection from space

King, Jeffery T.

Monterey, California: Naval Postgraduate School

http://hdl.handle.net/10945/49613

NAVAL
POSTGRADUATE
SCHOOL

MONTEREY, CALIFORNIA

DISSERTATION

A NEW APPROACH FOR OPTIMIZING IMAGE COLLECTION FROM SPACE

by

Jeffery T. King

September 2014

Dissertation Supervisor: I. Michael Ross

Approved for public release; distribution is unlimited

THIS PAGE INTENTIONALLY LEFT BLANK

REPORT DOCUMENTATION PAGE	*Form Approved OMB No. 0704–0188*

1. AGENCY USE ONLY *(Leave Blank)*	**2. REPORT DATE** 09-26-2014	**3. REPORT TYPE AND DATES COVERED** Dissertation 2102-06-01—2104-09-26

4. TITLE AND SUBTITLE
A NEW APPROACH FOR OPTIMIZING IMAGE COLLECTION FROM SPACE

5. FUNDING NUMBERS

6. AUTHOR(S)
Jeffery T. King

7. PERFORMING ORGANIZATION NAME(S) AND ADDRESS(ES)
Naval Postgraduate School
Monterey, CA 93943

8. PERFORMING ORGANIZATION REPORT NUMBER

9. SPONSORING / MONITORING AGENCY NAME(S) AND ADDRESS(ES)
N/A

10. SPONSORING / MONITORING AGENCY REPORT NUMBER

11. SUPPLEMENTARY NOTES

The views expressed in this document are those of the author and do not reflect the official policy or position of the Department of Defense or the U.S. Government. IRB Protocol Number: N/A.

12a. DISTRIBUTION / AVAILABILITY STATEMENT
Approved for public release; distribution is unlimited

12b. DISTRIBUTION CODE

13. ABSTRACT *(maximum 200 words)*

The capability of space-based sensors to collect images is directly related to the agility of the sensor. Increasing the sensor agility can be accomplished using optimal control; however, planning for the increased performance is required in order to increase the overall collection capability of a system. This dissertation demonstrates how optimal control yields a higher agility for a given spacecraft system, and presents a new and simple method to estimate the performance increase. New targeting equations are developed that define the sensor attitude, rate and acceleration required to collect a moving target. Operational maneuvers are defined and generated using optimal control. Finally, a new formulation for the time-varying image collection planning problem is presented by combining graph theory with optimal control into a hybrid optimal control architecture.

14. SUBJECT TERMS
targeting, collection planning, hybrid optimal control, time-varying, agilitoid, orienteering problem, maneuver planning, satellite

15. NUMBER OF PAGES 167

16. PRICE CODE

17. SECURITY CLASSIFICATION OF REPORT Unclassified	**18. SECURITY CLASSIFICATION OF THIS PAGE** Unclassified	**19. SECURITY CLASSIFICATION OF ABSTRACT** Unclassified	**20. LIMITATION OF ABSTRACT** UU

THIS PAGE INTENTIONALLY LEFT BLANK

A NEW APPROACH FOR OPTIMIZING IMAGE COLLECTION FROM SPACE

Jeffery T. King
Commander, United States Navy
B.S., U.S. Naval Academy, 1993
M.S., Naval Postgraduate School, 2002

Submitted in partial fulfillment of the
requirements for the degree of

DOCTOR OF PHILOSOPHY IN ASTRONAUTICAL ENGINEERING

from the

NAVAL POSTGRADUATE SCHOOL
September 2014

Author: Jeffery T. King

Approved by:

I. Michael Ross
Professor of Mechanical and
Aerospace Engineering
Dissertation Supervisor

Isaac Kaminer
Professor of Mechanical and
Aerospace Engineering

Mark Karpenko
Research Assistant Professor,
Mechanical and Aerospace
Engineering

Wei Kang
Professor of Applied
Mathematics

Jim Newman
Professor of Space Systems

Approved by: Garth V. Hobson
Chair, Department of Mechanical and Aerospace Engineering

Approved by: Douglas Moses
Vice Provost for Academic Affairs

THIS PAGE INTENTIONALLY LEFT BLANK

ABSTRACT

The capability of space-based sensors to collect images is directly related to the agility of the sensor. Increasing the sensor agility can be accomplished using optimal control; however, planning for the increased performance is required in order to increase the overall collection capability of a system. This dissertation demonstrates how optimal control yields a higher agility for a given spacecraft system, and presents a new and simple method to estimate the performance increase. New targeting equations are developed that define the sensor attitude, rate and acceleration required to collect a moving target. Operational maneuvers are defined and generated using optimal control. Finally, a new formulation for the time-varying image collection planning problem is presented by combining graph theory with optimal control into a hybrid optimal control architecture.

THIS PAGE INTENTIONALLY LEFT BLANK

Table of Contents

List of Figures

THIS PAGE INTENTIONALLY LEFT BLANK

List of Tables

THIS PAGE INTENTIONALLY LEFT BLANK

List of Acronyms and Abbreviations

BB	bang-bang
BoB	bang-off-bang
BVF	benefit value function
CCD	charged-coupled device
COE	classical orbital elements
DCM	direction cosine matrix
EO	electro-optical
ISM	industry standard maneuver
IR	infrared
LOS	line of sight
MIP	mixed integer problem
NR2NR	non-rest to non-rest
OC	optimal control
OP	orienteering problem
RW	reaction wheel
R2R	rest-to-rest
STM	shortest time maneuver
TOP	team orienteering problem
TDI	time delay integration
TSP	traveling salesman problem

UAV	unmanned aerial vehicle

Executive Summary

The agility of a space-based system has a very strong effect on the capability to collect images. Increasing spacecraft agility can be accomplished using optimal control. Current planning methods are incapable of utilizing the increased performance from optimal control maneuvering. This dissertation demonstrated how optimal control can yield a higher agility for a given system and further proposed a new formulation for optimal collection planning. The agility performance benefit, in slew maneuver time saved, seen by using optimal control maneuvers ranged between 16 and 30 percent for the example spacecraft.

A new way to analyze the agility of a system was presented that calculated the agility envelope, or agilitoid. An original figure of merit, γ, was derived to estimate the benefit of using optimal control versus an industry standard maneuvering algorithm. This figure of merit was validated with over 1500 maneuvers across a variety of different conditions. New targeting equations were developed that define the sensor conditions required to collect an image. These equations accommodate stationary or moving point targets as well as area scans using a scanning sensor. Most maneuvers in literature assume zero rates and are not operationally relevant. Operational minimum time maneuvers with non-zero initial and final rates were designed using optimal control for the first time in literature.

The concept of γ can be applied in two primary ways. First, if a system is already deployed, γ represents the average performance increase that can be expected from the current system by using optimal control maneuvering. In other words, optimal control maneuvering yields the same average performance a larger version of the current system (torque and momentum), multiplied by γ, would achieve. For the example system, the value of γ was 1.41, though results will vary because the agilitoid is unique in shape and size to the system configuration and maneuvering algorithm.

The second way to apply the γ concept is in the system design phase or pre-deployment. The γ represents the average decrease in size, weight, and power in reaction wheels using optimal control that can be expected to achieve the current performance level. In other words, optimal control may allow a design to meet the performance goals while saving size, weight, or power by $1/\gamma$. The example system performance could be met with a 29

percent smaller attitude control system.

Finally, a new formulation for the time-varying image collection planning problem is presented by combining graph theory with optimal control into a hybrid optimal control architecture. This new formulation allows the use of different maneuvering algorithms whose performances were compared in Figure 1 with the boresight trace of each type represented by a different color. The collection window ended with the optimal control (STM) collecting 10 targets while the industry standard (ISM) was en-route to the seventh target; the STM collected 30 percent more targets. The performance of the STM could only be achieved by an ISM with a 1.41 times larger attitude control system (γ ISM). This simple example illustrated that higher agility is the goal, but a more agile collection capacity is the end result.

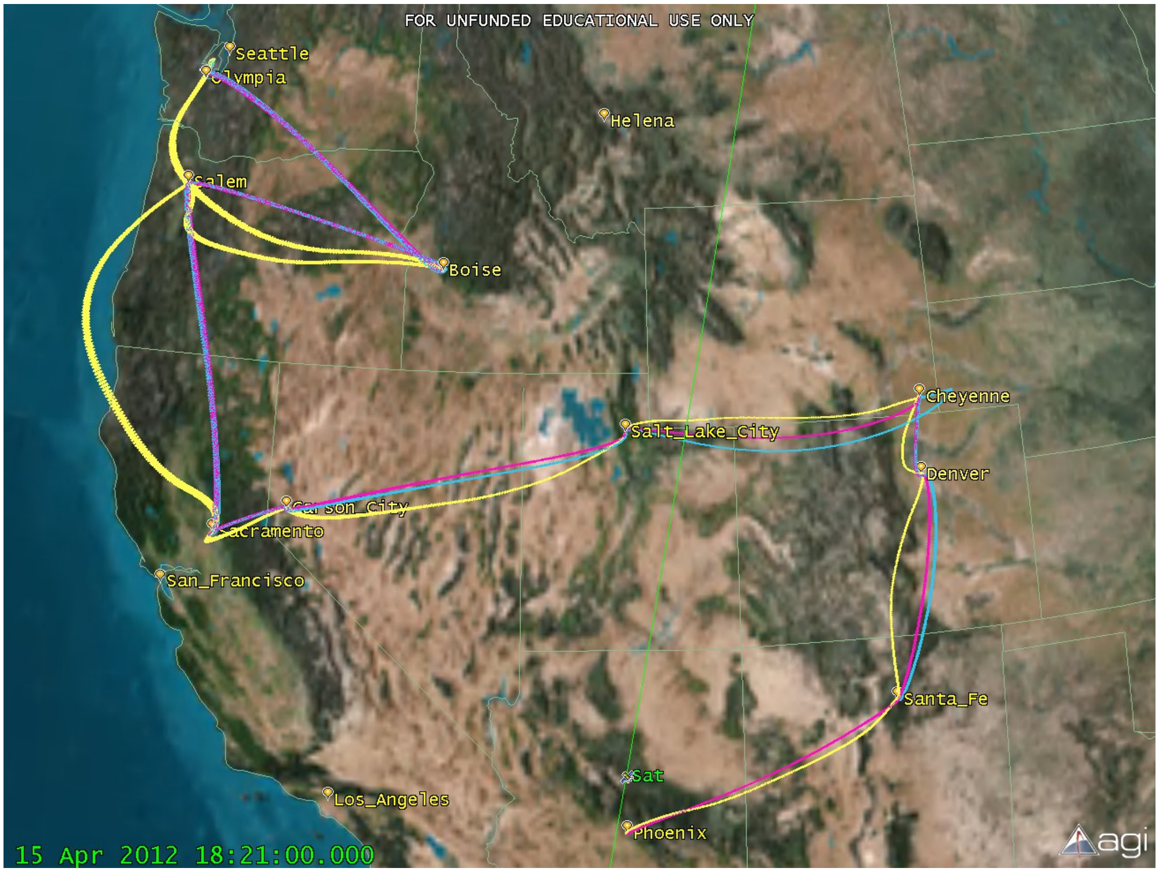

Figure 1: Relative Performance of ISM (blue), STM (yellow), and γ ISM (magenta) Collection Plans

Acknowledgements

I wish to thank my committee members for their time and attention in my journey of discovery. Specifically: Dr. Ross for taking me on as a project and mentoring me through the process; Dr. Karpenko for indulging my frequent interruptions and multiple questions; Dr. Newman for always keeping me focused on the larger picture; Drs. Kaminer and Kang for your invaluable insight along the way.

I also wish to thank the many fellow students that have helped me and taught me many things. Efforts such as this one are never a one person task.

My family deserves much of the credit for any success I may enjoy. It is their dedication and sacrifice of hours and days without me that made this possible.

Finally, I wish to thank my Saviour and Lord, Jesus Christ, for His love and grace. Everything I have and everything I am is a gift from the Lord.

THIS PAGE INTENTIONALLY LEFT BLANK

CHAPTER 1:
Introduction

1.1 Motivation

Space-based imagery has become part of everyday life and the need to increase quantity and timeliness of images continues to grow as more people become accustomed to these products. Space-based sensors are usually part of very large and expensive systems: it is not uncommon for an imaging satellite to cost hundreds of millions of dollars. As such, they should be as efficient as possible in order to maximize the return on investment.

The inability to respond to new tasking requests in a timely fashion is a direct result of the current processes used for collection planning [1]. Current planners create a collection plan often days in advance of the collection effort and therefore are not able to accommodate ad-hoc tasking in an efficient manner. The lack of dynamic ad-hoc tasking capability illustrates one of the prime motivators for solving the operational image collection planning problem in a different way.

For an operational overhead sensor, the attitude, body rates, and accelerations are all time dependent and coupled. The sensor must be at the correct attitude and motion at precisely the correct time in order to collect the desired target. Space-based sensors also have a significant challenge in collecting specific targets because they lack real-time pointing feedback from the target. Relative motion, sensor field of regard, and open-loop pointing all combine to mandate a very high precision and accuracy when planning and executing a series of maneuvers. Without this precision and accuracy, the risk is high that the sensor will collect something other than the intended target. The ability to determine the precise attitude, rate, and acceleration of a platform at a specific time to facilitate the target's subsequent collection is required.

The capacity to collect targets is directly related to the agility of the sensor [2]. Minimizing time to maneuver between targets allows an imaging sensor to collect the largest possible number of targets during a single pass. This dissertation demonstrates how optimal control is able to significantly increase available sensor agility in an operational setting. This increased agility can be exploited to improve the performance of current systems, or reduce the size, weight, and power of future systems without sacrificing performance.

While much of the academic literature for time-optimal maneuvering is limited to rest-to-rest (R2R) maneuvers (i.e., initial and final rates are zero), all operational imaging maneuvers are non-rest to non-rest (NR2NR) (i.e., non-zero rate boundary conditions). The NR2NR maneuver, regardless of time-optimality, results in a non-eigenaxis trajectory and cannot be generated using R2R eigenaxis-based algorithms, except under conservative assumptions. NR2NR maneuvers represent actual maneuvers and therefore time-optimal NR2NR maneuvers should be studied further for possible gains over current methods.

Increasing the sensor agility alone, however, is not sufficient. The ability to create a collection plan using this increased performance is required to realize an increase the overall collection capability of the system.

The space-based image collection planning problem can be described as choosing a sequentially ordered set of collection targets, from among a larger set of available targets, that maximize a specified benefit while remaining compliant to several time-dependent constraints. Most of the complicating factors are related to time, making the whole problem time dependent.

Presently, the challenge of collection planning is being met by simplifying the problem to a point that it can be solved by a given set of tools or algorithms. These simplifications degrade the performance of the system in order to linearize equations or remove certain complicating factors. The need exists for a way to create a collection plan that includes the actual operational constraints and dynamics and can incorporate increased sensor agility by using optimal control.

1.2 Collecting Images from Space

In order to produce images from space, the data from the target must be collected for this purpose and processed. Many modern imaging satellites utilize charged-coupled devices (CCDs) to acquire the image product. A CCD is a solid state chip that converts light directly to electrical signals [3]. Its advantages in space-based applications include good sensitivity and performance in the low light environment of space as well as small size, weight, and power requirements over more traditional sensors. The size of the image is determined by the number of CCDs in the sensor (see Figure 1.1). By creating a large focal plane array, staring-type sensors can image a larger area than a single CCD. Scanning sensors use linear arrays [4] of CCDs similar to the one shown in Figure 1.1(b).

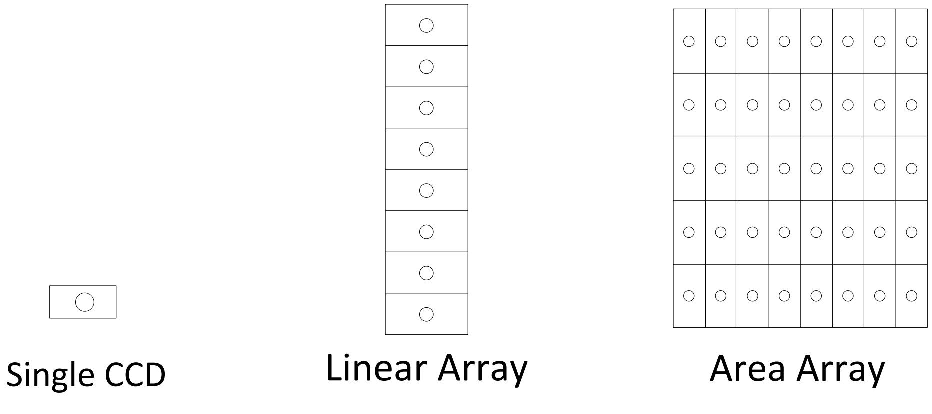

(a) (b) (c)

Figure 1.1: Single CCD (a), Linear Array (b), and Area CCD Array (c) Configurations

For a linear array, all the CCDs are sampled at the same time. The array is then moved to the next area or target to collect the next sample. These sensors scan in a push-broom fashion, as shown in Figure 1.2. The motion of the satellite over time provides the ability to collect an image across a given area target. The overall rate for a given scan is based on several factors including CCD size, capture rate, sensor altitude, and distance to target. These factors make the scan rate unique to a particular sensor-satellite combination [5]. The motion of the satellite must match this rate in order to create a contiguous image.

While all CCD based imagers require a finite dwell time as each pixel of information is collected, significant improvements in sensitivity have been achieved using time delay integration (TDI). TDI can be thought of as taking multiple images of the same object and combining them [6]. The electrical charge from an image in the linear CCD array is accumulated over time, using several arrays. The sensitivity of an N-stage TDI array is N times that of a single linear array, using the same scan time [4].

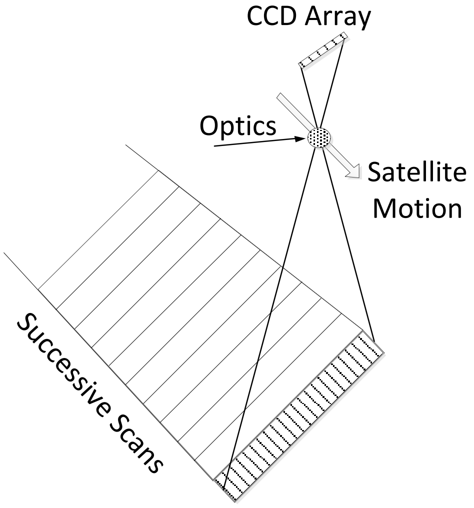

Figure 1.2: Pushbroom Imaging with a Linear CCD Array

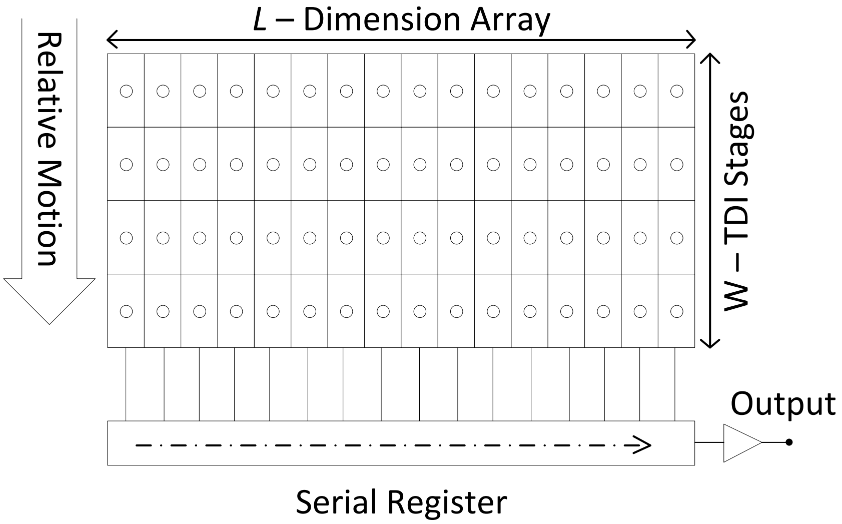

Figure 1.3: L x W Array of CCDs for TDI

The CCDs are typically arranged in an L by W array, with the L dimension being significantly larger than W (see Figure 1.3). The number of CCDs in the L direction determine the width of the target swath being collected. The *W* direction is used for TDI to accumulate electrical charge, enhancing the collected image quality. At each time step, the charge is transferred to the next cell until it is collected by a readout register. For TDI to work properly, the image must pass sequentially to each successive L-dimensional linear array in the same position and at the same time that the CCD is clocked to capture the image. Any difference in the relative motion, either in direction or speed, will cause a blurring of the captured image [6]. Many applications, including space-based platforms actually move the sensor across the image to achieve this relative motion. The direction and speed of the satellite motion must therefore be maintained in concert with the TDI time constant such that the result is a clear and stable image. Figure 1.4 is a simple illustration of this technique.

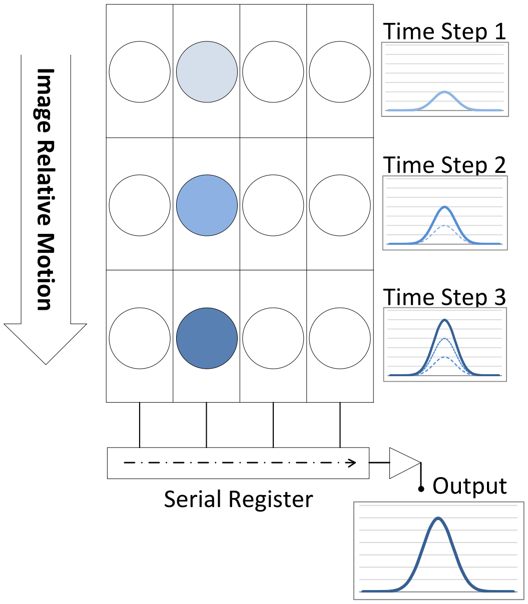

Figure 1.4: Time Domain Integration Technique

1.3 Relative Motion

Even though not all space imaging sensors are scanning sensors, all Earth-based or near Earth-based targets are moving targets. This motion arises from both the target's inherent motion with respect to the Earth and the motion of Earth itself. Therefore, without loss of generality, every point target can be transformed into an equivalent scan target. All targets are then specified with a particular velocity and acceleration equivalent to the desired scan or tracking motion. Thus, a spacecraft or sensor is in motion at the end of each scan (collect) corresponding to the direction and speed of the desired target. Between scans, the platform must maneuver to the precise attitude at the correct time to start the next scan collect. This requires the appropriate relative motion be accounted for in the boundary conditions. A slew between two scans, therefore, starts with non-zero body rates and ends with different non-zero body rates, based on the scan direction and scan rate.

Minimizing time between scans allows an imager to collect the largest possible area during a single pass. In order to image an area larger than the detector array can collect in one scan, the sensor must be able to perform successive scans on adjacent areas. Unless the sensor is articulated and controlled separately, the satellite or platform must continually reorient itself to achieve the desired attitude and motion in order to accomplish each scan. The orbital motion of the satellite limits the visibility, or access, to a particular point on the Earth. In general, time spent slewing from one scan to another does not produce product or revenue thus planners work to minimize slew time during a given pass [7].

The CCD-TDI sensor is designed to collect images in a certain direction with respect to the satellite platform. The nominal collection orientation and direction of relative motion is called a forward scan. Some sensors may be capable of bi-directional image collection [8, 9]. This may be accomplished by using two oppositely oriented TDI arrays, or a serial register and output on opposite ends of the same array, with a corresponding method to control the timing signal. These sensors are said to have a reverse scan capability in addition to forward scan. The importance of this distinction lies primarily in how succeeding scans are connected.

Even for a non-scanning sensor, the attitude, body rates, and accelerations are all time dependent and coupled. The sensor must be at the correct state at precisely the correct time in order to collect the correct target. Arriving up at a particular attitude, rate, and acceleration at an earlier time results in a sensor that is pointing at a different target.

Figure 1.5 illustrates that targeting the same attitude at a different time results in not being aligned with the target. The black vectors represent the attitude of the sensor at the beginning of a maneuver (t_0) and the center green vectors are the correct targeting attitude at the end of the maneuver ($t_f - dt$). The faded green vectors on the right represent the same final attitude (as $t_f - dt$), but at a later time, (t_f). The blue vectors represent the correct targeting attitude at time t_f. Space-based image collection requires the knowledge of the specific attitude and motion state for each instant in time so that the maneuvering sensor can to execute the mission successfully.

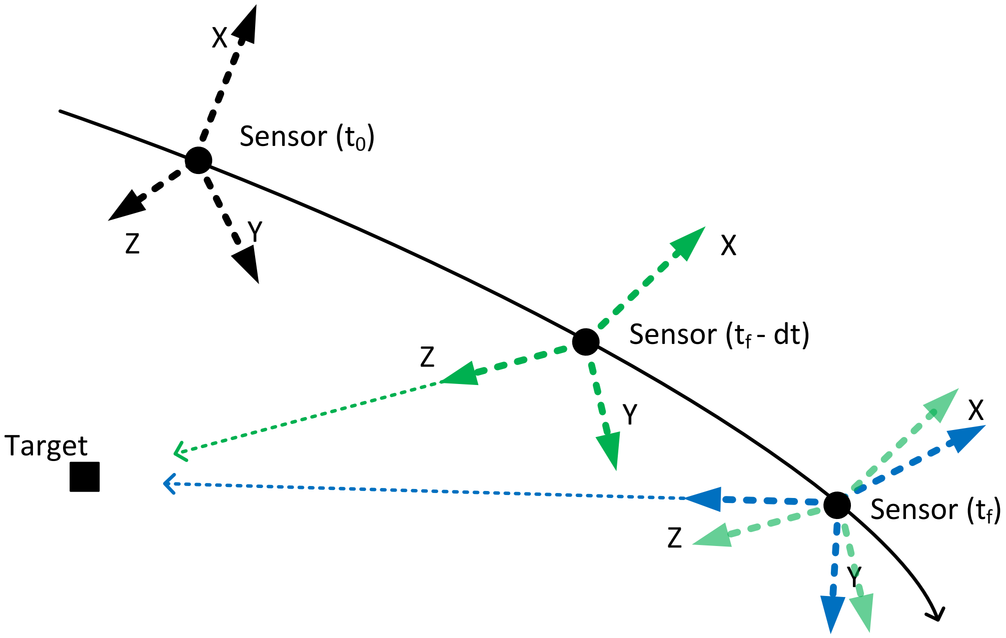

Figure 1.5: Illustration of Time-Varying Nature of Targeting

1.4 Objectives and Scope

The objective of this work is twofold: demonstrate and quantify the improvement in agility available using optimal control, and formulate the operational collection planning problem without undue simplifications or preconceived solution methods. While this dissertation is written primarily with space-based platforms and sensors as examples, the equations and concepts are applicable to any overhead moving sensor, such as manned aircraft or unmanned aerial vehicles. Each chapter includes a literature review addressing the material covered in that chapter. The remaining chapters are organized as follows.

Chapter 2 presents a new set of targeting equations that are able to accommodate both moving targets and area scans while providing the ability to predict an overhead sensor's particular attitude, rate, and acceleration needed to collect a certain target at a specific time. The work is based on the algebraic method described in Wertz [10] but expanded to include angular rates and accelerations.

Chapter 3 demonstrates how sensor agility can be improved using optimal control. R2R maneuvers are explored and compared to standard eigenaxis maneuvers. The agility envelope is described and a new method of estimating the performance benefit of optimal control maneuvering is presented. This method only requires calculating the volume of the agility envelope of a system in order to quantify the potential increase in agility. There is no need to solve the optimal control (OC) problem to estimate the agility increase. While it is demonstrated using the performance difference between optimal control and industry standard algorithms, it can also be used to show the performance difference between any two maneuvering algorithms (provided the respective agility envelopes can be constructed). NR2NR optimal control maneuvers are formulated and demonstrated, expanding the body of time-optimal control maneuvering literature beyond R2R. Additionally, specific maneuvers to connect sequential scan targets are presented and analyzed using optimal control.

Chapter 4 transitions the dissertation to the problem of collection planning (i.e., how and which targets to collect from a sensor) using optimal control maneuvers. Graph theory elements are introduced and examples are given for the space-based sensor application. The problem is then expanded to include more realistic elements that vary with time. Each element is discussed and space-based sensor examples are used. This time-varying image collection graph problem is capable of incorporating time-optimal maneuvers and represents a new formulation of the overhead collection planning problem, since optimal control maneuvering has never been used in collection planning prior to this work. By combining graph theory and optimal control, the operational problem can be formulated as a hybrid optimal control problem. The solution to the time-varying hybrid optimal control problem is beyond the scope of this dissertation.

Chapter 5 illustrates elements of a candidate solution to the time-varying collection planning problem presented in Chapter 4. By comparing different maneuvering types from Chapter 3, this chapter compares the overall performance using an operational real-world scenario, which includes the new targeting equations of Chapter 2.

Chapter 6 closes the work with a summary and detailed description of several areas of possible future research.

Original Contributions

Original contributions of this work include:

i) The development of a new set of targeting equations that represent the precise conditions required at a given time for a moving sensor to collect a moving target with little or no control effort. They differ from previous work because they make no assumption regarding the relationships between angles, rates, etc.

ii) A new method for estimating agility along with a new figure of merit for comparing the performance of various maneuvering methods are presented.

iii) The design of time-optimal NR2NR maneuvers, including maneuvers to connect sequential area scans, are designed using optimal control methods.

iv) A time-varying collection planning problem formulated as a hybrid optimal control problem, which can utilize optimal control maneuvering as the basis for transiting between targets. This new formulation maintains the realistic and operational constraints without simplification in an attempt to create the highest benefit plan possible.

CHAPTER 2:
Space-Based Targeting

The effect of a target's relative motion is never more clearly seen than when looking through a telescope at the moon. The moon is approximately 1,000 times farther away from the telescope than an Earth-based target is from a low Earth orbiting satellite platform. This means the relative motion between the Earth and moon is much slower than the motion between spacecraft and target. Yet, when viewing a point on the moon, constant adjustment and motion of the telescope is needed to maintain alignment.

Tracking the moon also demonstrates another issue for space-based sensors. While a satellite has a large field of regard on the Earth due to its altitude, it cannot collect meaningful images on the entire field of regard at the same time. In the same way that one has a large field of regard to the night sky and the planets, it is not until that regard is focused and limited to a very small aperture that one is able to see the rings of Saturn. Space-based sensors must similarly limit their aperture causing a "soda-straw" effect. This effect is the same as looking through a soda-straw at a distant target. When looking through a soda-straw or telescope, pointing accuracy is critical. A small error in pointing can result in missing the target completely.

Space-based sensors also have a significant challenge in collecting specific targets due to the lack of any real-time pointing feedback. There are no current examples of an on board space-based imager receiving real-time pointing feedback from the target. This has been done with active communication systems, but not with passive imagers or collectors. Calibration is often done when the collect of a known location is post-processed for accuracy. The pointing error can be reduced for the platform in terms of correction coefficients for future collects, but it is accomplished over days and not real-time. Therefore, the space-based sensor must point to an attitude that it believes corresponds to a desired target. Any feedback in the system is simply to determine whether or not the sensor is pointing at the commanded attitude and has no ability to determine if it is the correct target. The assumption is made that the targeting attitude is known precisely and specified correctly, thus success results from closing the loop on the specified attitude. Another way to look at the open-loop pointing issue is to recognize that all attitude commands to space-based platforms are fundamentally inertial attitudes or derivatives of them. The sensor is commanded to a specific state (attitude, rate, and/or acceleration) in inertial space, with the premise that the Earth will be in the correct spot at the exact time the image is collected.

Relative motion, sensor field of regard, and open-loop pointing combine to mandate a very high precision and accuracy threshold when executing maneuvers. Without this precision and accuracy, the risk is high that the sensor will collect something other than the intended target. The sensor must achieve the correct attitude and the dynamic relative motion (rates and/or accelerations) at a particular time. This complicates the planning process because the relative motion is coupled with the targeting attitude. Both elements are needed as part of the commanded state in order to accurately target a sensor. While this chapter is written primarily with space-based platforms and sensors in mind, the equations are applicable to any overhead moving sensor, such as aircraft or unmanned aerial vehicles (UAVs).

Literature Review

Much of what is published under the subject of target tracking is primarily focused on controlling a platform to track a given set of inputs. The problem presented in this chapter is fundamentally different. The goal is to determine the precise attitude, rate, and acceleration of a platform at a specific time that will facilitate the target's subsequent collection. The most straight forward method of determining the correct targeting attitude is based on the algebraic method described in Wertz [10]. This algorithm uses two independent vectors to determine the direction cosine matrix (DCM) from one reference frame to the other frame. Unfortunately, it does not address the body rates or accelerations required to maintain pointing at a given target, but simply the attitude at a particular time.

Time-optimal maneuvers are extensively documented in academic literature [10–22]. However, because the maneuvers in these references are R2R and do not include non-zero rates or accelerations as terminal conditions, they are incapable of accounting for the relative motion between target and sensor. Algorithms for finding targeting attitude are given in [23–26], but they do not address finding rates or accelerations.

Some work assumes the non-zero body rates are given [27, 28] and subsequently define a method to maintain sensor pointing. However, since the targeting rates are not known *a priori*, these methods are inadequate for the operational maneuver planning scenario. Body rates are indirectly addressed in [29, 30] by defining a quaternion trajectory for attitude tracking purposes and allowing the rates to follow without formally calculating target specific rates and accelerations. This method may work when employing a particular controller, but lacks the ability to define the beginning or ending conditions for a specific targeting maneuver. Final targeting rates (initial rates are assumed to be zero) are used in [31], however, the accommodation for final rates is added on at the end of an eigenaxis R2R maneuver as a deviation and not included in the derivation of the problem or scenario. Stationary point targets are assumed in [28, 32], thus, the developed equations are not able to accommodate scans or moving targets. This makes them impractical for all but a very small subset of targets.

Targeting equations are derived in [33], using modified Rodriques parameters for a sun-tracking case, but not for a scanning sensor. Though Long's derivation of rates and accelerations is similar to this dissertation, simplifying assumptions were made (e.g., spacecraft motion in a circular orbit) in [33] such that the results are not applicable to the general imaging problem. Long also uses the eigenaxis R2R as the basis for a maneuver and allows the controller to settle in on the final rates as a deviation or error.

Body rates are included in the derivation of the targeting state in [34], but the assumption of point targets allows an arbitrary constraint on the body rate, such as canceling out all motion about the bore-sight. Similarly, [35] uses point targets only and arbitrarily chooses the targeting orientation such that the amplitude of the angular rate is minimized. Because the assumption of point targets was employed, neither of these methods are able to employ a scanning sensor or dwell on a moving target.

Since relative motion is couple with the required targeting attitude at any particular time this chapter will derive general equations for sensor attitude, sensor body rates and sensor body accelerations and show how this knowledge can be used to improve maneuvering performance.

2.1 Reference Frames

At least four unique reference frames are defined for the general targeting problem: an inertial reference frame, i, the target centric reference frame, t, the spacecraft body reference frame, b, and the sensor centric reference frame, s. The inertial reference frame is considered fixed. However, the remaining reference frames are allowed to move both in rotation and translation. The target centric reference frame is fixed to the target and can be defined in any way that makes sense, based on the type of target. For example, an Earth-based target might use an Earth centered, Earth fixed frame. In any case, there is a predefined transformation from the target frame to the inertial frame such that the target data can be specified in, or transformed into, the inertial frame. As a result, the target position and velocity are assumed to be specified in inertial Cartesian coordinates.

The spacecraft body reference frame is specified from the spacecraft center of mass by three orthogonal direction vectors. It is known and fixed within the spacecraft, however, it does move and rotate in inertial space with the spacecraft orbit and attitude. Figure 2.1 shows the relationship between the i, t, and b frames.

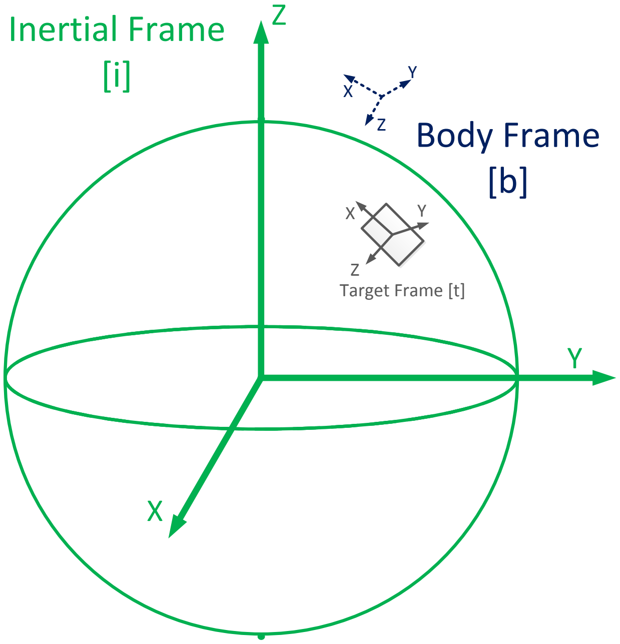

Figure 2.1: Reference Frames i, t and b

The transformation between the body frame and the inertial frame gives the attitude of the spacecraft. It can be specified in the form of a DCM, quaternions, Euler angles or any number of other forms [36]. This dissertation uses primarily DCMs and quaternions to represent attitude.

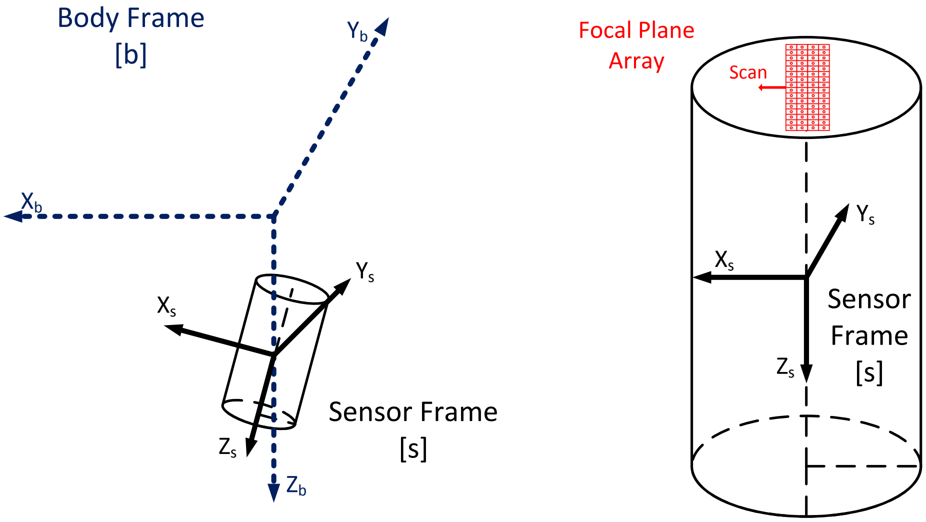

(a) (b)

Figure 2.2: Reference Frames b and s (a), and Reference Frame s with Focal Plane (b)

The spacecraft orbit information is used to define its position and velocity in inertial space. Conversion from classical orbital elementss (COEs) or any other standard orbital parameters to Cartesian coordinates is described in various texts [37–40]. For the purposes of targeting, the spacecraft position and velocity are assumed to be specified in inertial Cartesian vectors, similar to the target position and velocity.

The spacecraft has an imaging sensor that is fixed with respect to the spacecraft. The frame attached to the sensor is fixed with respect to the sensor and located at its center of mass. This means that any vector in the sensor frame, s, can be described in terms of the spacecraft body frame, b, by a fixed and constant transformation [41]. The sensor frame is arbitrarily specified with the +Z axis of the sensor frame aligned along the sensor bore-sight. See Figure 2.2(a). Furthermore, a TDI based or scanning sensor has a specific orientation and requires the relative motion of the target to be aligned with a particular scan direction as shown in Figure 2.2(b). This direction is presumed to be aligned with the +X axis of the sensor frame.

2.1.1 Transformations and Vector Notation

At any given time, a vector in one frame can also be expressed in any other frame using a transformation matrix or DCM. Specifically, this dissertation uses the notation ${}^{b}C^{a}$, where C is the DCM from generic frame a to generic frame b. Therefore, a vector expressed in frame b can also be expressed in frame a as follows [41] (left superscripts denote reference frame):

$$ {}^{a}\boldsymbol{v} := v_1\,\hat{a}_1 + v_2\,\hat{a}_2 + v_3\,\hat{a}_3 \tag{2.1} $$

and

$$ {}^{b}\boldsymbol{v} := v_1\,\hat{b}_1 + v_2\,\hat{b}_2 + v_3\,\hat{b}_3 \tag{2.2} $$

Therefore,

$$ {}^{a}\boldsymbol{v} = {}^{a}C^{b}\,{}^{b}\boldsymbol{v} \qquad \text{and} \qquad {}^{b}\boldsymbol{v} = {}^{b}C^{a}\,{}^{a}\boldsymbol{v} \tag{2.3} $$

The inverse transformation simply uses the transpose of the DCM, a unique property of DCMs [38].

$$ \left[{}^{b}C^{a}\right] = \left[{}^{a}C^{b}\right]^{-1} = \left[{}^{a}C^{b}\right]^{T} \tag{2.4} $$

A direction vector is a vector whose length is unity. The direction of vector, $\boldsymbol{x}$, is defined as $\hat{\boldsymbol{x}} = \boldsymbol{x}/|\boldsymbol{x}|$, where $|\boldsymbol{x}|$ is the Euclidean length of the vector.

The spacecraft position and velocity, specified in inertial coordinates, are given by ${}^{i}\boldsymbol{r}_{sc}$ and ${}^{i}\boldsymbol{v}_{sc}$. The target position and velocity, specified in inertial coordinates, are given by ${}^{i}\boldsymbol{r}_{tgt}$ and ${}^{i}\boldsymbol{v}_{tgt}$. If specified in the target frame, a single transformation is required to transform these quantities into the inertial frame:

$$ {}^{i}\boldsymbol{r}_{tgt} = {}^{i}C^{t}\,{}^{t}\boldsymbol{r}_{tgt} \tag{2.5} $$

Figure 2.3 shows how the line of sight (LOS) vector, $\boldsymbol{r}_{los}$, from the satellite to the target is calculated. Equation (2.6) defines the LOS position, velocity and acceleration vectors. Note that in (2.6), the direction of each vector may be different but the vector addition per Figure 2.3 still holds.

$$\begin{aligned} \boldsymbol{r}_{los} &= \boldsymbol{r}_{tgt} - \boldsymbol{r}_{sc} \\ \boldsymbol{v}_{los} &= \boldsymbol{v}_{tgt} - \boldsymbol{v}_{sc} \\ \boldsymbol{a}_{los} &= \boldsymbol{a}_{tgt} - \boldsymbol{a}_{sc} \end{aligned} \tag{2.6}$$

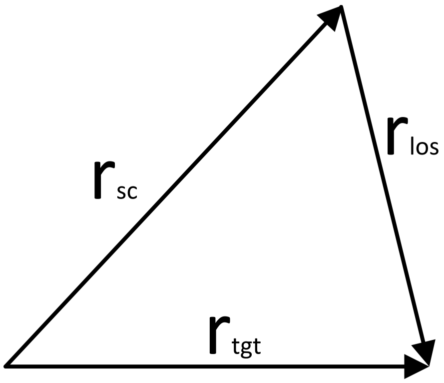

Figure 2.3: Vector Addition

In order to image any target, it is not enough to simply point at the target. The sensor must also be moving in such a way that it will remain on target despite the relative motion. Otherwise, it will soon be imaging something other than the desired target because the target is moving one way and the sensor is moving another. For an area scan, this motion is specified by the rate of scan along a desired direction of scan, $\hat{\boldsymbol{S}}$. Because every target can be transformed into an equivalent scan target, all targets are specified with a particular velocity and acceleration equivalent to the desired scan or tracking motion. The relative motion between sensor and target must be aligned with the scanning sensor, thus the scan direction, $\hat{\boldsymbol{S}}$, is defined by the direction of the relative motion vector $\boldsymbol{v}_{los}$ and illustrated in Figure 2.4.

$$\hat{\boldsymbol{S}} := \frac{\boldsymbol{v}_{los}}{|\boldsymbol{v}_{los}|} \tag{2.7}$$

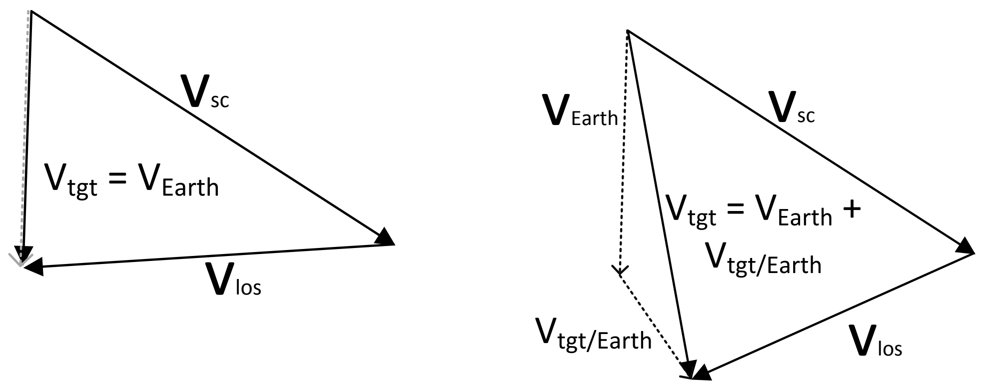

(a) (b)

Figure 2.4: Scan Direction Illustration of Stationary Targets (a) and Moving Targets (b)

The rate of change of the scan direction, $\dot{\hat{\boldsymbol{S}}}$, is the derivative of the scan direction, which is a unit direction vector. Generically, the time derivative of a unit vector is

$$\frac{d}{dt}\hat{\boldsymbol{u}} = \frac{d}{dt}\left(\frac{\boldsymbol{u}}{|\boldsymbol{u}|}\right) = \frac{\dot{\boldsymbol{u}}}{|\boldsymbol{u}|} - \left(\frac{\dot{\boldsymbol{u}}}{|\boldsymbol{u}|}\cdot\hat{\boldsymbol{u}}\right)\hat{\boldsymbol{u}} \tag{2.8}$$

Therefore, with $\boldsymbol{a}_{los} = \dot{\boldsymbol{v}}_{los}$,

$$\dot{\hat{\boldsymbol{S}}} := \frac{d}{dt}\hat{\boldsymbol{S}} = \frac{\boldsymbol{a}_{los}}{|\boldsymbol{v}_{los}|} + \left(\frac{\boldsymbol{a}_{los}}{|\boldsymbol{v}_{los}|}\cdot\hat{\boldsymbol{v}}_{los}\right)\hat{\boldsymbol{v}}_{los} \tag{2.9}$$

2.2 Defining Required Platform Orientation

The first step in determining the required attitude is to find the spacecraft or platform attitude that aligns the sensor with the target and with the desired scan direction. In order to maintain distinction between current and desired attitude and rates, a new reference frame is defined called the f frame. It is defined as the desired sensor attitude and motion, centered at the sensor center of mass. Its axes are defined similarly to the sensor frame axes such that both frames are coincident when the spacecraft is aligned properly. Figure 2.5 shows both the f frame (in green) and sensor frame (in blue) orientations.

The f frame is specified such that the desired image motion is along the $\hat{\boldsymbol{f}}_1$ axis, which is the $\hat{\boldsymbol{X}}$ axis of the sensor frame. The $\hat{\boldsymbol{f}}_3$ axis is defined along the sensor bore-sight, e.i.,the $\hat{\boldsymbol{Z}}$ sensor axis. The third axis $\hat{\boldsymbol{f}}_2$ completes the right-handed coordinate system.

The desired attitude is obtained when $\hat{\boldsymbol{f}}_3$ is parallel to $\hat{\boldsymbol{r}}_{los}$, as shown in Figure 2.5. This is accomplished when

$$\boldsymbol{f}_3 \cdot \boldsymbol{r}_{los} = 1 \qquad \text{or} \qquad \hat{\boldsymbol{f}}_3 = \hat{\boldsymbol{r}}_{los} \tag{2.10}$$

because the unit direction vectors, if parallel, are identical.

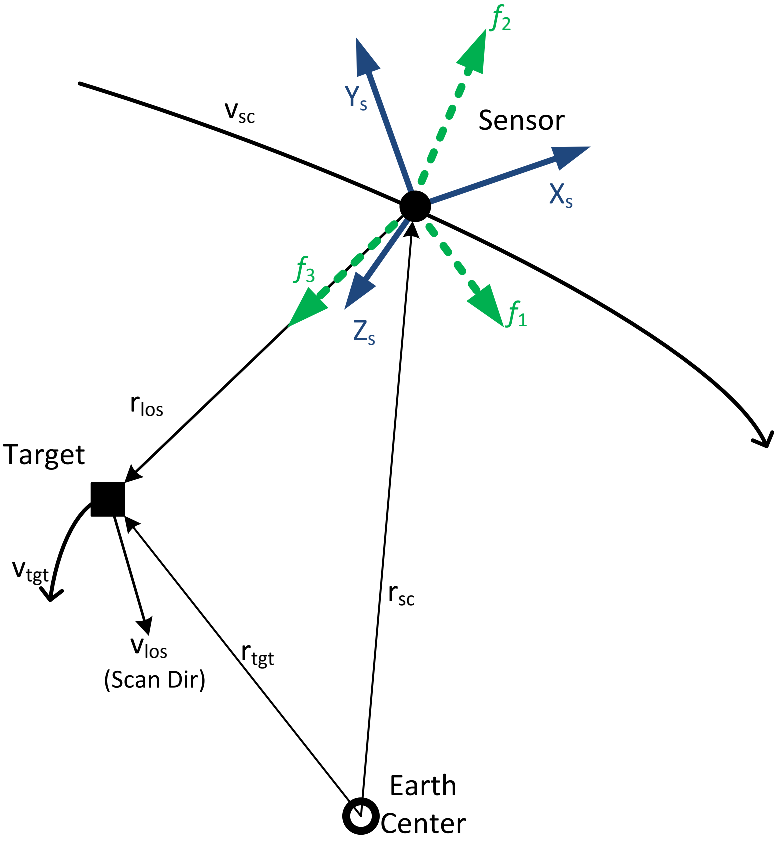

Figure 2.5: Schematic of the Targeting Problem, after [42]

Many derivations stop here [10–12, 18–20, 23–26] because attitude is their primary goal. These derivations either assume point targets or do not account for the motion between satellite and target. However, using a scanning sensor or accounting for the relative motion requires an additional constraint of aligning the sensor collection direction, $\hat{\boldsymbol{f}}_1$, along the desired scan direction, $\hat{\boldsymbol{S}}$.

In the special case where $\hat{\boldsymbol{S}}$ and $\hat{\boldsymbol{f}}_3$ are parallel, the constraint becomes similar to (2.10). However, this represents a unique situation where the scan direction and all the relative motion is along the sensor bore-sight. In this scenario, the constraint on $\hat{\boldsymbol{f}}_1$ becomes arbitrary and inactive. The likelihood of this situation for a space based platform with nominal imaging constraints is extremely low, because most space-based sensors look down onto a target and thus all the relative motion would not be along the bore-sight (i.e., $\boldsymbol{v}_{los}$ parallel to $\boldsymbol{r}_{los}$).

Constraining the projection of $\hat{\boldsymbol{f}}_1$ to be in the same direction desired scan direction, $\hat{\boldsymbol{S}}$ requires $\hat{\boldsymbol{f}}_1 \cdot \hat{\boldsymbol{S}} > 0$. An inequality is required because the first constraint on $\hat{\boldsymbol{f}}_3$ may prevent a perfect alignment of $\hat{\boldsymbol{f}}_1$ and $\hat{\boldsymbol{S}}$. Alternatively, this orientation can also be described by constraining $\hat{\boldsymbol{f}}_2$ to be perpendicular to the scan direction or $\hat{\boldsymbol{f}}_2 \cdot \hat{\boldsymbol{S}} = 0$, since $\hat{\boldsymbol{f}}_2$ is, by definition, perpendicular to $\hat{\boldsymbol{f}}_1$. More precisely, $\boldsymbol{f}_2$ must be perpendicular to the plane created by the sensor bore-sight and the desired scan direction. The cross product produces a vector that is perpendicular to both input vectors with direction determined by the order of multiplication. Therefore, the constraint becomes

$$\boldsymbol{f}_2 = \hat{\boldsymbol{f}}_3 \times \hat{\boldsymbol{S}} \tag{2.11}$$

Note that the direction vector, $\hat{\boldsymbol{f}}_2$, must still be found using the definition of a unit direction vector.

In order to ensure that the coordinate frame is consistent, $\boldsymbol{f}_1$ is defined in terms of $\hat{\boldsymbol{f}}_2$ and $\hat{\boldsymbol{f}}_3$ as

$$\boldsymbol{f}_1 = \hat{\boldsymbol{f}}_2 \times \hat{\boldsymbol{f}}_3 \tag{2.12}$$

2.3 Calculating Required Platform Attitude

The targeting attitude developed here generally follows the algebraic method [10]. Let the f frame be defined, in the sensor frame coordinates, as

$$ {}^{s}\hat{\boldsymbol{f}}_1 = \begin{bmatrix} 1 \\ 0 \\ 0 \end{bmatrix} \cdot [\hat{\boldsymbol{s}}_1\ \hat{\boldsymbol{s}}_2\ \hat{\boldsymbol{s}}_3] \qquad {}^{s}\hat{\boldsymbol{f}}_2 = \begin{bmatrix} 0 \\ 1 \\ 0 \end{bmatrix} \cdot [\hat{\boldsymbol{s}}_1\ \hat{\boldsymbol{s}}_2\ \hat{\boldsymbol{s}}_3] \qquad {}^{s}\hat{\boldsymbol{f}}_3 = \begin{bmatrix} 0 \\ 0 \\ 1 \end{bmatrix} \cdot [\hat{\boldsymbol{s}}_1\ \hat{\boldsymbol{s}}_2\ \hat{\boldsymbol{s}}_3] \tag{2.13} $$

Employing (2.3), ${}^{s}\hat{\boldsymbol{f}}$ can be expressed in inertial frame.

$$ \begin{bmatrix} {}^{i}\hat{\boldsymbol{f}}_1 & {}^{i}\hat{\boldsymbol{f}}_2 & {}^{i}\hat{\boldsymbol{f}}_3 \end{bmatrix} = {}^{i}C^{s} \begin{bmatrix} {}^{s}\hat{\boldsymbol{f}}_1 & {}^{s}\hat{\boldsymbol{f}}_2 & {}^{s}\hat{\boldsymbol{f}}_3 \end{bmatrix} \tag{2.14} $$

Substituting (2.13) into (2.14) and solving for ${}^{i}C^{s}$:

$$ {}^{i}C^{s} = \begin{bmatrix} {}^{i}\hat{\boldsymbol{f}}_1 & {}^{i}\hat{\boldsymbol{f}}_2 & {}^{i}\hat{\boldsymbol{f}}_3 \end{bmatrix} \tag{2.15} $$

Knowing ${}^{i}C^{s}$ allows the transformation of any vector from the aligned sensor frame to the inertial frame. The transformation matrix can then be converted into any number of parameters to specify spacecraft attitude. This dissertation either maintains the DCM matrix form or converts to quaternions, $[q_1, q_2, q_3, q_4]^T$ where q_4 is the scalar value [38].

Additionally, since the sensor is fixed with respect to the body frame, the fixed transformation from sensor frame to body frame, ${}^{b}C^{s}$, can be defined a priori.

2.4 Calculating Required Platform Rates

Since the desired attitude is only valid at a single instant in time, the spacecraft attitude must change with time. The change is due to the motion of the satellite, sensor, and any target motion. This is true whether the target is stationary or moving, since the satellite is always moving in its orbit. A given scan can also be thought of as a single point target with its motion across the scan area at the desired rate of scan.

If the spacecraft motion is precisely the same as the rate of change of the f frame vectors, it will remain aligned on the target with little or no control required. Therefore, differentiating the $\hat{\boldsymbol{f}}$ vectors with respect to time yields the desired platform attitude rate of change. Applying (2.8) to $\hat{\boldsymbol{f}}_3$ yields

$$\dot{\hat{\boldsymbol{f}}}_3 = \frac{d}{dt}\hat{\boldsymbol{f}}_3 = \frac{d}{dt}\hat{\boldsymbol{r}}_{los} = \frac{\dot{\boldsymbol{r}}_{los}}{|\boldsymbol{r}_{los}|} - \left(\frac{\dot{\boldsymbol{r}}_{los}}{|\boldsymbol{r}_{los}|} \cdot \hat{\boldsymbol{r}}_{los}\right)\hat{\boldsymbol{r}}_{los} \tag{2.16}$$

The time derivative of $\hat{\boldsymbol{f}}_2$ similarly follows

$$\dot{\hat{\boldsymbol{f}}}_2 = \frac{d}{dt}\frac{\boldsymbol{f}_2}{|\boldsymbol{f}_2|} = \frac{\dot{\boldsymbol{f}}_2}{|\boldsymbol{f}_2|} - \left(\frac{\dot{\boldsymbol{f}}_2}{|\boldsymbol{f}_2|} \cdot \hat{\boldsymbol{f}}_2\right)\hat{\boldsymbol{f}}_2 \tag{2.17}$$

where $\dot{\boldsymbol{f}}_2$ is the time derivative of (2.11)

$$\dot{\boldsymbol{f}}_2 = \frac{d}{dt}\boldsymbol{f}_2 = (\dot{\hat{\boldsymbol{f}}}_3 \times \hat{\boldsymbol{S}}) + (\hat{\boldsymbol{f}}_3 \times \dot{\hat{\boldsymbol{S}}}) \tag{2.18}$$

Calculating the derivative of $\hat{\boldsymbol{f}}_1$, using (2.12) becomes

$$\dot{\hat{\boldsymbol{f}}}_1 = \frac{d}{dt}\frac{\boldsymbol{f}_1}{|\boldsymbol{f}_1|} = \frac{\dot{\boldsymbol{f}}_1}{|\boldsymbol{f}_1|} - \left(\frac{\dot{\boldsymbol{f}}_1}{|\boldsymbol{f}_1|} \cdot \hat{\boldsymbol{f}}_1\right)\hat{\boldsymbol{f}}_1 \tag{2.19}$$

with

$$\dot{\boldsymbol{f}}_1 = \frac{d}{dt}\boldsymbol{f}_1 = (\dot{\hat{\boldsymbol{f}}}_2 \times \hat{\boldsymbol{f}}_3) + (\hat{\boldsymbol{f}}_2 \times \dot{\hat{\boldsymbol{f}}}_3) \tag{2.20}$$

The time derivative of the relationship between the inertial frame and the spacecraft body frame in (2.14), carrying out all terms, becomes

$$\begin{bmatrix} {}^{i}\dot{\hat{\boldsymbol{f}}}_1 & {}^{i}\dot{\hat{\boldsymbol{f}}}_2 & {}^{i}\dot{\hat{\boldsymbol{f}}}_3 \end{bmatrix} = {}^{i}\dot{C}^{s} \begin{bmatrix} {}^{s}\hat{\boldsymbol{f}}_1 & {}^{s}\hat{\boldsymbol{f}}_2 & {}^{s}\hat{\boldsymbol{f}}_3 \end{bmatrix} + {}^{i}C^{s}\,\frac{{}^{s}d}{dt} \begin{bmatrix} {}^{s}\hat{\boldsymbol{f}}_1 & {}^{s}\hat{\boldsymbol{f}}_2 & {}^{s}\hat{\boldsymbol{f}}_3 \end{bmatrix} \tag{2.21}$$

However, the definition of the sensor axes $\hat{\boldsymbol{f}}$ precludes any motion in the sensor frame, thus the time derivative with respect to the sensor frame, $\frac{{}^{s}d}{dt}\begin{bmatrix} {}^{s}\hat{\boldsymbol{f}}_1 & {}^{s}\hat{\boldsymbol{f}}_2 & {}^{s}\hat{\boldsymbol{f}}_3 \end{bmatrix} = 0$. Along with the definitions in (2.13), ${}^{i}\dot{C}^{s}$ is now defined by

$${}^{i}\dot{C}^{s} = \begin{bmatrix} {}^{i}\dot{\hat{\boldsymbol{f}}}_1 & {}^{i}\dot{\hat{\boldsymbol{f}}}_2 & {}^{i}\dot{\hat{\boldsymbol{f}}}_3 \end{bmatrix} \tag{2.22}$$

Let the rate of rotation of the sensor frame, s, with respect to the inertial frame, i, be defined as

$$ {}^{i}\boldsymbol{\omega}^{s} = \begin{bmatrix} \omega_1 \\ \omega_2 \\ \omega_3 \end{bmatrix} \tag{2.23} $$

The time derivative of the DCM becomes [39, 43]

$$ {}^{i}\dot{C}^{s} = {}^{i}[{}^{i}\boldsymbol{\omega}^{s}] \times {}^{i}C^{s} = \begin{bmatrix} 0 & -\omega_3 & \omega_2 \\ \omega_3 & 0 & -\omega_1 \\ -\omega_2 & \omega_1 & 0 \end{bmatrix} {}^{i}C^{s} \tag{2.24} $$

Let the skew symmetric matrix representing $\boldsymbol{\omega}\times$ be defined as

$$ \boldsymbol{\Omega} := \begin{bmatrix} 0 & -\omega_3 & \omega_2 \\ \omega_3 & 0 & -\omega_1 \\ -\omega_2 & \omega_1 & 0 \end{bmatrix} \tag{2.25} $$

Combining the above equations and rearranging terms while solving for ${}^{i}[{}^{i}\boldsymbol{\Omega}^{s}]$,

$$ {}^{i}[{}^{i}\boldsymbol{\Omega}^{s}] = {}^{i}\dot{C}^{s}\, {}^{i}C^{s^T} = \begin{bmatrix} {}^{i}\dot{\hat{\boldsymbol{f}}}_1 & {}^{i}\dot{\hat{\boldsymbol{f}}}_2 & {}^{i}\dot{\hat{\boldsymbol{f}}}_3 \end{bmatrix} {}^{s}C^{i} \tag{2.26} $$

The angular rates are additive [38], meaning ${}^{i}\omega^{s} = {}^{i}\omega^{b} + {}^{b}\omega^{s}$. However, because the sensor is fixed within the platform, the rate of change of the sensor frame with respect to the body frame is assumed to be zero (i.e., ${}^{b}\boldsymbol{\omega}^{s} = {}^{s}\boldsymbol{\omega}^{b} = 0$), thus ${}^{i}\boldsymbol{\omega}^{s} = {}^{i}\boldsymbol{\omega}^{b}$. Once the right hand side of (2.26) is evaluated, the values for ${}^{i}\boldsymbol{\omega}_1^{b}$, ${}^{i}\boldsymbol{\omega}_2^{b}$, and ${}^{i}\boldsymbol{\omega}_3^{b}$ are obtained by inspection of the resulting skew symmetric matrix, ${}^{i}\boldsymbol{\Omega}^{s}$.

The goal is to define the attitude rates of the spacecraft in the spacecraft body frame, since the actuators that will accomplish this motion are normally specified and controlled in this frame. Having calculated the rotation rates in the inertial frame, a simple transformation to the spacecraft body frame is accomplished using ${}^{b}C^{i} = {}^{b}C^{s}\, {}^{s}C^{i}$ and (2.3).

2.5 Calculating Required Platform Accelerations

Following a similar method to the general derivation of (2.8),

$$\frac{d}{dt}\left(\frac{\dot{\boldsymbol{u}}}{|\boldsymbol{u}|}\right) = \frac{\ddot{\boldsymbol{u}}}{|\boldsymbol{u}|} - \left(\frac{\dot{\boldsymbol{u}}}{|\boldsymbol{u}|} \cdot \frac{\boldsymbol{u}}{|\boldsymbol{u}|}\right)\frac{\dot{\boldsymbol{u}}}{|\boldsymbol{u}|} \tag{2.27}$$

Note that (2.27) is not the same as $\ddot{\hat{\boldsymbol{u}}}$.

Taking the time derivative of (2.16) yields

$$\ddot{\hat{\boldsymbol{f}}}_3 = \frac{d}{dt}\frac{\dot{\boldsymbol{r}}_{los}}{|\boldsymbol{r}_{los}|} - \left(\frac{d}{dt}\frac{\dot{\boldsymbol{r}}_{los}}{|\boldsymbol{r}_{los}|} \cdot \hat{\boldsymbol{r}}_{los}\right)\hat{\boldsymbol{r}}_{los} - \left(\frac{\dot{\boldsymbol{r}}_{los}}{|\boldsymbol{r}_{los}|} \cdot \frac{d}{dt}\hat{\boldsymbol{r}}_{los}\right)\hat{\boldsymbol{r}}_{los} - \left(\frac{\dot{\boldsymbol{r}}_{los}}{|\boldsymbol{r}_{los}|} \cdot \hat{\boldsymbol{r}}_{los}\right)\frac{d}{dt}\hat{\boldsymbol{r}}_{los} \tag{2.28}$$

The derivative of $\dot{\hat{\boldsymbol{f}}}_2$ similarly follows:

$$\ddot{\hat{\boldsymbol{f}}}_2 = \frac{d}{dt}\frac{\dot{\boldsymbol{f}}_2}{|\boldsymbol{f}_2|} - \left(\frac{d}{dt}\frac{\dot{\boldsymbol{f}}_2}{|\boldsymbol{f}_2|} \cdot \hat{\boldsymbol{f}}_2\right)\hat{\boldsymbol{f}}_2 - \left(\frac{\dot{\boldsymbol{f}}_2}{|\boldsymbol{f}_2|} \cdot \frac{d}{dt}\hat{\boldsymbol{f}}_2\right)\hat{\boldsymbol{f}}_2 - \left(\frac{\dot{\boldsymbol{f}}_2}{|\boldsymbol{f}_2|} \cdot \hat{\boldsymbol{f}}_2\right)\frac{d}{dt}\hat{\boldsymbol{f}}_2 \tag{2.29}$$

where

$$\ddot{\boldsymbol{f}}_2 = \frac{d}{dt}\dot{\boldsymbol{f}}_2 = (\ddot{\hat{\boldsymbol{f}}}_3 \times \hat{\boldsymbol{S}}) + 2(\dot{\hat{\boldsymbol{f}}}_3 \times \dot{\hat{\boldsymbol{S}}}) + (\hat{\boldsymbol{f}}_3 \times \ddot{\hat{\boldsymbol{S}}}) \tag{2.30}$$

Finally, the derivative of $\dot{\hat{\boldsymbol{f}}}_1$ becomes

$$\ddot{\hat{\boldsymbol{f}}}_1 = \frac{d}{dt}\frac{\dot{\boldsymbol{f}}_1}{|\boldsymbol{f}_1|} - \left(\frac{d}{dt}\frac{\dot{\boldsymbol{f}}_1}{|\boldsymbol{f}_1|} \cdot \hat{\boldsymbol{f}}_1\right)\hat{\boldsymbol{f}}_1 - \left(\frac{\dot{\boldsymbol{f}}_1}{|\boldsymbol{f}_1|} \cdot \frac{d}{dt}\hat{\boldsymbol{f}}_1\right)\hat{\boldsymbol{f}}_1 - \left(\frac{\dot{\boldsymbol{f}}_1}{|\boldsymbol{f}_1|} \cdot \hat{\boldsymbol{f}}_1\right)\frac{d}{dt}\hat{\boldsymbol{f}}_1 \tag{2.31}$$

where

$$\ddot{\boldsymbol{f}}_1 = \frac{d}{dt}\dot{\boldsymbol{f}}_1 = (\ddot{\hat{\boldsymbol{f}}}_2 \times \hat{\boldsymbol{f}}_3) + 2(\dot{\hat{\boldsymbol{f}}}_2 \times \dot{\hat{\boldsymbol{f}}}_3) + (\hat{\boldsymbol{f}}_2 \times \ddot{\hat{\boldsymbol{f}}}_3) \tag{2.32}$$

The acceleration rates of the sensor frame with respect to the inertial frame,$^i[^i\boldsymbol{\alpha}^s]$, become the time derivative of (2.26). Therefore

$$\begin{bmatrix} 0 & -\alpha_3 & \alpha_2 \\ \alpha_3 & 0 & -\alpha_1 \\ -\alpha_2 & \alpha_1 & 0 \end{bmatrix} =^i [^i\dot{\boldsymbol{\Omega}}^s] = \begin{bmatrix} ^i\ddot{\hat{\boldsymbol{f}}}_1 & ^i\ddot{\hat{\boldsymbol{f}}}_2 & ^i\ddot{\hat{\boldsymbol{f}}}_3 \end{bmatrix} {}^sC^i + \begin{bmatrix} ^i\dot{\hat{\boldsymbol{f}}}_1 & ^i\dot{\hat{\boldsymbol{f}}}_2 & ^i\dot{\hat{\boldsymbol{f}}}_3 \end{bmatrix} {}^s\dot{C}^i \tag{2.33}$$

Using (2.22), the equation for the acceleration rates in the inertial frame can be expressed as

$$\begin{bmatrix} 0 & -\alpha_3 & \alpha_2 \\ \alpha_3 & 0 & -\alpha_1 \\ -\alpha_2 & \alpha_1 & 0 \end{bmatrix} = \begin{bmatrix} {}^{i}\ddot{\hat{\boldsymbol{f}}}_1 & {}^{i}\ddot{\hat{\boldsymbol{f}}}_2 & {}^{i}\ddot{\hat{\boldsymbol{f}}}_3 \end{bmatrix} \begin{bmatrix} {}^{i}\hat{\boldsymbol{f}}_1 & {}^{i}\hat{\boldsymbol{f}}_2 & {}^{i}\hat{\boldsymbol{f}}_3 \end{bmatrix}^T + \begin{bmatrix} {}^{i}\dot{\hat{\boldsymbol{f}}}_1 & {}^{i}\dot{\hat{\boldsymbol{f}}}_2 & {}^{i}\dot{\hat{\boldsymbol{f}}}_3 \end{bmatrix} \begin{bmatrix} {}^{i}\dot{\hat{\boldsymbol{f}}}_1 & {}^{i}\dot{\hat{\boldsymbol{f}}}_2 & {}^{i}\dot{\hat{\boldsymbol{f}}}_3 \end{bmatrix}^T \tag{2.34}$$

Once the right hand side of (2.34) is evaluated, the values for ${}^{i}\alpha_1^b$, ${}^{i}\alpha_2^b$, and ${}^{i}\alpha_3^b$ are obtained by inspection of the resulting skew symmetric matrix. Having calculated the acceleration rates in the inertial frame, a simple transformation to the spacecraft body frame is accomplished using ${}^{b}C^{i}$ with (2.3).

The elegant and simple form of (2.26) and (2.34) do not imply the solution is simple. On the contrary, each step builds on the previous derivation and results. Every equation from (2.15) to (2.32) are needed in order to produce a result with (2.34).

2.6 Summary

This chapter derived a new set of equations that define the precise attitude and motion, in both angular rates and accelerations, required to properly target a moving object from a moving overhead sensor. Without them, a sensor cannot ensure that it is pointing at the correct target and will remain pointing at the right target with little to no control effort needed.

These equations are an original contribution to the published body of knowledge because they include both rate and acceleration equations for a target at a given time without assumption of a particular target or sensor motion. These equations do not rely on tracking a particular attitude trajectory, but are able to precisely define the conditions for a targeting maneuver at a given instant in time. Since the final maneuver time is normally unknown, these equations represent the fundamental boundary conditions needed to create operational targeting maneuvers.

THIS PAGE INTENTIONALLY LEFT BLANK

CHAPTER 3:
Increasing Platform Agility Using Optimal Control

Maximizing the number of images collected by a particular sensor is dependent on how efficiently that sensor can slew between targets. The faster a sensor can maneuver, the more targets it can conceivably collect [2].

While many papers have been published on optimal maneuvering for satellites, a few stand out as ground breaking. Bilimoria and Wie proved three-axis maneuvers using the eigenaxis are not time-optimal even with spherical bodies [44], Shen and Tsiotras expanded optimal control applications to axisymmetric bodies [45], and Ross et al. further extended optimal control to more realistic asymmetric bodies [46]. Solving optimal maneuver problems using pseudospectral techniques has been described in [16, 47, 48] and flight-proven on orbit with operational space systems such as the NASA Transition Region and Coronal Explorer spacecraft [21, 49, 50] and the International Space Station [51].

For the most part, the optimal maneuvering problems solved in the literature are R2R (meaning the initial and final body rates are zero). Even though eigenaxis R2R maneuvers have been shown to be sub-optimal, they continue to serve as a benchmark against which to measure a particular algorithm or maneuver controller performance [10–12, 14–22].

This chapter demonstrates how sensor agility can be improved operationally using optimal control. Time-optimal R2R maneuvers are first compared to standard eigenaxis maneuvers so that a new method of estimating the performance benefit of optimal control maneuvering and comparing different maneuvering algorithms can be discussed. NR2NR optimal control maneuvers are then introduced and demonstrated, expanding the body of time-optimal control maneuvering literature beyond R2R. Additionally, specific maneuvers to connect sequential scan targets are presented and analyzed using optimal control.

3.1 Spacecraft Platform Model

This dissertation demonstrates the maneuvering performance benefit of using optimal control versus other standard methods. In order to objectively compare the performance of different algorithms, a single platform is used consistently throughout this work. The results obtained here, however, are applicable to other platforms with the precise performance being slightly different. Unless otherwise specified, the representative Imaging Spacecraft is defined by the data given in this section.

The satellite is in a low Earth orbit defined at the epoch time of 15 APR 2012, 18:15:00.0 UTCG by the following COEs. Specifically, a semimajor axis of 7049.76 km and eccentricity of 0.0018335, making it slightly non-circular. The inclination is 98.11° with an argument of perigee equal to 46°. The right ascension of the ascending node (RAAN) is 181.37° and the true anomaly equal to 73.017°.

The satellite size is 1 m x 1 m x 1.5 m, weighing approximately 150 kg. These inertia values, Table 3.1, are non-axisymmetric, making it the most general case for any given imaging spacecraft. These values are assumed constant, which is valid over the time span of a an imaging pass. In reality, these values may change over time due to appendage movement (e.g., solar panels) or fuel expenditure.

Parameter	Value (kg m^2)
I_{xx}	40.31
I_{yy}	37.83
I_{zz}	25.86
I_{xy}	0.86
I_{xz}	-3.01
I_{yz}	1.69

Table 3.1: Example Satellite Inertias

The momentum exchange devices for the example platform are four reaction wheels. The reaction wheels (RWs) are identical and modeled after the Surrey Space Technology, Ltd. 100SP-O RW [52]. Each RW is capable of producing 0.11 Nm of torque and storing up to 1.5 Nms of momentum. These limits represent τ_{max} and h_{max}, respectively. The inertia of each reaction wheel about its spin axis is 0.0028 kg·m^2 and is assumed to be constant. The RWs are configured as shown in Figure 3.1. The wheels are distributed around the +Z body axis with a spacing of 90° between each wheel. The spin axis of each RW is also offset from the X-Y plane by 35.26°. This configuration is based on the optimal four wheel configuration described by Markley et al. [53].

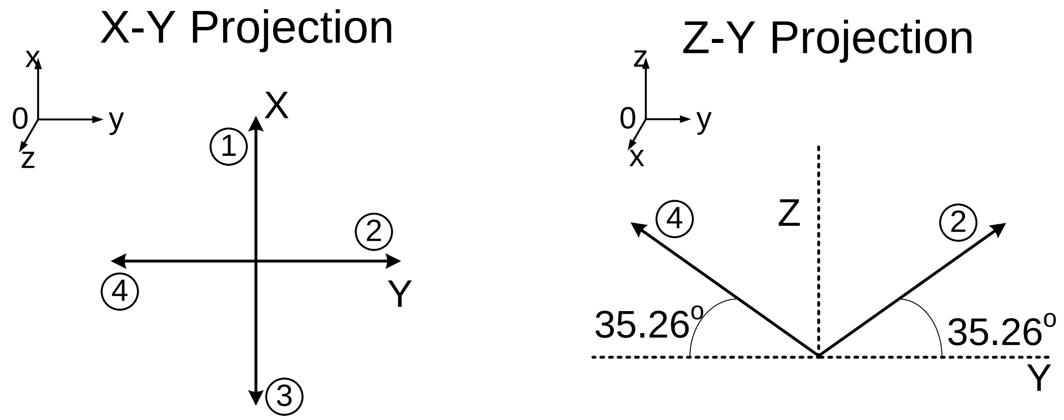

(a)

(b)

Figure 3.1: Reaction Wheel Configuration for Example Platform: X-Y Plan Projection (a), Z-Y Plane Projection (b)

3.2 Kinematic and Dynamic Equations of Motion

Spacecraft kinematics (i.e., attitude and sensor orientation) can be described using quaternions of the form, $[q_1, q_2, q_3, q_4]$, with q_4 being the scalar term. The reference frame for all quaternions in this dissertation is the body frame with respect to the inertial reference frame, so subscripts are omitted. The equation for the time derivative of the inertial quaternions is [38]

$$\dot{\mathbf{q}} = \frac{1}{2}(q_4\, {}^i\boldsymbol{\omega}^b - {}^i\boldsymbol{\omega}^b \times \mathbf{q}) \tag{3.1}$$

$$\dot{q_4} = -\frac{1}{2}({}^i\boldsymbol{\omega}^b \cdot \mathbf{q}) \tag{3.2}$$

with $\boldsymbol{q} := [q_1\ q_2\ q_3]^T$ and ${}^i\boldsymbol{\omega}^b := [{}^i\omega_1^b\ {}^i\omega_2^b\ {}^i\omega_3^b]^T$.

The spacecraft dynamics, where ${}^i\boldsymbol{\omega}^b$ is the angular rotation of the spacecraft body reference frame b with respect to the inertial frame i, are given by [38]

$$ {}^i\dot{\boldsymbol{\omega}}^b = \frac{{}^id}{dt}{}^i\boldsymbol{\omega}^b = \boldsymbol{I}^{-1}(-{}^i\boldsymbol{\omega}^b \times \mathbf{H} - \sum_n \mathbf{a}_n \tau_n) \tag{3.3}$$

where $\mathbf{a}_n$ is a unit vector representing the projection of n^{th} RW spin axis from the RW frame to the spacecraft body frame and τ_n is the torque produced by the n^{th} RW. Expanding the system momentum vector, **H** yields

$$^{i}\dot{\boldsymbol{\omega}}^{b} = \boldsymbol{I}^{-1}(-{}^{i}\boldsymbol{\omega}^{b} \times (\boldsymbol{I} \cdot {}^{i}\boldsymbol{\omega}^{b} + \sum_{n} \mathbf{a}_n \mathbf{h}_n) - \sum_{n} \mathbf{a}_n \tau_n) \tag{3.4}$$

The momentum of the n^{th} RW is $\mathbf{h}_n$ which can be defined using the individual RW speed, Ω_n, and RW inertia about its spin axis, I_{w_n}.

$$\boldsymbol{h}_n = I_{w_n}\Omega_n + I_{w_n}\boldsymbol{a}_n^{T\,i}\boldsymbol{\omega}^{b} \tag{3.5}$$

Finally, the control variable is defined as

$$\tau_n = I_{w_n}\dot{\Omega}_n \quad \forall n \tag{3.6}$$

3.3 Eigenaxis Maneuvers

The rotation of a rigid body from one attitude or orientation to another attitude is often performed around a special axis. This axis, called the eigenaxis, remains fixed in both the body frame and inertial frame for the entire maneuver [38]. A rotation through angle θ about the eigenaxis is known as an eigenaxis maneuver (Figure 3.2).

The eigenaxis slew represents a maneuver having the minimum angular distance between two attitudes. As such, an eigenaxis slew prescribes a particular path to follow and much work has been done to minimize the time needed to traverse this path. However, even for a spherical body, the eigenaxis maneuver is not time-optimal [44]. Nevertheless, due to their widespread use in industry and academic literature [38,39], eigenaxis slews are used as the standard benchmark of performance. Because an eigenaxis maneuver is, by definition, a rotation about a single axis, designing a trajectory for performing an eigenaxis maneuver is straightforward.

Minimum time maneuvers about a single axis can be implemented by applying the maximum acceleration for part of the time and the maximum deceleration for the other part. This bang-bang (BB) control profile [54] is seen in Figure 3.3(a). The application of a

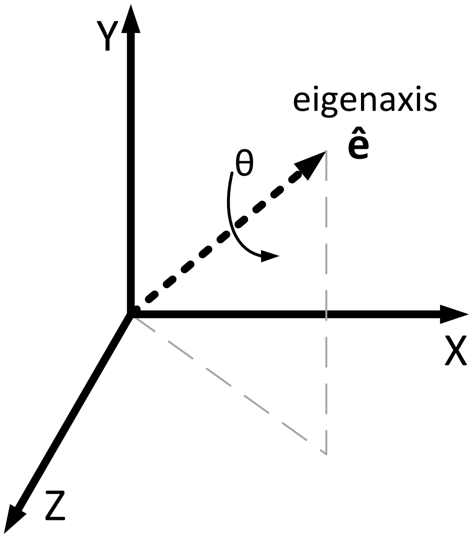

Figure 3.2: Eigenaxis in Three Dimensions

BB control results in a constantly increasing rate, followed by a constantly decreasing rate. Thus, the trajectory for ω becomes a triangle as seen in Figure 3.3(a). Maneuvers using this profile are limited only by the torque (translated into acceleration) that can be applied and are called acceleration limited maneuvers.

However, there are also times when the application of the maximum acceleration over time is such that the maximum rate is achieved before the switch time. A maximum rate is derived from the momentum storage capability of the system and results in a saturation of the angular rate forcing a coast period where the acceleration is off before commencing deceleration, hence the name bang-off-bang (BoB). The period when acceleration is applied is similar to the BB profile above, but now there is a phase of constant rate (zero acceleration) between the rate ramp up and ramp down. The resulting “trapezoid” is shown in Figure 3.3(b). Maneuvers using this profile are limited in momentum which corresponds to the maximum rate they can achieve. Thus, eigenaxis maneuvers can be divided into two categories, torque-limited and momentum-limited maneuvers or equivalently acceleration-limited and rate-limited maneuvers.

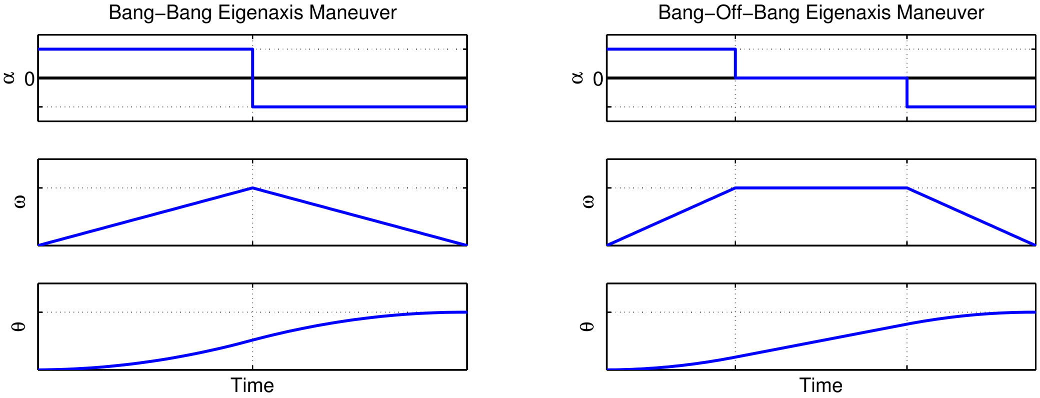

(a)

(b)

Figure 3.3: Eigenaxis Maneuver Profiles: Bang-Bang (a) and Bang-Off-Bang (b)

The task remaining is to determine the maximum acceleration and rate that can be achieved for a given spacecraft. For a single axis, the maximum acceleration that can be applied is directly proportional to the torque applied and inversely proportional to the moment of inertia about the maneuver axis.

$$\alpha = \frac{\tau}{I} \tag{3.7}$$

Finding Available Torque and Momentum about an Arbitrary Axis

Let $\hat{\boldsymbol{e}}$ be the direction vector representing the axis of rotation, $\boldsymbol{a}_i$ the direction of the spin axis for the i^{th} RW, and τ_{max} the maximum torque capability of the individual RW. The maximum torque that can be applied along a particular axis is the sum of the torques applied by each RW along this axis. By varying $\hat{\boldsymbol{e}}$ over 4π steradian and plotting the maximum torque for each axis, a maximum torque surface can be defined.

$$\boldsymbol{\tau}_{\hat{e}} = \sum_i (\boldsymbol{a}_i \cdot \hat{\boldsymbol{e}}) \tau_{max} \tag{3.8}$$

The momentum equation and resulting surface is similar to torque, simply exchanging momentum for torque in (3.8).

$$\boldsymbol{h}_{\hat{e}} = \sum_i (\boldsymbol{a}_i \cdot \hat{\boldsymbol{e}}) h_{max} \tag{3.9}$$

Consequently, examples are presented using torque but apply equally to momentum as the resulting maximum envelopes are identical in shape.

Unless the shape of the torque envelope is perfectly spherical, there exists certain axes about which the system will generate more torque than other axes. Correspondingly, there are also axes about which the system will produce less than the maximum torque. For example, using three orthogonal RWs results in a cube shaped torque envelope [53] as shown in Figure 3.4. If τ_{max} is the max torque capability of a single RW, the maximum system torque in the X-Y plane is 1.41 τ_{max} along an axis that is 45° off of the $\boldsymbol{X}$ axis (the diagonal of the square). However, along the the $\boldsymbol{X}$ axis, the maximum system torque is τ_{max}. The specific axis of maximum torque is a function of the number of RWs, their orientation, and individual torque and momentum capacity.

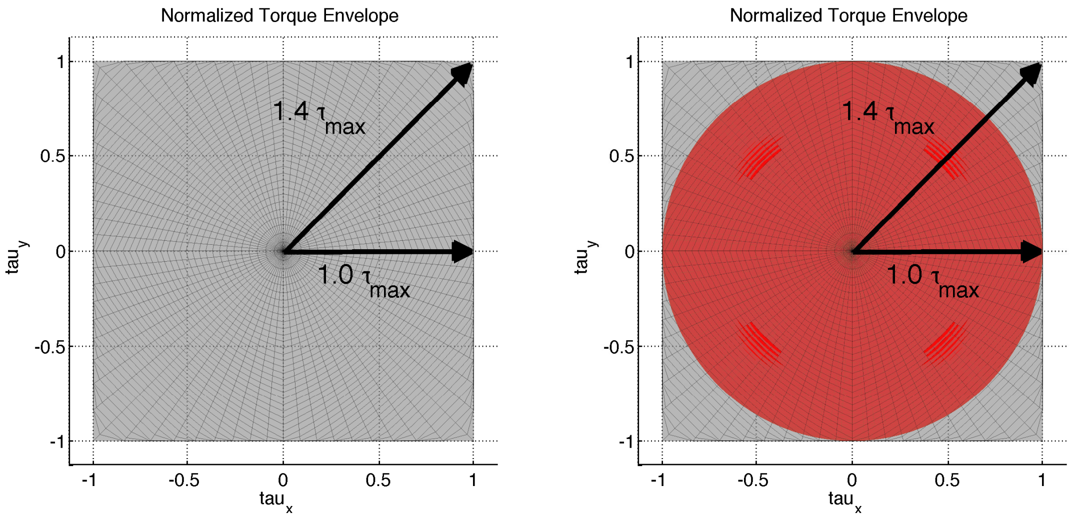

(a) (b)

Figure 3.4: Maximum Torque Examples for Non-spherical (a) and Spherical (b) Envelopes

Constraining the available torque to the smallest maximum value achievable for any axis, creates a spherical torque envelope, shown in red in Figure 3.4(b). This spherical constraint allows a maneuver planner to design a maneuver about any axis base don a single torque value. This approach is a simplification of the system capability imposed by the maneuver designer and not a physical limitation of the system.

Markley et al., [53] described an algorithm to design a RW array to achieve the largest spherical torque. For a four wheel system, the maximum spherical torque is 1.63 τ_{max} or 0.180 Nm, using the example system presented. Figure 3.5 shows the three-dimensional torque envelope as well as the X-Y and X-Z projections. The Y-Z projection is omitted because it is identical to X-Z. The largest maximum torque is found along the $\boldsymbol{Z}$ axis and is equal to 2.31 τ_{max} or 0.254 Nm. The corresponding largest and smallest maximum spherical momentum values are 2.31 h_{max} or 3.47 Nms and 1.63 h_{max} or 2.45 Nms, respectively.

Finding Inertia about an Arbitrary Axis

In contrast to finding torque about an arbitrary axis, the inertia about a given axis, $\hat{\boldsymbol{e}}$, is found using a similarity transform

$$\boldsymbol{I}_{\hat{\boldsymbol{e}}} = \hat{\boldsymbol{e}}^T \boldsymbol{I} \hat{\boldsymbol{e}} \tag{3.10}$$

Plotting the values of $\boldsymbol{I}_{\hat{\boldsymbol{e}}}$ over 4π steradian results in the shape [39] shown in Figure 3.6. The non-axisymmetric nature of inertia for the example spacecraft is evident because the X-Z and Y-Z projections are not identical. The largest inertia value is 41.0 kg·m^2 and is equal to the largest principal moment of inertia in section 3.1. The smallest inertia is 25.0 kg·m^2 (i.e., smallest principal moment of inertia).

3.3.1 Defining Agility

If (3.7) gives the angular acceleration about a given axis, the α about every axis can be obtained by applying (3.7) over the 4π steradian volume. When plotted in three dimensions, the results of these computations is an agility ellipsoid, or agilitoid [55]. The agilitoid represents the maximum acceleration performance or agility envelope of the system and is dependent on the inertia ellipsoid and maximum torque envelope. The agilitoid for the example spacecraft is shown in Figure 3.7.

Rather than calculate the maximum acceleration for every possible maneuver axis, it is easier on the maneuver designer [39] to define a single maximum acceleration that will ensure all maneuvers are within limits and can actually be executed by the platform.

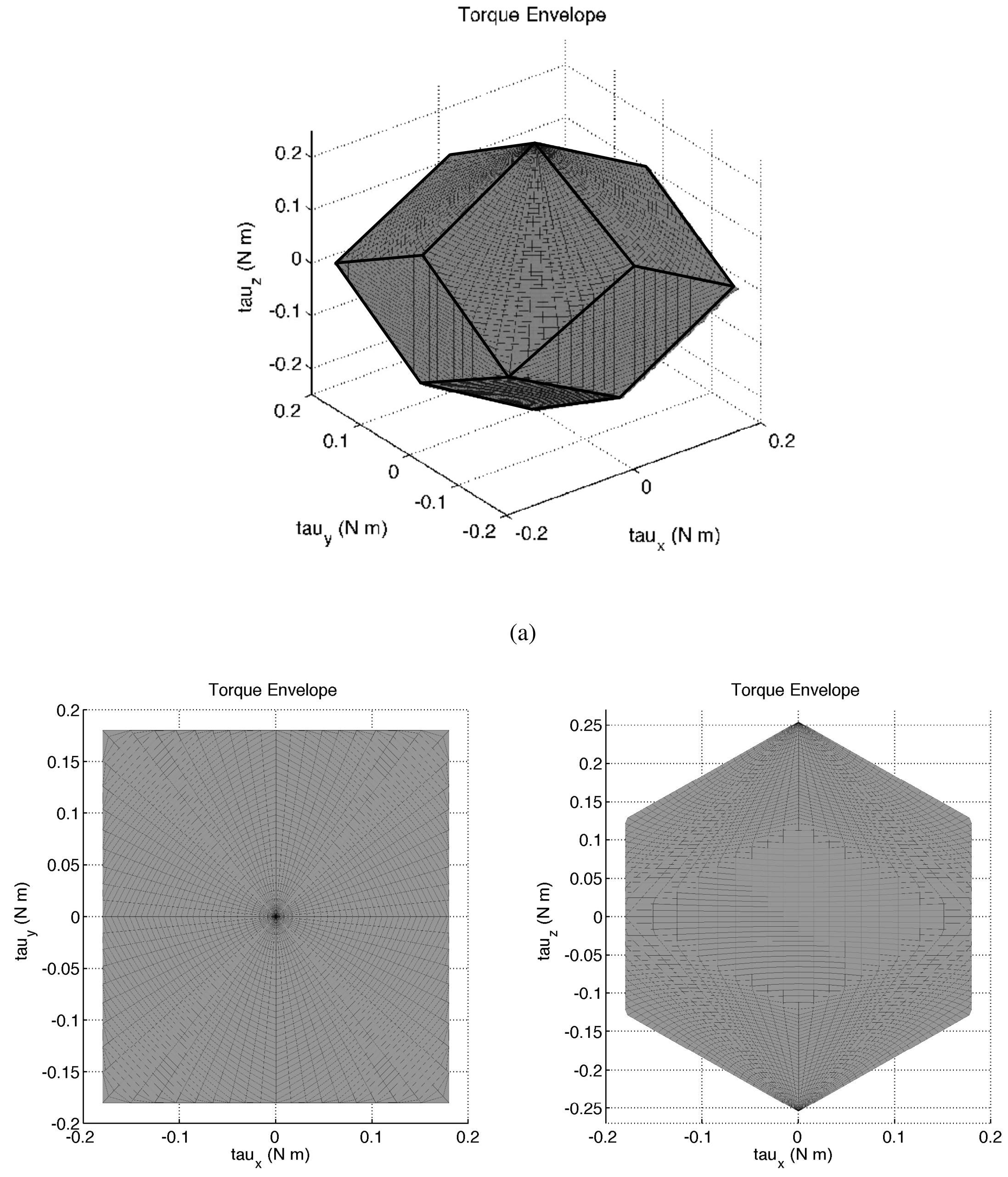

(a)

(b)

(c)

Figure 3.5: Torque Envelope in 3-D (a), X-Y Projection (b), and X-Z Projection (c)

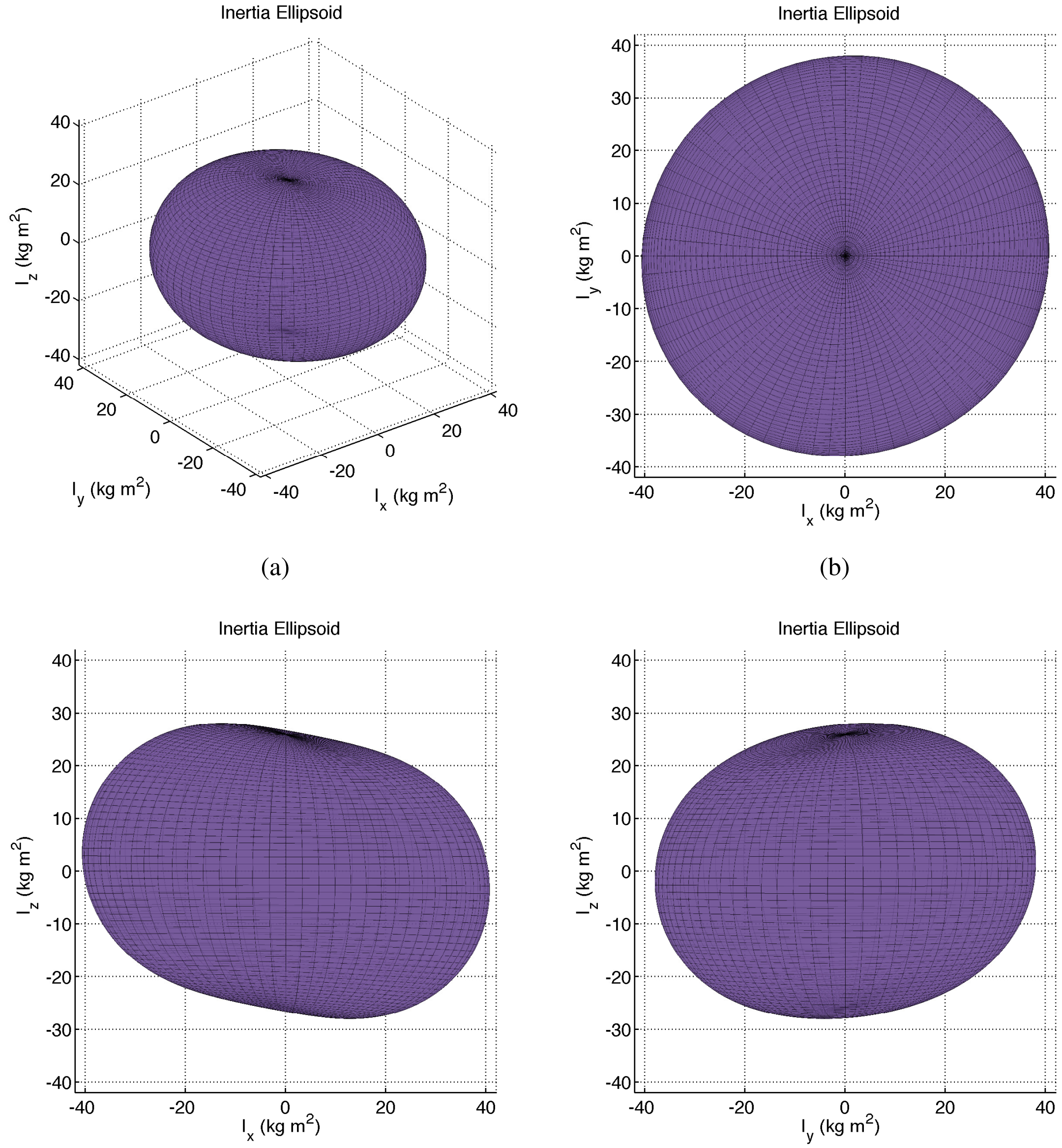

(a) (b)

(c) (d)

Figure 3.6: Inertia Ellipsoid in 3-D (a), X-Y Projection (b), X-Z Projection (c), and Y-Z Projection (d)

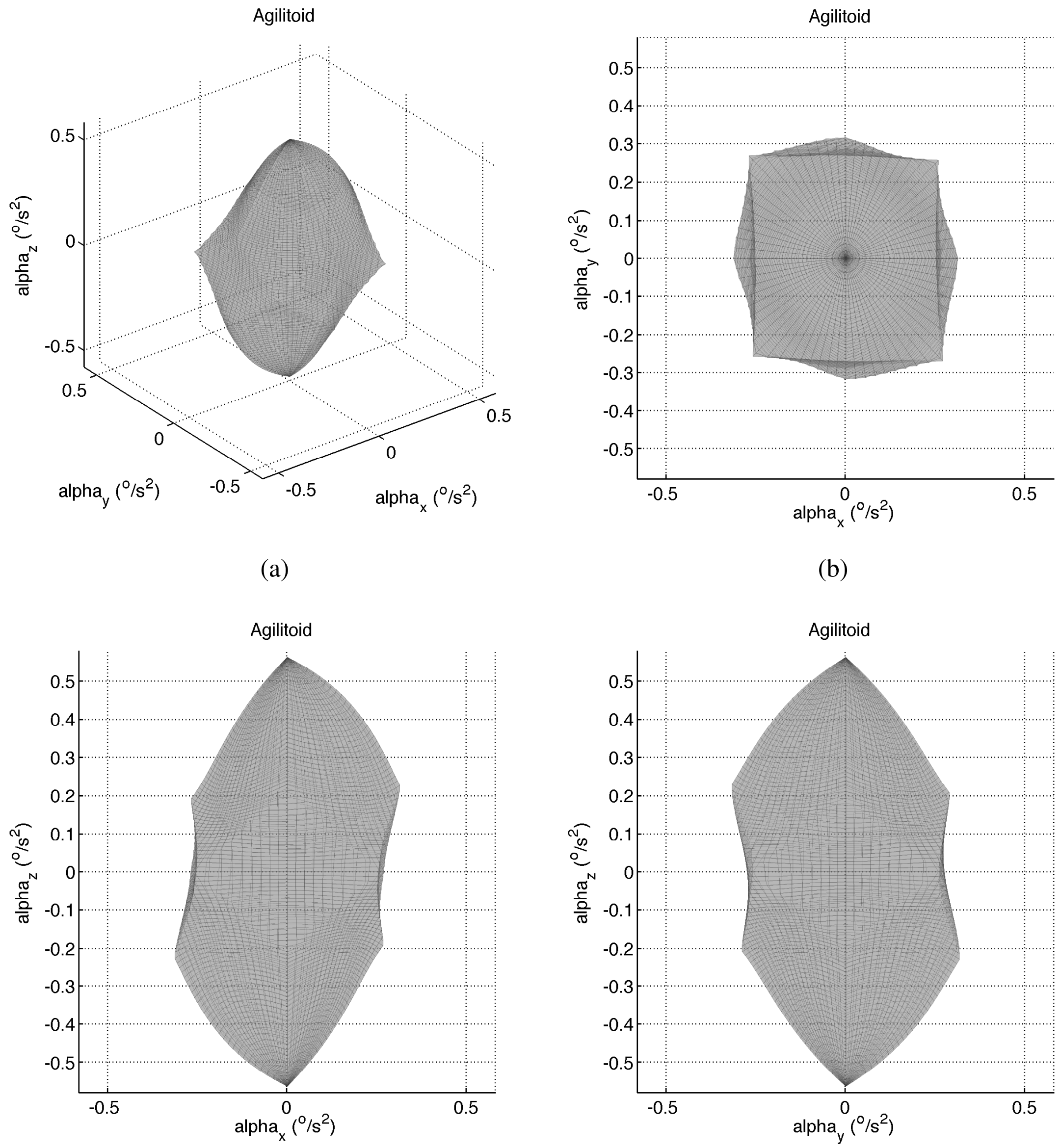

(a) (b)

(c) (d)

Figure 3.7: Agilitoid in 3-D (a), X-Y Projection (b), X-Z Projection (c), and Y-Z Projection (d)

Given the relationship of τ and I to α, this requires that the smallest maximum torque and largest moment of inertia. Any other combination may result in a commanded torque or momentum that cannot be executed for every axis. The maximum acceleration can be found by increasing the numerator and decreasing the denominator of (3.7) to their respective extremes, where τ_{min} is the smallest maximum torque from the torque envelope.

$$\alpha_{max} = \frac{\tau_{min}}{I_{max}} = \frac{0.180\text{ Nm}}{41\text{ kg}\cdot\text{m}^2}\left(\frac{180^\circ}{\pi}\right) = 0.25^\circ/\text{s}^2 \tag{3.11}$$

The maximum angular rate is similarly dependent on the inertia ellipsoid and maximum momentum envelope.

$$\omega_{max} = \frac{h_{min}}{I_{max}} = \frac{2.45\text{ Nms}}{41\text{kg}\cdot\text{m}^2}\left(\frac{180^\circ}{\pi}\right) = 3.4^\circ/\text{s} \tag{3.12}$$

The industry standard maneuver (ISM) is defined by limiting the angular accelerations and rates in such a way that they can always be achieved regardless of the axis of rotation. This means that the effective maximum torque is limited to a sphere so that it will produce the same maximum in all possible directions. This corresponds to the largest inscribed sphere within the torque envelope. However, this is not sufficient since acceleration is defined by both torque and inertia. Thus, the largest inscribed sphere must be inside the agilitoid, not just the torque envelope. Figure 3.8 shows the agilitoid with the inscribed industry standard spherical limit in red. The sphere is limited to the smallest α on the surface of the agilitoid, $\alpha = 0.25^\circ/s^2$. These spherical limits, found in (3.11) - (3.12), become the maximum acceleration and rate values used to design the BB or BoB eigenaxis maneuvers.

3.3.2 Critical Angle and Critical Time

Recalling Figure 3.3(a), a time optimal single axis maneuver that is acceleration-limited applies the full acceleration for half the total maneuver time. Let t_s be the switch time when the acceleration switches from positive to negative. The rate, as a function of time, is found by integrating this acceleration profile over time, but since it is piece-wise constant the integration simply becomes the equation for the line with slope $\pm\alpha$. The trajectory of θ is found by integrating the ω profile over time.

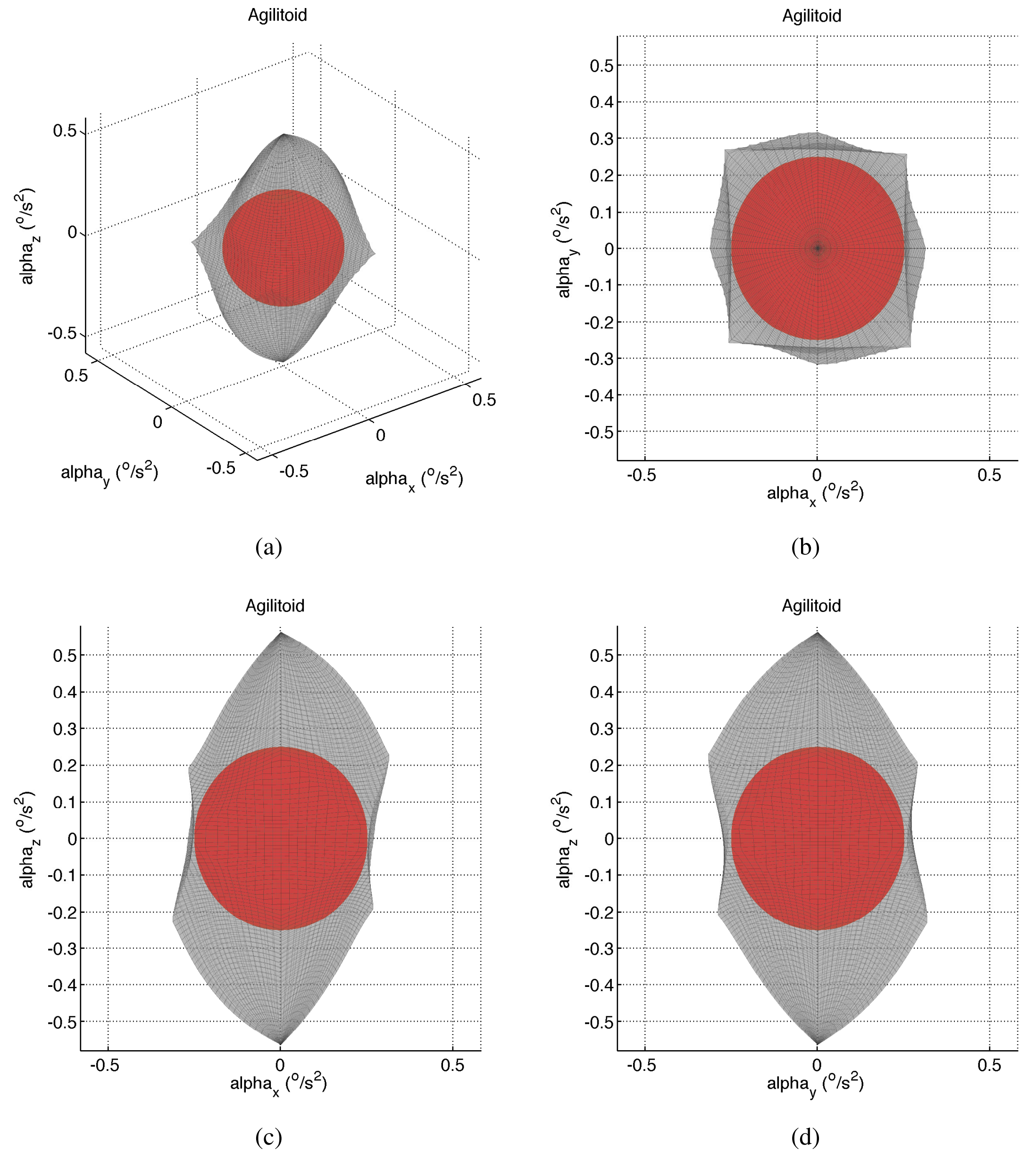

(a) (b) (c) (d)

Figure 3.8: Agilitoid with Spherical Agility Envelope Superimposed in 3-D (a), X-Y Projection (b), X-Z Projection (c), and Y-Z Projection (d)

The total time for a given acceleration-limited eigenaxis maneuver is [56]

$$t_f = \sqrt{\frac{4\theta}{\alpha_{max}}} \tag{3.13}$$

The value of ω reaches a maximum value at time ($t_s = t_f/2$). As long as this maximum value of ω is less than ω_{max}, the acceleration-limited maneuver can be performed. However, as the slew size increases, the maneuver will become rate-limited when ω reaches saturation at ω_{max}. The rate saturates at time

$$t_{crit} = \frac{\omega_{max}}{\alpha_{max}} \tag{3.14}$$

Any slew taking longer than two times t_{crit} will be a rate limited slew. For the example platform, the overall time of a maneuver that is not rate-limited must be less than two times t_{crit} or 27.2 sec. The corresponding critical angle, θ_{crit}, is the maneuver size below which all maneuvers are acceleration limited:

$$\theta_{crit} = t_{crit}\,\omega_{max} = \frac{\omega_{max}^2}{\alpha_{max}} = 46.2^\circ \tag{3.15}$$

For all slews larger than θ_{crit}, a coast phase must be included where α is zero. The duration of this coast phase, t_{coast}, is computed as

$$t_{coast} = \frac{\theta - \theta_{crit}}{\omega_{max}} \tag{3.16}$$

Thus, the overall time for a BoB maneuver is given by:

$$t_{BoB} = \frac{\theta}{\omega_{max}} + \frac{\omega_{max}}{\alpha_{max}} \qquad , \quad \theta > \theta_{crit} \tag{3.17}$$

A plot of the slew time versus angle for eigenaxis rotations is shown in Figure 3.9 with cyan and red curves delineating the acceleration-limited and rate-limited regions, respectively. This chart represents the baseline slew performance that can be used to benchmark any algorithm for improving agility.

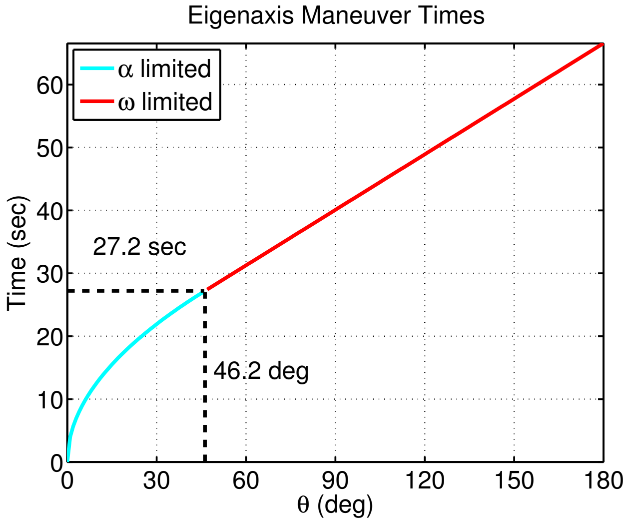

Figure 3.9: Eigenaxis Rest-to-Rest Maneuver Performance

3.4 Increasing Performance with Larger Reaction Wheels

If faced with the desire for greater agility, the most common approach is to increase the size of the RWs. If the α_{max} and ω_{max} max are increased because of larger RWs, it naturally results in a shorter total time to slew. Therefore, let a performance factor γ be applied such that $\alpha_{new} = \gamma\, \alpha_{old}$ and $\omega_{new} = \gamma\, \omega_{old}$. The resulting time for an acceleration limited maneuver would be

$$t_{BB_{new}} = \sqrt{\frac{4\theta}{\gamma\, \alpha_{max}}} \tag{3.18}$$

Let the ratio of the new time to the old time be called the time efficiency factor, η:

$$\eta = \frac{t_{f_{new}}}{t_{f_{old}}} \tag{3.19}$$

For BB maneuvers, η is related to γ, using (3.18), by the following equation

$$\eta_{BB} = \frac{1}{\sqrt{\gamma}} \tag{3.20}$$

For the rate-limited maneuvers,

$$t_{BoB_{new}} = \frac{\theta}{\gamma\, \omega_{max}} + \frac{\omega_{max}}{\alpha_{max}} \tag{3.21}$$

The efficiency factor for rate-limited maneuvers starts equal to the acceleration-limited efficiency at the point when ω reaches saturation, then steadily increases as the maneuvers get longer due to the difference in slopes (see Figure 3.10). The ratio of slopes in the rate-limited regime is given by $1/\gamma$.

The increased acceleration, combined with a similar increase in ω_{max} means that the critical time to become rate-saturated remains constant according to (3.14). However, the angle traveled during this time increases by the factor γ

$$\theta_{crit_{new}} = \gamma\, \frac{\omega_{max}^2}{\alpha_{max}} = \gamma\, \theta_{crit_{old}} \tag{3.22}$$

resulting in a given maneuver remaining in the acceleration-limiting region longer, as expected when using a larger RW. A example of the decreased slew time versus angle for any eigenaxis rotation, using a $\gamma = 1.5$ factor is shown in Figure 3.10. It is plotted showing the original performance as a baseline.

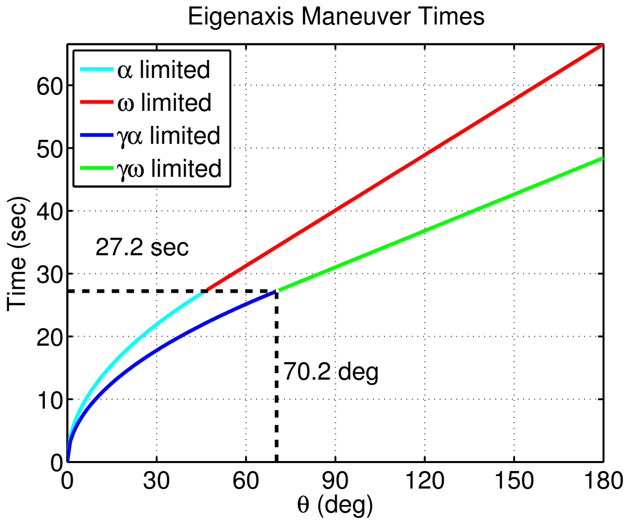

Figure 3.10: Eigenaxis Performance, with $\gamma = 1.5$

Effects of Control Allocation

To implement the maneuver, the requested system torque must be allocated to the RWs. Control allocation is very straightforward if there are only three RWs and becomes more complicated as the number of RWs rise. There are several methods for allocating torque commands to individual RWs including Markley's iterative method [53]. A more common transformation from the system frame to the RW frame is the pseudoinverse [13, 38, 39]. The transformation from RW to body frame is done using $\boldsymbol{a}$, where $\boldsymbol{a} = [\boldsymbol{a}_1|\boldsymbol{a}_2|...|\boldsymbol{a}_n]$ and is a $3\ x\ n$ matrix for n RWs. Because this matrix is not square (for $n > 3$), it is not directly invertible. The Moore-Penrose pseudoinverse ($\boldsymbol{a}^+$) maps the three desired system torques into the n individual RW torque commands. It is the least-squares solution to an overdetermined set of equations. Essentially, the pseudoinverse allocates the system torques to the RWs while minimizing a proxy for the overall total commanded energy (energy is proportional to norm of RW torque) of the system.

$$\boldsymbol{a}^+ = \boldsymbol{a}^T(\boldsymbol{a}\boldsymbol{a}^T)^{-1} \tag{3.23}$$

Using the pseudoinverse allocation method reduces the available torque by approximately 18 percent [57]. This reduction in torque causes the pseudoinverse allocation α_{max} to be 82 percent smaller than the maximum spherical acceleration shown in Figure 3.8 (which is the ideal case). Additionally, actuator dynamics and controller uncertainty requires an additional margin be applied to the maximum acceleration [38]. However, it should be noted that, in this thesis, the example spacecraft in this work assumes a perfect allocation of torques to the individual RWs. This means that the performance of any actual system is expected to be even more conservative than the baseline system used in this work. Therefore, any application of these principles to another system must include the impact of control allocation when calculating the agilitoid volumes.

3.5 Point-to-Point Optimal Control Maneuvering

Every optimal control problem is comprised of four fundamental elements [58]: the cost or objective function, dynamic constraints, event constraints, and controls. Much has been written on optimal control formulation [54, 59] and therefore only a brief summary and any applicable examples are included here.

There are an infinite number of different optimal control problems that can be formulated simply by varying the cost function to be minimized. The optimal control problems in this section consist of minimum time problems, thus the cost to be minimized is simply the maneuver duration or $t_f - t_0$. The dynamic constraints were derived in section 3.2 and given by (3.1)-(3.6). The event constraints include the boundary conditions. Specifically, the initial and final quaternions for the maneuver. In this section, the body rates are assumed zero since the maneuvers are R2R, but the initial conditions of each RW is specified as a boundary condition. Control allocation issues are not present in this formulation because the optimal controls are the individual reaction wheel torques, $\tau_n(t)$, as opposed to the resultant body torques. In summary, the optimal control solution must determine the controls that minimize the cost function subject to the dynamic constraints and initial and final event conditions.

The R2R optimal control satellite maneuvering problem becomes determining the controls, $\tau_n(t)$, according to the following optimal control problem.

$$\min_{\tau_n(t)} \quad J = t_f - t_0$$

$$\text{subject to:} \begin{cases} \dot{\mathbf{q}} = \frac{1}{2}(q_4 \, {}^i\boldsymbol{\omega}^b - {}^i\boldsymbol{\omega}^b \times \mathbf{q}) \\ \dot{q_4} = -\frac{1}{2}({}^i\boldsymbol{\omega}^b \cdot \mathbf{q}) \\ {}^i\dot{\boldsymbol{\omega}}^b = \boldsymbol{I}^{-1}\left[-{}^i\boldsymbol{\omega}^b \times \left(\boldsymbol{I} \cdot {}^i\boldsymbol{\omega}^b + \sum_n \left(\mathbf{a}_n I_{w_n} \Omega_n + I_{w_n} {}^i\boldsymbol{\omega}^b\right)\right) - \sum_n \mathbf{a}_n \tau_n\right] \\ \dot{\Omega}_n = \tau_n / I_{w_n} \quad \forall \, n \\ q_1^2 + q_2^2 + q_3^2 + q_4^2 = 1 \quad \forall \, t \\ |\boldsymbol{h}_n| <= h_{max} \quad \forall \, n \\ |\tau_n| <= \tau_{max} \quad \forall \, n \\ \mathbf{q}(t_0) = \mathbf{q}_0 \\ \mathbf{q}(t_f) = \mathbf{q}_f \\ {}^i\boldsymbol{\omega}^b(t_0) = {}^i\boldsymbol{\omega}^b(t_f) = [0,0,0]^T \\ \boldsymbol{\Omega}(t_0) = \boldsymbol{\Omega}_0 \end{cases} \tag{3.24}$$

In this case, t_0 is given, but t_f is unknown and becomes an argument of the final solution.

3.5.1 Maneuver Verification and Validation

Necessary conditions for optimality include [56] the Hamiltonian minimization condition, transversality condition, and Hamiltonian value condition. Numeric solutions to the optimal control problem in (3.24) were obtained using a Legendre pseudospectral method [60] as implemented in the DIDO software package [61].

Each maneuver was validated using several tests including the independent verification that all constraints are satisfied. Because the final time is not fixed, the Hamiltonian Value Condition requires the control Hamiltonian to be equal to negative one. This was verified at each time step for the duration of the maneuver. Lastly, the proposed control trajectory must maneuver the system to the specified final conditions. The control solution was independently propagated using a Runge-Kutta solver within the MATLAB® ODE45 subroutine. The propagated results are then checked against all boundary conditions and verified within a specified tolerance.

3.5.2 Rest-to-Rest Optimal Control Results

Because optimal control makes use of the entire capability of a spacecraft (as embodied by the agilitoid), the resulting path does not travel along the eigenaxis. The solution for each time-optimal maneuver is called a shortest time maneuver (STM) [21]. As a baseline, 21 maneuvers were generated along each body axis, $\hat{\boldsymbol{x}}, \hat{\boldsymbol{y}}$, and $\hat{\boldsymbol{z}}$ for various maneuver lengths: from 1° to 12° in three degree increments followed by 15° to 90° in five degree increments. The time for the set of optimal slews of STMs are plotted in Figure 3.11 along with the eigenaxis ISM benchmark performance in black. The results of these 63 maneuvers were combined to calculate a mean time at each maneuver size (θ) and plotted as the dashed blue line. The maximum time and minimum time are denoted by the error bars and show the range in maneuver times over the set of optimal maneuver solutions at each θ.

The time savings for each maneuver size can be quantified as either an absolute time savings or a percentage savings. The first method yields no new insights, but the second shows a relatively constant percentage in time savings during the acceleration-limited phase followed by an increasing percentage as maneuver length grows. The increase in percentage savings is due primarily because of the higher body rates achievable using optimal control than the ISM eigenaxis maneuvers. Figure 3.12 shows the time saved as a percentage using the mean STM times versus the ISM times.

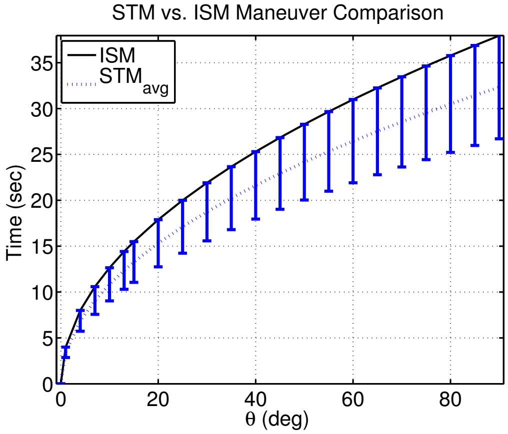

Figure 3.11: STM Performance versus ISM Benchmark

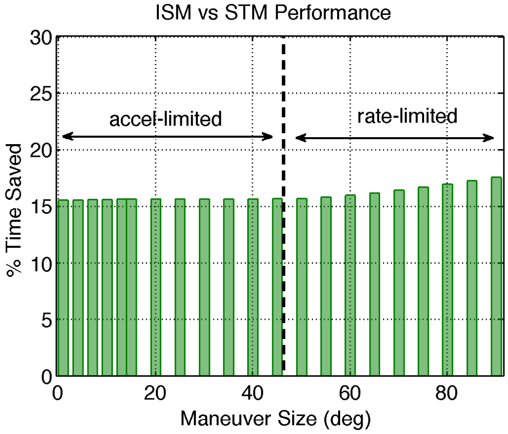

Figure 3.12: Percent Time Saved STM Mean Performance versus ISM Benchmark

Figure 3.13 shows the time efficiency, η, using the mean STM times versus the ISM times. The blue line is the value for η obtained during the acceleration-limited region. In the α limited region, $\eta = 0.84$. As maneuver length grows, the time savings is greater, causing η to decrease (i.e., better performance). During the acceleration-limited portion, η is essentially constant, therefore, this value is used for comparison purposes. It should be noted, that using a constant η is a simplification, though minor and conservative in nature. The additional decrease in η with longer maneuvers is less than seven percent of η at 90°.

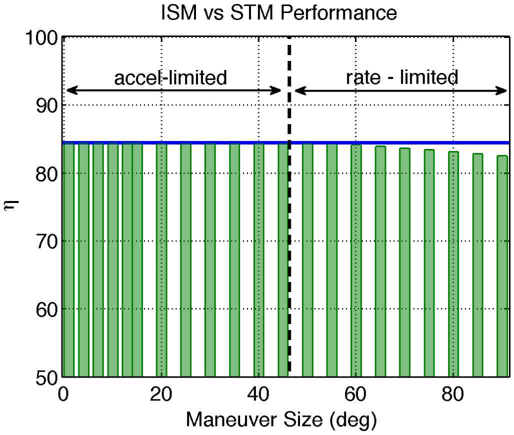

Figure 3.13: Efficiency, η, of Mean STM Performance versus Eigenaxis Benchmark

Using average η from the acceleration-limited region, one can calculate the average γ. This γ represents the equivalent increase in RW size that would be needed to obtain similar performance as the optimal control, on average, across all maneuvers. If $\eta = 0.84$, then using the reciprocal of (3.20) yields

$$\gamma = \frac{1}{(0.84)^2} = 1.41 \tag{3.25}$$

Overlaying the performance of the new γ-scaled ISM against the STM yields Figure 3.14(a). Figure 3.14(b) is a zoom in on the 30° maneuver. Each magenta dot represents an individual STM for a 30° rotation about an arbitrary axis. The axis of rotation was varied over the 4π steradian but the angular length of rotation remained constant. The left to right spread in Figure 3.14(b) is artificially created for better viewing of the over 1440 maneuvers used to cover the entire volume. The mean time of all these maneuvers is represented by the black circle at 18.4 seconds. Therefore, this γ represents the average performance when using optimal control.

3.5.3 Equivalent Eigenaxis Spherical Limit

The shape of a single time-optimal maneuver is not intuitive (see Chapter 5) and does not lend itself well to analytical comparisons with the ISM. However, as an average, the γ factor provides a possible means to accomplish this comparison or rule-of-thumb.

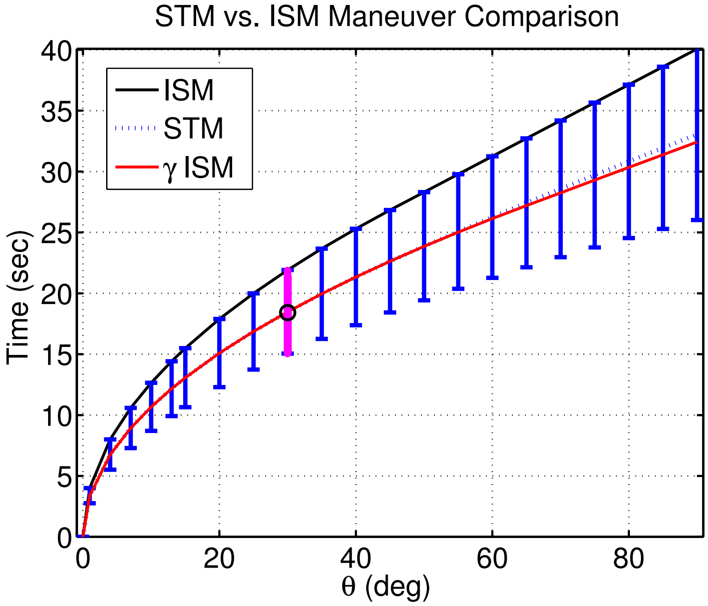

(a)

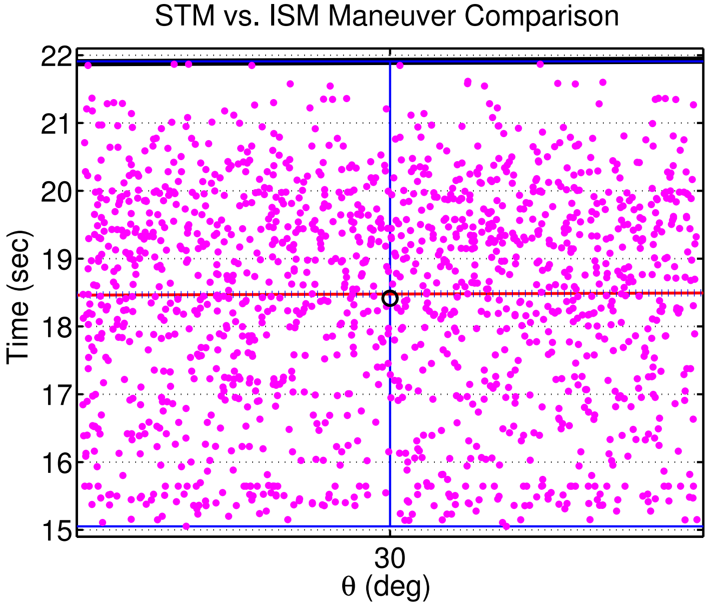

(b)

Figure 3.14: STM Performance versus ISM Benchmark: Overall Comparison (a) and Zoom in on $\theta = 30^\circ$ (b)

The concept of an optimal control equivalent eigenaxis spherical limit was first presented by Crews in [57] (though called effective eigenaxis). The concept was applied to the maximum torque envelope, but can also be applied to the agilitoid. One reason the optimal control maneuver is able to perform better is because it can use the entire volume of the agilitoid and is not limited to the spherical volume of the ISM. The increase in agility for the STM is found in the increased volume of the agilitoid. Since the volume of the agility envelope is proportional to the cube of the maximum torque (or momentum), let γ_a be defined as the cube root of the ratio of increased agility envelope volume between two maneuvers or maneuvering methods.

$$\gamma_a = \sqrt[3]{\frac{\text{agility envelope volume 1}}{\text{agility envelope volume 2}}} \tag{3.26}$$

The MATLAB® command *convhull* provides a method to calculate the volume (in addition to the convex hull) of the STM agilitoid. The volume of the ISM spherical envelope was calculated using the volume of a sphere with radius $= 0.25°/s^2$. Thus, for the example spacecraft presented here,

$$\gamma_a = \sqrt[3]{\frac{vol_{STM}}{vol_{ISM}}} = 1.41 \tag{3.27}$$

This ratio of agility volume is proportional to the average increase in actual performance obtained by the optimal control maneuvers in (3.25). Thus, a γ-scaled ISM using the equivalent spherical limit estimates the average STM performance. The equivalent eigenaxis spherical limit on α_{max} is $1.41 * (0.25°/s^2) = 0.35°/s^2$. Figure 3.15 plots this equivalent sphere in blue, with the previous agilitoid and spherical limit for comparison. Recall from section 3.4 that a pseudoinverse control allocation reduces the maximum spherical torque available by 82 percent. The γ_a between STM and pseudoinverse ISM would be equal to 1.71. This increase in value is due to the fact that the STM uses the full agilitoid capability while the pseudoinverse allocation severely limits the achievable torque and momentum.

The increased performance obtained using optimal control has a twofold benefit, depending on the particular system under evaluation. If the desire is for more performance or the system is already designed and on orbit, then the γ_a multiplier means additional performance is available in the current system if optimal control is implemented.

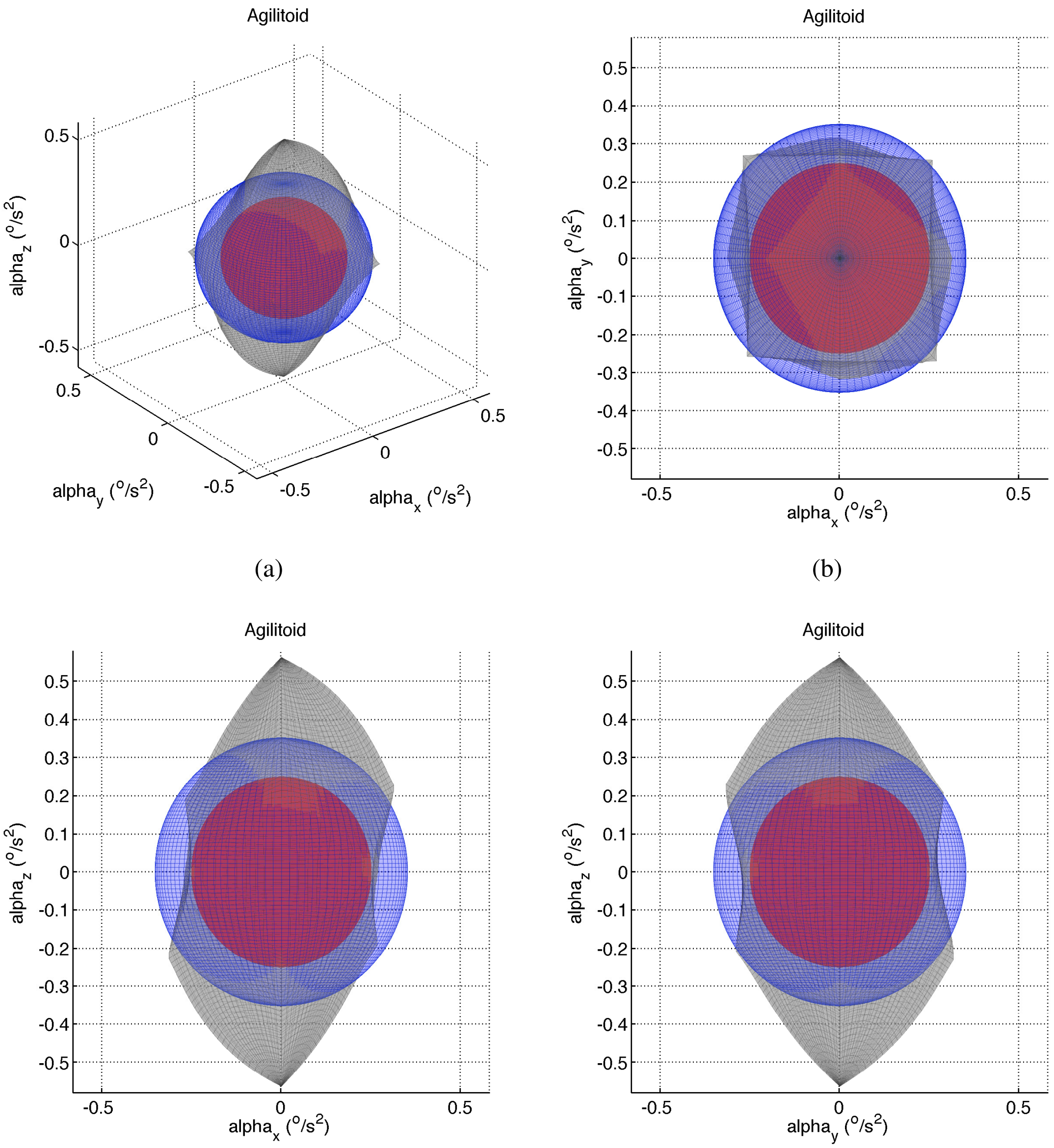

(a)

(b)

(c)

(d)

Figure 3.15: Agilitoid Superimposed with Spherical Agility Envelope and Equivalent Spherical Envelope in 3-D (a), X-Y Projection (b), X-Z Projection (c), and Y-Z Projection (d)

On the other hand, if the desire is to reduce size, weight, or power in a proposed design, then $\gamma_a > 1.0$ means the system can meet the required performance with smaller RWs. The degree of reduction is based on the increased agility obtained when using STMs. Therefore, the savings in weight and power may be significant and can be estimated as $1/\gamma_a$. For the results shown here, with a $\gamma_a = 1.4$, a system with almost 30 percent smaller RWs should still be able to meet requirements.

Time-optimal control is able to exploit the full capability of the system and therefore, yields a better performing maneuver. The ISM sacrifices performance in an attempt to simplify the maneuver design algorithm. While this may be acceptable for some missions, any mission that equates performance with profit or user value must be able to utilize the full capability of their costly asset and maximize the return on investment.

In this section, a new method has been presented to predict the average increase in performance that optimal control provides for R2R maneuvers. This method is simple and only requires calculating the volume of the agilitoid and corresponding agility envelope and evaluating their ratios to find γ_a. The agility envelope volumes should include the effects of control allocation for an accurate comparison, but estimating the performance increase does not require solving any optimal control problems.

3.6 Non-Rest to Non-Rest Maneuvering

It has been shown in Chapter 2 that R2R is a gross simplification of actual operational collections from space. R2R motion behaves intuitively and consistently for any given axis of rotation. However, the NR2NR maneuver is very sensitive to initial and final conditions. This sensitivity and the almost infinite variation in possible rates discourage an analytical solution to this problem. This dissertation extends the current body of knowledge into the realm of operational time-optimal NR2NR maneuvers.

In the optimal control framework, the NR2NR problem looks strikingly similar to the R2R problem. In formulation, it differs simply in the boundary conditions (i.e., initial and final $\boldsymbol{\omega} \neq 0$).

The full problem formulation, based on (3.24), is find the control, $\tau_n(t)$, and final time in order to:

$$\min_{\tau_n} \quad J_{slew} = t_f - t_0$$

$$\text{subject to:} \begin{cases} \dot{\mathbf{q}} = \frac{1}{2}(q_4\, {}^i\boldsymbol{\omega}^b - {}^i\boldsymbol{\omega}^b \times \mathbf{q}) \\ \dot{q_4} = -\frac{1}{2}({}^i\boldsymbol{\omega}^b \cdot \mathbf{q}) \\ {}^i\dot{\boldsymbol{\omega}}^b = \boldsymbol{I}^{-1}\left[-{}^i\boldsymbol{\omega}^b \times \left(\boldsymbol{I}\cdot {}^i\boldsymbol{\omega}^b + \sum_n \left(\mathbf{a}_n I_{w_n}\Omega_n + I_{w_n}{}^i\boldsymbol{\omega}^b\right)\right) - \sum_n (\mathbf{a}_n \tau_n)\right] \\ \dot{\Omega}_n = \tau_n / I_{w_n} \quad \forall\, n \\ q_1^2 + q_2^2 + q_3^2 + q_4^2 = 1 \forall\, t \\ |\boldsymbol{h}_n| <= h_{max} \quad \forall\, n \\ |\tau_n| <= \tau_{max} \quad \forall\, n \\ \mathbf{q}(t_0) = \mathbf{q}_0 \text{ (See Table 3.2)} \\ \mathbf{q}(t_f) = \mathbf{q}_f \text{ (See Table 3.2)} \\ {}^i\boldsymbol{\omega}^b(t_0) = {}^i\boldsymbol{\omega}_0^b \text{ (See Table 3.3)} \\ {}^i\boldsymbol{\omega}^b(t_f) = {}^i\boldsymbol{\omega}_f^b \text{ (See Table 3.3)} \\ \boldsymbol{\Omega}(t_0) = \boldsymbol{\Omega}_0 \end{cases} \tag{3.28}$$

Almost all NR2NR maneuvers, regardless of time-optimality, result in non-eigenaxis trajectories. This is because the non-zero initial and final rates force the motion away from the eigenaxis, except for the very rare case when the rates are perfectly aligned with the eigenaxis and equal. The non-eigenaxis nature of the motion violates the fundamental assumptions of the industry standard eigenaxis formulation and cannot be planned using a simple trapezoid. The ISM must be generated using a different algorithm. Hablani [42, 62] has documented a standard method for generating the NR2NR maneuvers in a single axis only. In this dissertation, Hablani's method was applied in all three axes simultaneously (while ensuring constraints were satisfied) to create the final maneuver trajectory for a NR2NR ISM.

3.6.1 NR2NR Point Target Maneuver Results

A set of nine operationally relevant maneuvers were selected for comparison. The initial and final quaternions for each NR2NR maneuver are given in Table 3.2. The initial and final body rates for each NR2NR maneuver are given in Table 3.3.

Maneuver	$q_1(t_0)$	$q_2(t_0)$	$q_3(t_0)$	$q_4(t_0)$	$q_1(t_f)$	$q_2(t_f)$	$q_3(t_f)$	$q_4(t_f)$
1	0.0411	-0.8284	0.5179	0.2092	-0.1086	-0.9143	0.3748	0.1081
2	-0.1066	-0.9106	0.3796	0.1237	0.0272	-0.8074	0.5281	0.2616
3	0.0258	-0.8025	0.5300	0.2728	0.0145	-0.8957	0.4381	0.0745
4	-0.0109	-0.8927	0.4421	0.0864	-0.0310	-0.8880	0.4349	0.1459
5	-0.0293	-0.8838	0.4389	0.1595	-0.2307	-0.8075	0.2414	0.4863
6	-0.2318	-0.7958	0.2451	0.5029	-0.3801	-0.6570	0.0458	0.6495
7	-0.3613	-0.5914	0.0539	0.7189	-0.3270	-0.6230	-0.0203	0.7103
8	-0.3275	-0.6143	-0.0131	0.7178	-0.3436	-0.6910	-0.0977	0.6285
9	-0.3430	-0.6816	-0.0925	0.6397	-0.2915	-0.7035	0.1654	0.6267

Table 3.2: Initial and Final Quaternions for NR2NR Maneuvers

Maneuver	$\omega_1(t_0)$	$\omega_2(t_0)$	$\omega_3(t_0)$	$\omega_1(t_f)$	$\omega_2(t_f)$	$\omega_3(t_f)$
1	0.0000	0.1686	-0.0845	0.0000	0.2379	-0.0375
2	0.0000	0.2442	-0.0389	0.0000	0.2343	-0.0624
3	0.0000	0.2376	-0.0620	0.0000	0.1503	-0.0634
4	0.0000	0.1541	-0.0644	0.0000	0.3096	-0.0381
5	0.0000	0.3183	-0.0383	0.0001	0.7477	-0.0107
6	0.0002	0.7350	-0.0115	-0.0806	0.1783	0.0032
7	0.0000	0.2086	0.0009	0.0000	0.2735	0.0123
8	0.0000	0.2646	0.0110	0.0001	0.3454	0.0272
9	0.0001	0.3349	0.0265	0.0004	0.6043	-0.0047

Table 3.3: Initial and Final Body Rates ($^\circ/s$) for NR2NR Maneuvers

Each time-optimal NR2NR maneuver was verified and validated using the methods described in section 3.5.1. As expected, the STM produces a faster maneuver in each case, as shown in Figure 3.16, using the same initial and final conditions as the ISM from Tables 3.2 and 3.3.

The resulting rate and acceleration magnitudes for maneuver number four are shown in Figures 3.17 - 3.18 as representative of the entire maneuver set and illustrate the differences between the ISM and STM. Hablani's approach [62] predicted the completion for maneuver four in approximately 13 seconds. Figure 3.18 shows not only the difference, but also why the multi-axis ISM time was similar to the single axis ISM. In this maneuver, the attitude motion is primarily about the Y axis and thus, it behaves very much like a single axis NR2NR maneuver. The magnitude of the rate and acceleration are plotted against the spherical limit. Note the STM acceleration is greater than the specified maximum acceleration limit for the ISM (shown by the green dash-dot line) in Figure 3.17(b). The rate is consistently higher than the ISM rate at any given time, as seen in Figure 3.17(a), and the STM completes in less time.

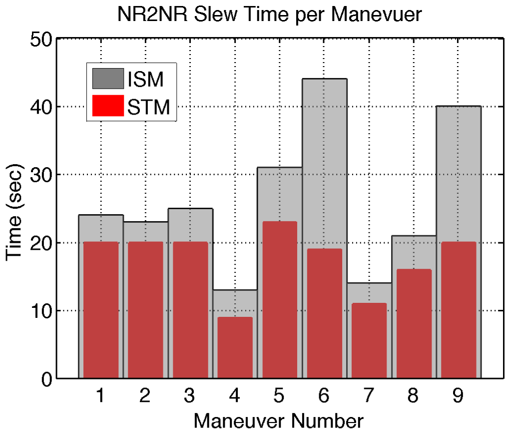

Figure 3.16: Time Savings for NR2NR Maneuvers

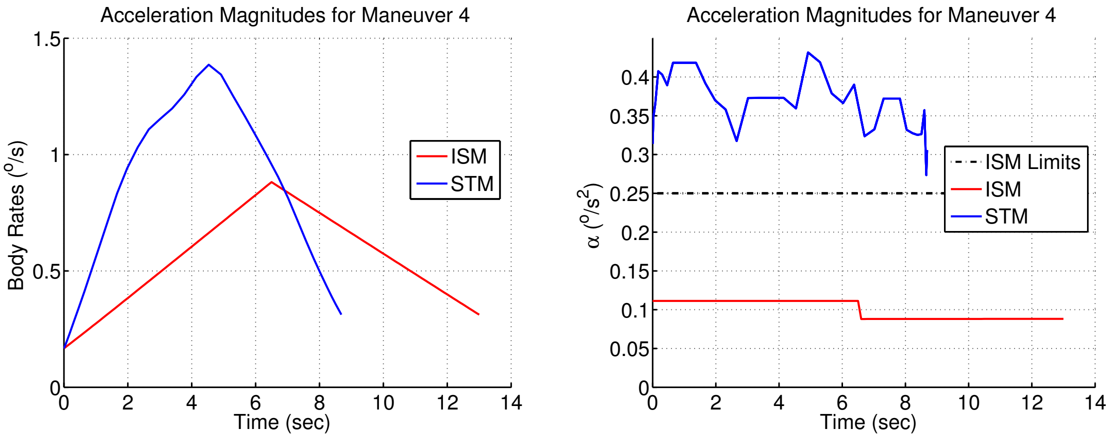

(a)

(b)

Figure 3.17: Trajectories for Maneuver 4: Body Rate (a) and Acceleration (b)

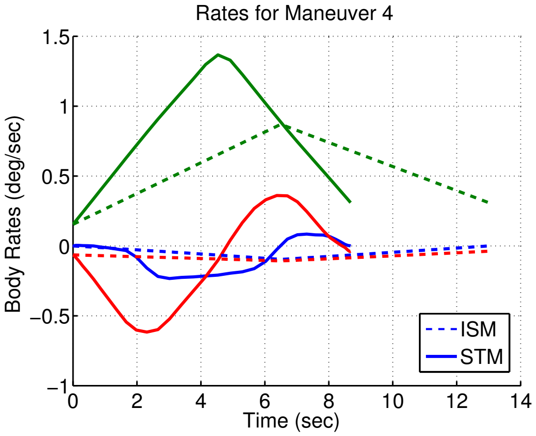

Figure 3.18: Rate Trajectory for Representative Maneuver ISM and STM_{fixed}

The total time to complete all nine maneuvers, using the industry standard method was 235 seconds. Shortest time slews for the same nine maneuvers took only 154 seconds. The time savings is significant by itself, but even more significant is the efficiency it represents. The resulting efficiencies for the nine NR2NR maneuvers is shown in Figure 3.19. For this maneuver set, the average η value is 0.70 (shown in Figure 3.19) representing an additional increase in performance for NR2NR maneuvers compared to the R2R average η of 0.84. Using (3.20), this improvement in performance translates to a γ value of 2.04, significantly higher than the R2R γ of 1.41.

The difference between these NR2NR maneuvers and the R2R maneuvers is the presence of non-zero initial and final body rates. The magnitude of the target motion or scan was the same for each target, but the scan direction was different for each target. This created the changes in initial and final rates for each maneuver seen in Table 3.3. The variation in η, from Figure 3.19, between individual maneuvers indicates that the change in system performance may be sensitive to initial conditions of rate (see section 6.2). The same NR2NR maneuvers were executed with identical but non-zero rates (i.e., every row in Table 3.3 was the same). The performance of these maneuvers very closely resembled the R2R maneuvers in η.

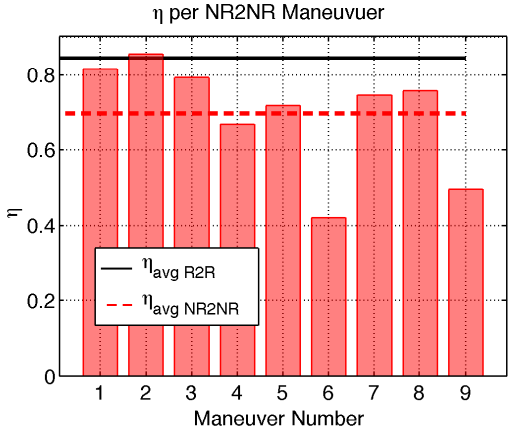

Figure 3.19: η for STM NR2NR Maneuvers

3.7 Connecting Scans

A sensor capable of both forward and reverse scanning (see section 1.3) can connect two adjacent scans as shows in Figure 3.20. The sensor simply begins the new scan with the appropriate body rates oriented along the scan direction, but there is no need to spin and reorient the sensor in order to collect the reverse scan. This maneuver is referred to as a bi-directional u-turn, but not all systems are capable of utilizing it. For this reason, this dissertation is limited to the two remaining maneuvers that are required by the more common unidirectional sensor.

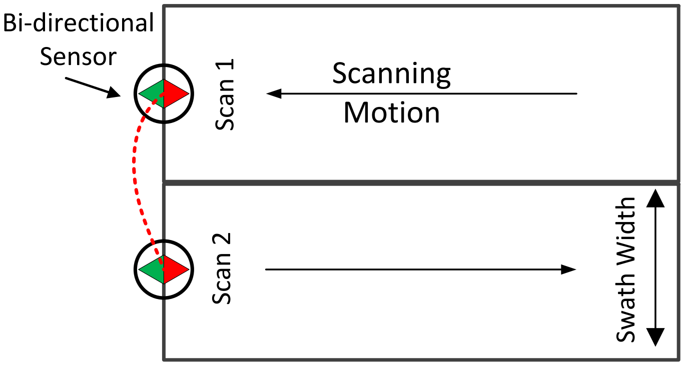

Figure 3.20: Bi-directional Scan-to-Scan Maneuvers

When a sensor is not capable of bi-directional scanning, either by design limitations or system failures, it cannot employ the maneuver shown in Figure 3.20. Instead, the satellite must maneuver to the next scan (direction and velocity), but it must also reorient the sensor such that it is aligned in the forward or nominal scan direction. Figure 3.21(a) illustrates one such maneuver. It is called the 180° u-turn, because it forces the satellite to change its apparent orientation approximately 180° from the previous scan. The second maneuver is called the 360° u-turn, or typewriter maneuver (after the similar motion of a typewriter carriage return). It is used when a sensor is incapable of reverse scan, similar to the 180° u-turn, but in this case, successive scans are required to be in the same direction over the target area (as seen in Figure 3.21(b)). These maneuvers were investigated using optimal control and compared to the corresponding ISMs .

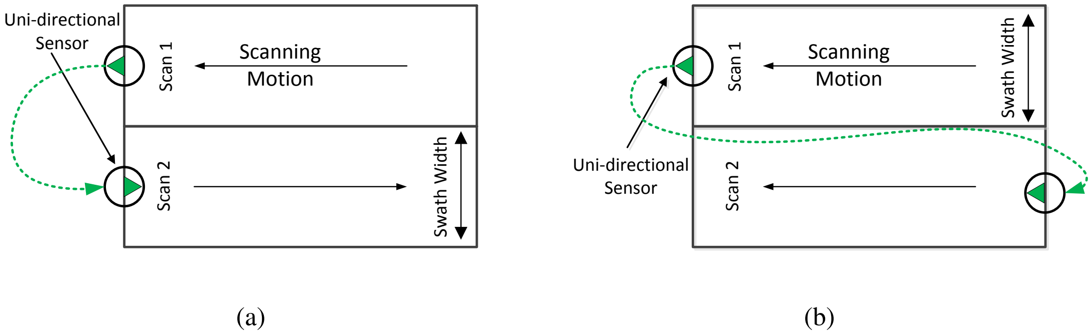

(a) (b)

Figure 3.21: Uni-directional Scan-to-Scan U-turns: 180° (a), and Typewriter (b)

Two different cases were selected to analyze this class of maneuvers. The first was a pair of adjacent scan areas essentially underneath the sensor as it passed overhead (see Figure 3.22). The second pair of scans were placed approximately 45° to the right of nadir in order to stress the off-nadir scenario. The geometry of a space-based sensor means that these two cases represent the extremes for this class of maneuver. The nadir maneuver represents the largest angular change in attitude for adjacent scans because the sensor is directly overhead. The off-nadir scan pair creates a much smaller angular change in attitudes and serves as the lower bound for this maneuver class.

The initial and final conditions for each scan-to-scan maneuver are given in Tables 3.4 and 3.5.

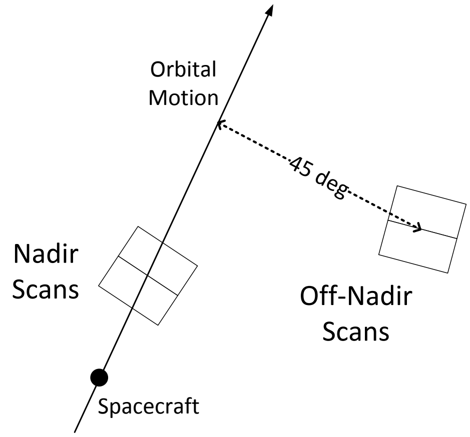

Figure 3.22: Illustration of Scan Orientation

	180° U-turn (t_0)	360° U-turn (t_0)	180° U-turn (t_f)	360° U-turn (t_f)
q_1	0.2157	0.2157	-0.2056	0.2448
q_2	0.9086	0.9086	0.8285	0.8372
q_3	-0.2130	-0.2130	0.0083	-0.1804
q_4	-0.2872	-0.2872	-0.5208	-0.4546
ω_1	0.0025 $^\circ/s$	0.0025 $^\circ/s$	-0.0041 $^\circ/s$	0.0058 $^\circ/s$
ω_2	0.7615 $^\circ/s$	0.7615 $^\circ/s$	0.6132 $^\circ/s$	0.7818 $^\circ/s$
ω_3	-0.0058 $^\circ/s$	-0.0058 $^\circ/s$	0.0006 $^\circ/s$	-0.0068 $^\circ/s$

Table 3.4: Nadir Scan U-turn Initial and Final Conditions

	180° U-turn (t_0)	360° U-turn (t_0)	180° U-turn (t_f)	360° U-turn (t_f)
q_1	0.0262	0.0262	0.3530	0.0159
q_2	-0.9161	-0.9161	-0.8277	-0.9106
q_3	0.3994	0.3994	0.3645	0.4038
q_4	0.0249	0.0249	0.2395	0.0866
ω_1	-0.0001 $^\circ/s$	-0.0001 $^\circ/s$	-0.0002 $^\circ/s$	-0.0001 $^\circ/s$
ω_2	0.20648 $^\circ/s$	0.20648 $^\circ/s$	0.3596 $^\circ/s$	0.2774 $^\circ/s$
ω_3	-0.0411 $^\circ/s$	-0.0411 $^\circ/s$	-0.0478 $^\circ/s$	-0.0362 $^\circ/s$

Table 3.5: Off-Nadir Scan U-turn Initial and Final Conditions

3.7.1 Scan-to-Scan Maneuver Results

Each maneuver type was designed based on the given initial and final conditions. The relative performance is shown in Figure 3.23 for the nadir and off-nadir scans.

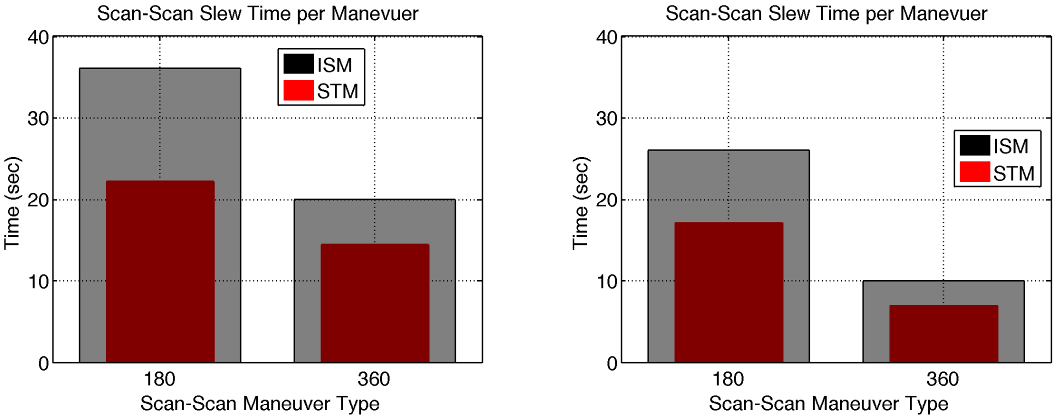

(a) (b)

Figure 3.23: Scan-to-Scan Maneuver Comparison for Nadir Scans (a) and Off-Nadir Scans (b)

Figure 3.24 shows the efficiency η for all the scan-to-scan maneuvers along with the average u-turn η value of 0.67. The significant increase in performance (i.e., lower η) by the STM is due primarily to the relative difference between initial and final rates combined with the relative size of the maneuver. As before, the STM is better able to utilize the additional capability in the agilitoid and therefore allows the maneuvers to be executed more quickly.

A simple calculation is possible to estimate the increased benefit when using STMs instead of using ISMs to connect scans. Based on a satellite in a 650 km orbit, a given point on the Earth would only be visible for approximately 820 seconds during a single pass. Let the nominal time to scan a 2500 km^2 area target be 20 seconds and the ISM slew time between successive scans be 30 seconds (see Figure 3.23). The sensor is able to collect 16 successive scans for a cumulative area of 40,000 km^2. However, using STMs between scans saves an average of 9.9 seconds per slew maneuver ($\eta = 0.67$). Applying the time savings to the above scenario, the sensor can now collect a total of 20 consecutive scans using an STM to connect each scan; four more than when using an ISM. These additional scans represent an additional 10,000 km^2 collected by the sensor when using optimal control.

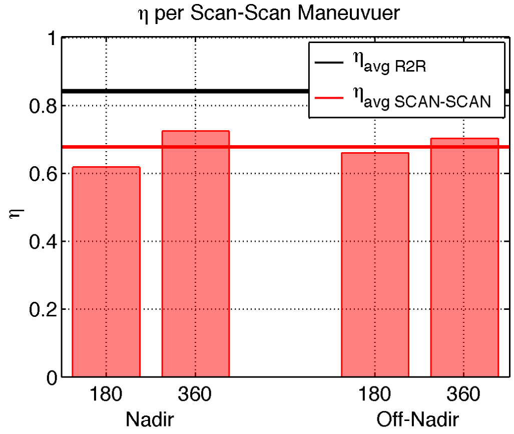

Figure 3.24: Scan-to-Scan Efficiency Using Optimal Control

The increased performance of NR2NR maneuvers creates a trend showing that the closer one gets to the operational maneuver, with all the dynamics and constraints included, the greater increase in performance is possible when using optimal control over the ISM. This increase comes from the fact that the ISM is based on a kinematic model that does not account for the full capabilities of the system. These differences are most evident during NR2NR maneuvers.

3.8 Operational Targeting with Scanning Sensors

While the increased performance of NR2NR maneuvers seen in section 3.6 is beneficial, showing up at a particular attitude, rate, and acceleration at an earlier time results in a sensor that is pointing at a different target (see Figure 1.5). Since the attitude, body rates, and accelerations are all time dependent, as demonstrated in Chapter 2, the sensor must be at the correct state at precisely the correct time in order to collect the right image.

By calculating the specific attitude, rates, and accelerations for a particular target at any given time, the correct maneuver can be generated. The nine operational maneuvers were analyzed using the initial conditions from Tables 3.2 and 3.3 . However, instead of specifying a final target state of quaternions, rates and accelerations, the maneuver end state is actually the target of interest transformed to a spacecraft state at a given time using the equation from Chapter 2. Instead of getting to the same attitude faster, the maneuver now achieves the correct attitude to image the target in the minimum time. This is yet another step closer to real operational maneuvers. Figure 3.25(a) shows the performance of real STMs (in blue) when the same initial conditions on q and ω are enforced, but allowing the final conditions of the attitude and rates to be determined using the targeting equations. The fixed STMs are defined as the same attitude and rates as the ISM, but it has already been shown that this is not operationally relevant.

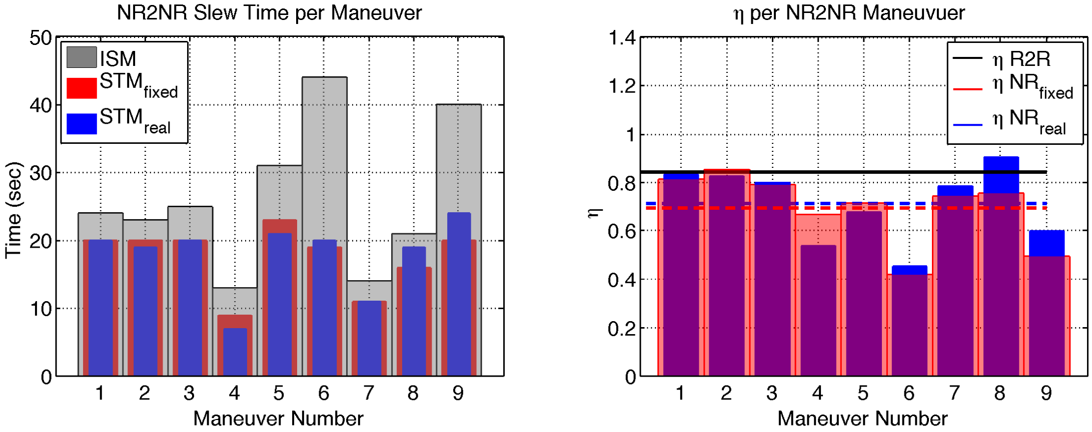

(a) (b)

Figure 3.25: Operational NR2NR Maneuvers Using Targeting: Time Savings (a) and η (b)

The resultant efficiency for the operational NR2NR maneuvers is shown in Figure 3.25(b). For this set of maneuvers, the average NR2NR η value is 0.71, which is similar to the fixed NR2NR results of 0.70 and better than the average R2R η. This slight increase in NR2NR η is due to the more realistic targets used vice maneuvering to the same attitudes. Regardless of the fixed NR2NR performance, Figure 1.5 demonstrates why the fixed attitude maneuver is not sufficient for operational image collection. Using (3.20), the improvement in performance for operational NR2NR translates to a γ value of 1.98. Recall that γ means either an increase in performance or a reduction in size/weight/power needed to meet current requirements. In this case, the reduction would be equivalent to almost 50 percent smaller RWs in order to achieve the same performance.

$$\gamma = \frac{1}{(0.71)^2} = 1.98 \tag{3.29}$$

The total time to execute these nine individual maneuvers was 162 seconds, compared to the 235 seconds for the ISM maneuvers. The savings of 73 seconds (almost 1/3 of the total ISM time) suggests that there is additional time to capture a few more targets. Applying these savings over the 100 to 1000 maneuvers in a single day with multiple passes of a single sensor could yield significant gains in overall system capability.

Using the same methodology as section 3.7.1, it is possible to estimate the increased benefit when using STM versus ISM for point targets. Based on a satellite in a 650 km orbit, a given point on the Earth would be visible for approximately 820 seconds during a single pass. Let the nominal time to collect a point target be 3.0 seconds and the ISM slew time between successive targets 20 seconds (see Figure 3.25(a)). The sensor is able to collect 35 targets on a single pass. However, using STMs between targets saves an average 5.8 seconds per slew maneuver ($\eta = 0.71$). Applying this time savings to the above scenario, the sensor can collect a total of 47 targets, 12 more than when using an ISM. At more than $\$10,000$ for each point target [63], these additional targets represent a substantial increase of $\$120,000$ in profit or value added of a single platform for a single pass simply by using optimal control maneuvering. Considering that a typical imaging satellite makes a pass every 100 minutes, the increase revenue could be more than $1.7 million a day.

3.9 Summary

This chapter demonstrated how a space-based sensor's agility can be improved using optimal control to design operational maneuvers. R2R maneuvers were defined and compared to standard eigenaxis maneuvers.

The concept of an agilitoid was presented and a new method for estimating the performance benefit of optimal control maneuvering was derived and validated for R2R maneuvers. This method requires simply calculating the volume of the agilitoid of a system, without solving any optimal control problems. A new figure of merit, γ, for comparing agility between systems was defined.

NR2NR optimal control maneuvers were formulated and demonstrated, contributing to the body of time-optimal control maneuvering literature beyond R2R. Another original contribution of this work includes a specific set of maneuvers used to connect sequential area scan targets which were presented and analyzed using optimal control.

Finally, operational NR2NR maneuvers were designed and analyzed. The performance of these operational maneuvers overcame the inaccuracies of simply arriving at the same attitude earlier by calculating the correct attitude required at the given arrival time using the new targeting equations from Chapter 2. The NR2NR maneuvers resulted in a higher γ than the average R2R maneuvers. However, it was also shown that the average R2R γ is a valid figure of merit for estimating even NR2NR maneuvers, though it may be slightly conservative. The increase in benefit from R2R to NR2NR implies that the closer one comes to modeling the real operational system and constraints, the better optimal control may perform.

In order to realize this benefit, however, a space-based sensor must be able to create an image collection plan using optimal control maneuvers. The remainder of this dissertation seeks to address this issue.

THIS PAGE INTENTIONALLY LEFT BLANK

CHAPTER 4:
Operational Image Collection Planning

The space-based image collection planning problem can be described as choosing a sequentially ordered set of collection targets, from among a larger set of available targets, that maximize a specified benefit while remaining compliant to several time-dependent constraints. The issues of relative motion, soda-straw aperture, and open-loop pointing, described in Chapters 1-3, combine to make operational imaging from space challenging.

Most of the complicating factors are related to time, making the whole problem time dependent. For example, the sensor is always in motion, due to orbital dynamics; every target is in motion, both intrinsically and due to the Earth's rotation; a particular target is not always in view of a sensor, due to its orbital motion; and the desired sensor state (attitude, rate and acceleration) corresponding to a particular target is constantly changing with the relative motion between sensor and target.

Finally, the time required to maneuver between targets also changes with time since it is a function of the initial and final state. For example, as the sensor moves along its orbit, the angle to the target changes. Figure 4.1 illustrates how the desired targeting attitude (i.e., the difference between the sensor s frame and the targeting f frame) and scan direction, $\hat{\boldsymbol{S}}$, are dependent on time and relative motion. This fact alone is enough to prevent many of the current methods from being able to solve the operational planning problem without significant simplifying assumptions. Oversimplification often neglects performance in favor of simplicity yielding a less capable collection plan and reducing overall system benefit. In order to regain the performance that is sacrificed due to planning simplifications, a new planning method must be used.

This chapter will introduce elements of graph theory by developing a base problem, $P0$. Following this, the remainder of the chapter will expand problem $P0$ into the operational, time-varying, problem faced by space-based image collection planners.

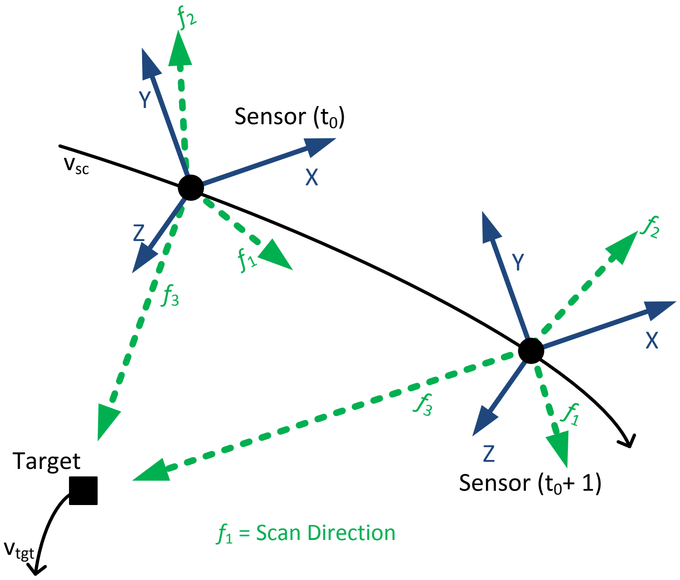

Figure 4.1: Illustration of Time-Dependent Attitude

4.1 Brief History of Orienteering

Orienteering came about as a way to teach land navigation skills to the Swedish military with the first competition held in 1893 [64]. It remains a sport today, though more popular in Europe than the United States.

In the sport of orienteering, each competitor is given a map with checkpoints and must choose which checkpoints to visit and in what order. They all begin at a particular starting location and must proceed to the finish location, collecting checkpoints along the way. The maximum number of checkpoints collected determines the winner, with completion time as a tie-breaker or discriminator. Thus, the underlying optimization task is to collect as many targets as possible in the least amount of time. Figure 4.2 illustrates a small orienteering problem (OP) prior to a solution. Variations of the OP may limit the allowable time to complete the course or increase the value of specific checkpoints based on their difficulty.

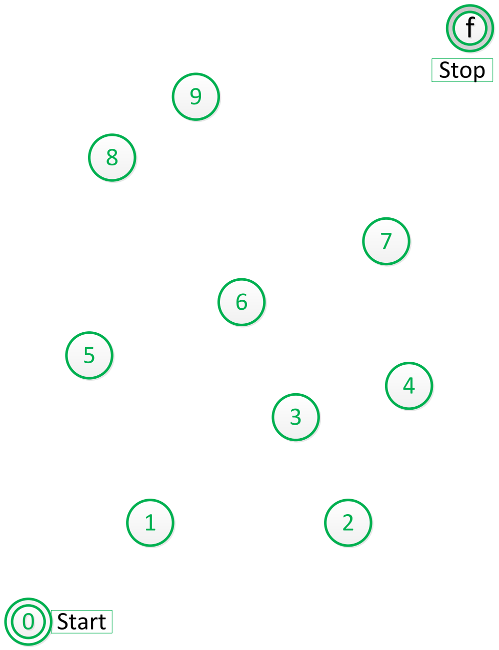

Figure 4.2: Illustrative Orienteering Problem

In the vernacular of space-based collection, the OP becomes a sensor that must collect n out of m targets and proceed from a start node to an end node while minimizing a certain cost, with the value of n unknown in advance. The similarities between the sport of orienteering and the space-based image collection planning problem naturally lends itself to comparison.

The OP is a generalization of the traveling salesman problem (TSP) because the TSP assumes every target must be collected and the start and stop nodes are identical. The TSP has been the subject of much research and [65] provides a detailed survey on the TSP class of problems. Being a generalization of the TSP, much of the TSP research is transferable to the OP. The OP is often called by other names (e.g., selective TSP [66] or prize-collecting TSP [67, 68]). An excellent survey of previous work on the OP is [69].

Previous examples of using mixed integer problems (MIPs), TSPs, and OPs for satellite applications include [70–77]. However they fall short of the full operational problem because of the simplifications made in each.

In general, the formulation presented in this work is based on [78], which uses MIP as the basis for the OP, except that this dissertation does not linearize the non-linear constraints.

4.2 Planning Problem $P0$

In order to illustrate the various concepts used to formulate the full operational planning problem, a base or fundamental problem is introduced. The base problem includes determining which targets to collect and in what sequence, along with the control trajectory and targeting times required to accomplish the plan.

4.2.1 Sensors

Using the orienteering problem as a construct, let a “competitor” be the particular sensor that is being planned by a collection planner. In this way, the planner seeks to define the "course" of a single sensor to maximize the number of targets collected.

For a given sensor, $\boldsymbol{X}$ is defined as the sensor state vector containing everything known about the sensor. It contains real valued data as well as categorical data as specific parameters that define its motion, attitude, and overall state.

Examples of the categorical data include, but are not limited to:

- Sensor type (infrared (IR), electro-optical (EO), RADAR, low resolution, high resolution)
- Platform type (satellite, UAV, land-based)
- Availability of sensor
- Platform maneuvering method (thrusters, RWs, control moment gyros, etc.)

Some examples of real-valued elements of $\boldsymbol{X}$ include:

- Orbital elements that describe sensor platform orbit
- Platform slewing constraints and limits
- Platform inertia and other dynamic motion parameters

The overall definition of the planning problem must include not only the individual elements, but also all logical and mathematical relationships between them. This work must be done prior to planning or the resultant plan may not be executable.

Sensors are used as the competitor instead of vehicles, since there may be several different types of sensors on a particular vehicle. This generalizes the problem and can accommodate both single sensor platforms as well as multi-sensor vehicles (see section 6.2).

4.2.2 Nodes

If the sensor is a competitor in the OP, then each desired collect becomes a node or vertex. Thus, an OP graph contains all the target nodes as vertices.

Let N_{tgt} be a set of all possible collects and i be the index within N_{tgt}. For every node $i \in N_{tgt}$, a data vector, $\boldsymbol{Y}_i$ is defined. In a similar fashion to $\boldsymbol{X}$, it contains everything known (or needed) with respect to node i and includes both categorical and real-valued elements. It is indexed by i to distinguish it from the data vector of other nodes.

Examples of the categorical node elements include, but are not limited to:

- Collect type (IR, EO, RADAR, low resolution or high resolution)
- Point-target or area scan
- Is this collect related to another collect? (This could be same "target" with a different sensor, or wholly different but related collect.)

Some examples of real-valued elements of $\boldsymbol{Y}_i$ include:

- Earth fixed coordinates (latitude, longitude, altitude)
- Collect size or area
- Priority of the collect

Nodes are specified as collects rather than targets because they carry an inherent tie to a specific type of sensor. For example, a target (latitude and longitude) may have two collects (nodes) associated with it, one for an infrared collect and one for a visible spectrum collect. Each collect must be serviced only by an appropriate sensor in order to be of benefit.

Node Benefit

Each collect has a benefit that can be simple constant uniform profit or a more complicated benefit value function built using multiple factors such as priority, profit, size, etc. For this initial example, the benefit of each node is assumed to be the same.

4.2.3 Arcs

If each node is a collect, then the sensor must be able to maneuver from one collect to the next. On a graph, these maneuvers or transitions are called arcs, or edges. The difference between an arc and an edge is whether or not it has a specified direction associated with its movement [65, 79]. An edge is undirected, meaning travel is allowed in either direction between the adjacent nodes. An arc is a directed edge, meaning that travel is allowed in only one direction. In general, it cannot be assumed that the travel from one node to another is reversible and symmetric, therefore, the collection planning problem is defined as a graph having only arcs and is called a directed graph (i.e., digraph). The irreversibility of motion between nodes forces the specification of two arcs for every node pair, one in each direction. This is illustrated in Figure 4.3.

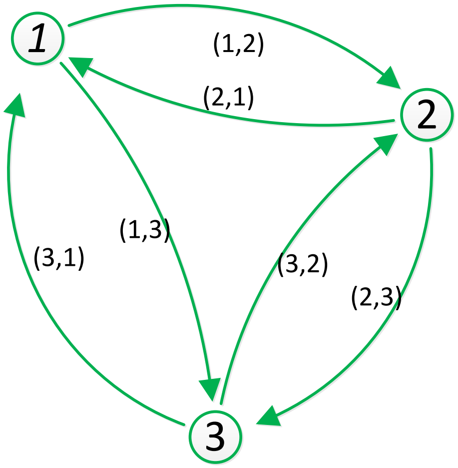

Figure 4.3: Illustration of a Directed Graph

In many cases, travel from one particular node to another node may not be feasible. However, to maintain generality, particularly for the space imaging application, every node is assumed to be completely connected with every other node by an arc representing a possible path.

Let A be a set of all arcs from node i to node j in N_{tgt}, or

$$(i,j) \in A \quad \{i \in N_{tgt}, j \in N_{tgt}\} \tag{4.1}$$

The overall structure is now described as the complete, directed graph $G = (N_{tgt}, A)$.

For every arc $(i,j) \in A$, let δt_{ij} be the weight assigned to the arc representing a resource that the planner must manage and is constrained in some way. For this example, weight $\delta_{ij} \geq 0$ represents the time spent in transit from node i to node j.

4.2.4 Path Decision Variable

The primary decisions in creating a collection plan are which nodes to collect and the path to take when collecting them (i.e., the order). These two decisions may be captured in a single variable denoted as Δ_{ij} where

$$\Delta_{ij} = \begin{cases} 1 & \text{if node } j \text{ is visited immediately after node } i \\ 0 & \text{otherwise} \end{cases} \tag{4.2}$$

Another way to look at Δ_{ij} is that a value of one means the sensor traveled on arc (i,j), from node i to node j. It also means, by definition, that nodes i and j were both visited [78]. Since the graph is a complete graph, there is never a need to pass through a node en-route to another node. Every node can be reached from every other node. Therefore, Δ_{ij} captures both the visit and path decisions.

Using the plan represented in the Figure 4.4, the corresponding Δ values are given in the Table 4.1. By evaluating the Δ values in Table 4.1, one can recreate the path through the selected nodes. Row 0 captures the arc taken from the start node to the next node. In this example, the next node is node 1 because there is a one in the 1 column. The next row shows that the arc (1,3) was taken from node 1 to node 3 by the one in the 3 column. Moving to row 3, the one in the 4 column means node 4 is the next destination. From node 4 to node 7 and so on until the final arc is taken from node 9 to the stop node f.

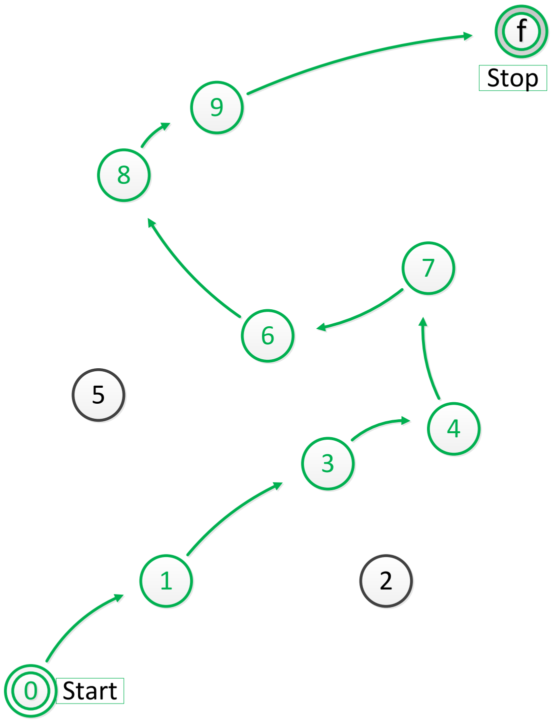

Figure 4.4: Illustrative Solution Example

Node	0	1	2	3	4	5	6	7	8	9	f
0	0	$\boxed{1}$	0	0	0	0	0	0	0	0	0
1	0	0	0	$\boxed{1}$	0	0	0	0	0	0	0
2	0	0	0	0	0	0	0	0	0	0	0
3	0	0	0	0	$\boxed{1}$	0	0	0	0	0	0
4	0	0	0	0	0	0	0	$\boxed{1}$	0	0	0
5	0	0	0	0	0	0	0	0	0	0	0
6	0	0	0	0	0	0	0	0	$\boxed{1}$	0	0
7	0	0	0	0	0	0	$\boxed{1}$	0	0	0	0
8	0	0	0	0	0	0	0	0	0	$\boxed{1}$	0
9	0	0	0	0	0	0	0	0	0	0	$\boxed{1}$
f	0	0	0	0	0	0	0	0	0	0	0

Table 4.1: Example Δ Matrix

Notice there are no ones in the first column, since there is no arc leading into the start node, just as there are no ones in the f row (no arcs leading out of the stop node). Because there are no ones in rows (or columns) 2 or 5, these nodes were never visited. Consequently, the resulting choice of nodes in sequence is $[0,1,3,4,7,6,8,9,f]$.

4.2.5 Objective Function

The goal of any collection planner is to create a plan that meets all constraints and requirements while maximizing the overall benefit or utility of the plan. In order to compare one plan against another, assuming they both meet constraints and are feasible, one must have an objective goal or measure. This objective, written as a function, is defined as the overall benefit value for a given collection plan. It is made up of the sum of the individual benefits from all the nodes visited. Determining whether or not a node is visited in a given plan relies on the decision variable Δ_{ij}. In fact,

$$\text{the number of visits to node } j = \sum_{i \in N_{tgt}} \Delta_{ij} \tag{4.3}$$

When the value of each node is the same, the benefit gained by the entire collection plan becomes the sum of the target nodes, j, visited. Thus, the objective for this base problem becomes

$$\max_{\Delta_{ij}} \quad \sum_{j \in N_{tgt}} \sum_{i \in N_{tgt}} \Delta_{ij} \tag{4.4}$$

4.2.6 Constraints

There are constraints that must be imposed on a planning algorithm to ensure it produces the plan that is feasible. Some of these constraints may be scenario specific, such as the maximum number of visits to a particular node. Others may be required for all scenarios to properly ensure that the resulting collection plan is achievable and does not violate any requirements.

Overall Resource Constraint

The overall resource constraint limits the length of the path through the targets. Without it, every target would be collected since there is no restriction to limit collection. This constraint can be a simple maximum number of targets, however, since the objective is to maximize the benefit collected, another resource should be constrained, such as time to complete the collection plan. If δt_{ij} is the time (resource) assigned to the arc (i,j), then the constraint is simply

$$\sum_{j\in N_{tgt}}\sum_{i\in N_{tgt}} \Delta_{ij}\ \ \delta t_{ij} \leq T_{max} \tag{4.5}$$

where T_{max} is the maximum time allowed for collection (normally a function of the sensor orbit which limits the visibility or access to a given target). By incorporating the path decision variable, Δ, only the resources associated with the paths taken are included in the constraint calculation.

Path Selection Constraints

The first path selection constraint is a maximum number of visits to a particular node. In some applications, more than one visit may be allowed and beneficial, but in the space imaging scenario, one visit is assumed to be the maximum. Collecting multiple images of the same node does not generally increase the benefit over a single image, within a single collection plan. Recall that a collect and a physical target are not necessarily the same (i.e., a single physical target may have multiple collect nodes associated with it depending on the type of collection desired).

If (4.3) defines the number of visits to a particular node, then a simple constraint is all that is needed. An inequality is used because not collecting a node is allowed, but the sensor cannot collect a node more than once. The binary nature of Δ_{ij} ensures that a node is not partially collected.

$$\sum_{i\in N_{tgt}} \Delta_{ij} \leq 1 \quad \forall j \in N_{tgt} \tag{4.6}$$

Another way to understand the visit constraint is that out of all the arcs leading into node j, no more than one is used.

A complete graph is a simple graph and therefore prohibits self-loops ($i = j$). However, a constraint is needed to enforce this definition and prevent the collection plan from including these arcs. This constraint forces the corresponding Δ_{ij} path variable to zero for every node.

$$\Delta_{ii} = 0 \quad \forall i \in N_{tgt} \tag{4.7}$$

Since the sensor is not allowed to stay at the node permanently, it must leave a node after collecting that node [78]. Specifically, if any node j is visited, ($\Delta_{ij} = 1$), then the sensor must also leave node j. This constraint holds for every collect node, ensuring that for every arrival at a collect node there is a corresponding departure.

$$\sum_{i \in N_{tgt}} \Delta_{ij} = \sum_{i \in N_{tgt}} \Delta_{ji} \quad \forall j \in N_{tgt} \tag{4.8}$$

4.2.7 Start and Stop Nodes

An OP, in the most general sense, must have a starting line and a finish line. It is the ability of a competitor to collect targets before crossing the finish line that measures their performance. The space imaging application of orienteering is no different. It also requires a start node and a stop node. Without these nodes, one would have to determine the target assigned to the first node and which target was the last node collected, before beginning the planning process. However, a planner does not know which nodes will be visited and in what order, thus, they cannot know which target is to be collected first. When the start and stop node are the same node it is called a depot and the orienteering path becomes a cycle (round trip) and falls into the prize winning or selective TSP class of problems.

It may also be the case that the planner has knowledge of the precise sensor data vector, $\boldsymbol{X}$, at the starting point of a collection plan for that sensor. Therefore, any formulation should allow for either known or unknown starting knowledge. The use of start/stop nodes maintains the ability of a planner to specify these nodes in scenarios when the precise start and stop conditions are known or have physical meaning. A depot implementation eliminates this option, so it should not be used for general problems. For example, a space imaging application may be planning a single pass of a spacecraft and choose to model the start node as the point when the spacecraft crosses the North Pole and stop node as the corresponding point on the South Pole. Nothing in the problem formulation should prevent such a scenario. The general formulation should be free from any artifacts associated with preconceived solution methods in order to allow as many potential methods as possible. Generally, it is assumed that a known start and stop locations/nodes are not available *a priori*. Figure 4.5 illustrates the possible paths to and from the start and stop nodes.

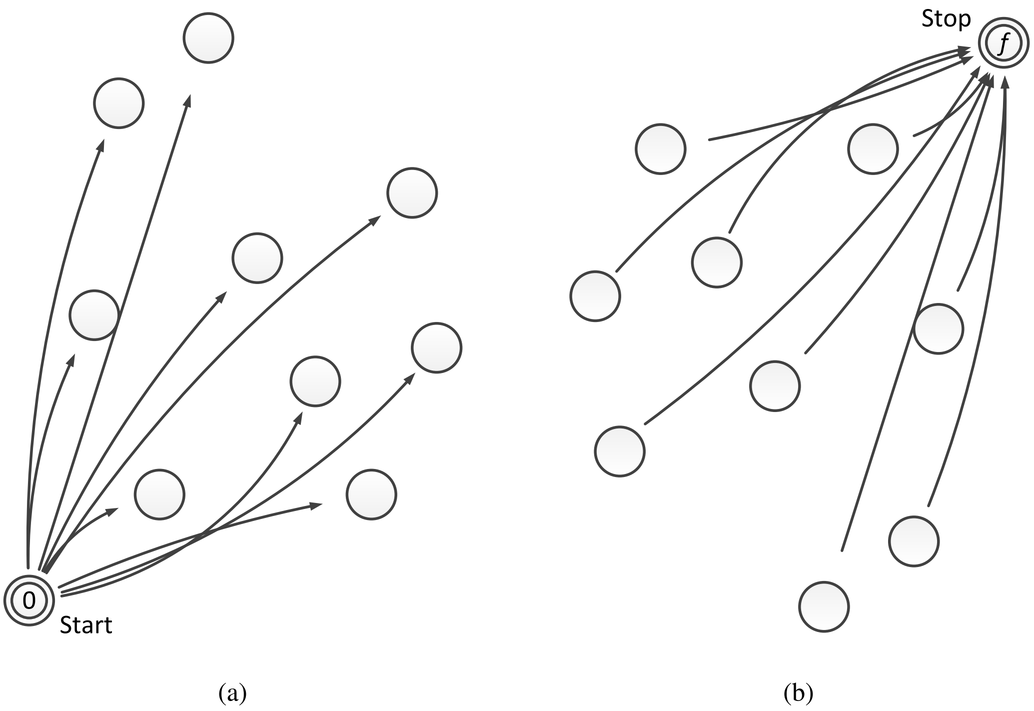

(a) (b)

Figure 4.5: Start Node (a) and Stop Node (b) Arc Examples

Additionally, the start/stop nodes must be defined in a way that they do not affect the decisions made by the collection algorithm in terms of the visits and order of the collects. Therefore, the start/stop nodes must be handled differently than collect nodes. One way to accomplish this might be to create a new set of constraints that govern only the start and stop nodes while maintaining the collect node constraints as is. A more elegant solution would be to define the start/stop nodes in such as way as to allow a single set of constraints for both collect nodes and start/stop nodes. The latter, more elegant, implementation is detailed in this dissertation.

The need for transparent start/stop nodes can be circumvented by using an additional decision variable that keeps track of the order of the selected nodes [80] and then subtracts out any effects the start/stop nodes may have induced. However, rather than adding another decision variable (with its associated constraints) to the planning construct, the current set of decision variables and constraints can be utilized, with modification, if each sensor has a particular start node and stop node defined.

The transparency of start node 0 requires that it produces no benefit for collection [81]. The data vector for the start node is not used, thus it can be defined as a null vector $\boldsymbol{Y}_0 = []$. If the start node is not allowed to affect the planning decisions, there can be no resources required to transit from the start node to any target node, $\delta t_{0j} = 0.0 \;\forall j \in N_{tgt}$.

If the graph is a complete graph, there exists an arc departing from every node and heading to the start node. These arcs are not allowed, since there can be no node visited before the start node. Rather than excluding them from the set A and disturbing the completeness of the graph (similar to [82, 83]), they are simply defined infeasible by setting $\Delta_{i0} = 0 \;\forall i \in \{N_0, N_{tgt}, N_f\}$. This declaration also eliminates the self-loop for the start node.

Similar to the start node, the stop node f must be transparent and can have no benefit. The data vector for the stop node is also defined as a null vector, $\boldsymbol{Y}_f = []$. Unlike the start node, the stop node is allowed to be the destination of an arc from a target node, however, no resources are required to travel along that arc. Thus, $\delta t_{if} = 0.0 \quad \forall i \in N_{tgt}$. At the same time, there are no feasible arcs departing from the stop node, including the self-loop. So, $\Delta_{fj} = 0 \;\forall j \in \{N_0, N_{tgt}, N_f\}$

Finally, the arc proceeding from the start node directly to the stop node is declared feasible and given a zero resource weight (time), $\delta t_{0f} = 0.0$. This will ensure that there exists at least one feasible path through the entire set of targets, even if it yields no overall benefit.

In order to ensure that the plan actually begins at the start node and finishes at the stop node, an additional pair of constraints must be included. Out of all the possible arcs leading out of start node 0, one arc must be taken and only one arc:

$$\sum_{j \in \{N_{tgt}, N_f\}} \Delta_{0j} = 1 \tag{4.9}$$

The stop node constraint ensures the corresponding condition, that one and only one arc is taken into the stop node f.

$$\sum_{i \in \{N_0, N_{tgt}\}} \Delta_{if} = 1 \tag{4.10}$$

For simplicity and compactness, a superset of nodes, N, is defined to contain all nodes, including the start and stop nodes. That is, $N := \{N_0, N_{tgt}, N_f\}$.

4.2.8 Formulation of Planning Problem $P0$

The planning problem, $P0$, can now be formulated as maximizing the set of collected targets subject to certain constraints.

$$\max_{\delta_{ij},\Delta_{ij}} \quad \sum_{j\in N_{tgt}} \sum_{i\in N_{tgt}} \Delta_{ij} \tag{4.11}$$

subject to:

$$\begin{aligned}
\sum_{i\in N} \Delta_{ij} &\leq 1 && \forall j \in N && (4.12)\\
\Delta_{i0} = \Delta_{fi} = \Delta_{ii} &= 0 && \forall i \in N && (4.13)\\
\sum_{j\in N} \Delta_{0j} = \sum_{i\in N} \Delta_{if} &= 1 && && (4.14)\\
\sum_{i\in N} \Delta_{ij} - \sum_{i\in N} \Delta_{ji} &= 0 && \forall j \in N_{tgt} && (4.15)\\
\sum_{j\in N} \sum_{i\in N} \Delta_{ij} \;\; \delta t_{ij} &\leq T_{max} && && (4.16)\\
\delta t_{0j} = \delta t_{if} &= 0.0 && \forall \{i,j\} \in N && (4.17)\\
\delta t_{ij} = \underset{\boldsymbol{u}_{ij}(t)}{\text{argmin}} \;\; J_{slew} &\left[\boldsymbol{X}, \boldsymbol{Y}_i, \boldsymbol{Y}_j, \boldsymbol{u}_{ij}(t), t\right] && \forall \{i,j\} \in N_{tgt} && (4.18)\\
\Delta_{ij} &\in \{0,1\} && \forall \{i,j\} \in N && (4.19)
\end{aligned}$$

Equation (4.12) ensures that the single visit path constraint holds, which means that each node is allowed to be collected no more than once. Equation (4.13) prevents the infeasible arcs and self-loops from being selected. Equation (4.14) forces the sensor to begin and finish at the designated start and stop nodes. Equation (4.15) ensures that if the sensor arrives at a collect node j, it must also leave that node. This constraint is applied to all collect nodes, but not to the start/stop nodes. Equation (4.16) ensures the overall plan is within the overall allowable collection time as set by T_{max}. Equation (4.17) fixes the arc weight between start or stop node and every other target at zero. It also creates at least one feasible path through all the collect nodes, directly between start node 0 and stop node f

with zero transit time. Equation (4.18) defines the individual transit time between nodes as the argument of the optimal control problem, J_{slew} and its solution. This optimal control problem is the same one described and solved in Chapter 3. Equation (4.19) ensures the decision variable remains a binary variable.

This base OP is NP-hard [84], but as will be seen, the operational problem expands on this problem making it even more challenging.

4.3 Current Methods for Addressing Problem $P0$

Presently, the space-based image collection planning challenge is claimed to being solved by a collection of proprietary methods [85, 86]. However, this challenge is most often being met by simplifying the problem to a point that it can be solved by available tools and algorithms. Even problem $P0$ is reduced further before a particular solution method is attempted.

There are several types of simplifications possible for the task of choosing the number and sequence of targets. A very straightforward simplification is to point the sensor at the correct azimuth and elevation angles needed to collect a particular target and simply wait for the precise time that target will be in view [18]. In doing so, however, no other collects can be accomplished en-route to the desired image which limits collection capacity. Target and path selection is often done iteratively using heuristics or algorithms such a greedy algorithm [87], branch-and-cut [66], evolutionary algorithms (EA) [73], or dynamic programming [86], but all are based on significant simplifications. It is also possible to select an initial subset of targets, then continue adding targets as long as the resulting solution remains feasible [83], which is another form of iterative process. This method can preclude possible solutions because they are not based on the initial target subset. At the same time, one might collect over an entire area and allow post-processing to identify the target of interest within the area image [88]. This would result in the collection of much more data than is necessary, most of which is may not be desired or useful to the customer.

Simplifications in platform performance, specifically in maneuver design, are often the biggest culprits in decreased system performance. Examples of simplifications used in maneuver design include:

- Using a simple angle metric vice slew time (e.g., ± 30° off nadir) [76, 89]
- Slew time is a proportional angle (or distance) between targets [90]
    - This is essentially equivalent to the eigenaxis R2R simplification which, demonstrated in chapter 3, results in a performance loss equivalent to reducing the size of the RW system by almost 30 percent (for the example system).
- Assume worst case maneuvering performance for all maneuvers [38, 39, 53, 62]
    - This is the most common simplification since many system specifications are based on the spherical rate and acceleration limits discussed in section 3.3
- Slew time is constant for all maneuvers (as seen in planning Tracking and Data Relay Satellite (TDRS) service windows [91])
    - This requires the worst case performance be used as the nominal slew time and is an even more conservative simplification than the spherical rate limit.
- Rates are treated as disturbances and added to the end of a R2R maneuver [31, 33]
    - This requires a penalty time be added to each maneuver in order to allow the settling of the motion and achieving of the proper rates.

A unique possibility exists for space-based platforms. Increasing the orbital altitude will achieve an increase in agility because the angles between targets get smaller with increased distance. For example, DigitalGlobe raised the orbit of GeoEye-1 and achieved an increased agility of approximately five percent [92]. However, this benefit comes with a corresponding decrease in collection quality because of the increase in distance between the sensor and the target.

Ultimately, all planned maneuvers must be executed on board a real platform. The assumptions that allowed a planner to quickly create a plan are not available to the actual spacecraft. Higher fidelity models are reserved for the final validation step prior to sending commands to the spacecraft due to cost and complexity. Ensuring the planning simplifications do not invalidate the proposed solution means accepting lower performance from the platform in order to execute the plan.

Not only is the proposed plan required to be physically executable, it must satisfy any additional operational constraints placed on the system, such as sensor capacity, keep-out zones, or temperature limits on the platform. Constraint violations require planner intervention, such as adding a dog-leg maneuver to manually circumvent an exclusion zone or eliminating an offending target [18]. These decisions are usually made with a specific focus of satisfying a particular constraint and not the overall plan benefit. If the proposed plan violates a constraint, dropping a single target may result in the constraints being satisfied. However, it is also likely that this new plan may be of lower overall benefit than a plan created that included the constraints from the beginning. For each and every validation that fails, no matter where in the process it occurs, the proposed plan must be modified to eliminate the offending issue and re-validated. Such human-in-the-loop interventions are costly in both time and effort and may further reduce overall system performance.

All of these simplifications have arisen over time because effort was focused on improving a specific piece of the overall problem. Unfortunately, the performance decay of these simplifications is compounded with every additional simplification used. For example, if every simplification carried a 10 percent reduction, then using five simplifications by a given planner would result in an overall reduction of 41 percent not just 10 percent. In order to properly solve the planning problem, one must look more holistically.

4.4 Time-Varying Problem Literature Review

In [1], Pemberton describes the inability to respond to new tasking requests in a timely fashion as a direct result of the current processes used for collection planning and makes an excellent case for why current static scheduling techniques do not work. His focus on dynamic, ad-hoc tasking illustrates one of the prime motivators for solving the operational image collection planning problem in a different way.

Though often associated with the vehicle routing problem (VRP) [93], the time dependent OP has critical timing and sequencing constraints that set it apart and make it unique, similar to the UAV application described in [94]. It is not simply an arbitrary sequencing of collects: each decision has an effect on the remaining problem.

The time-dependent nature of the full OP has not fully been addressed to date, even though many of the individual elements have been researched independently. The first reference to a time-dependent OP is [95], though it makes a simplifying assumption that the ratio between minimum and maximum travel times is constant. The temporal challenges of the planning problem were simplified by restricting the changes to linear continuous changes only in [96], however this restriction is not valid with time-optimal maneuvering.

Time windows that constrain the collection of nodes or targets are presented in [78, 93]. Independent waiting times are discussed by [80, 93], but are limited to the period before a collection event and unduly constrain the flexibility of the waiting sensor. The use of wait times in conjunction with time windows was presented in [97]. Servicing time (time spent at a node in order to collect it) was described in [78].

Time-dependent arc weights were demonstrated in various works, but all with simplification. Reference [98] based the time dependency solely on the route starting time and not on individual arc transits while [99] determined a dynamic travel time between nodes by randomly assigning a value about some mean instead of calculating them from physical performance constraints. Variable arc weights between nodes (i.e., transit time) were implemented in [100], however, travel time was simplified by restricting it to linear constraints only. Time dependent node benefits were used in [101], but the formulation does not include time as a resource to be managed. The first to include time dependent arc lengths and servicing times at each node was [102]. In [102], Pietz treats time as a resource and uses a network formulation for the OP, however the node characteristics are not time-varying or dependent on the transit time.

Choosing the targets to collect and in what sequence is often considered the outer-loop problem while determining the specific maneuvers given a path as the inner-loop part of the problem [103]. While it is possible to focus solely on the maneuvering (inner-loop) without regard to the planning (outer-loop), it is not possible to reverse that focus. The planning must include the maneuvering performance as a fundamental part of the solution. Without it, any proposed solution is not guaranteed to be feasible when it is executed on board the spacecraft. This dissertation asserts that both problems, planning and maneuvering, are elements of a single problem and the best solution to the larger problem must solve both simultaneously. Any splitting up of the problems will inevitably incur assumptions and therefore potentially discard system performance.

Throughout this work, the term “image” is used generically to represent a “collect” of target-specific information. It is not meant to be limited to visual data and is used interchangeably with “collect.”

4.5 Planning Problem $P1$

Problem $P0$ made several simplifying assumptions in order to demonstrate the concepts of the collection planning problem. This section will recast problem $P0$ in its full operational sense using similar concepts to problem $P0$. The operational space-based collection planning problem is a multi-phase problem with both continuous variables and categorical variables. The dynamic constraints governing this problem include differentiable and non-differentiable constraints.

The sensor attitude needed to collect the target is determined by the relationship between the target state and the sensor state, as shown in Chapter 2. Since both the sensor and targets may be moving, the required attitude to collect a target also changes and is associated with a particular time. The desired attitude, rates, and accelerations cannot be determined in advance without associating the time of arrival at a particular state. The challenges of solving even a moderate sized operational problem are significant.

4.5.1 Sensors

For a given sensor, $\boldsymbol{X}$ is still defined as the sensor state vector containing everything known about the sensor, but now includes additional elements that are time-varying. Some examples of potentially time-varying elements of $\boldsymbol{X}(t)$ include:

- Position, velocity, acceleration of the sensor $[\bar{r}(t), \bar{v}(t), \bar{a}(t)]$
- Estimated accuracy of location knowledge
- Sensor pointing parameters (Where is it pointing now?)
- Platform attitude parameters $[\bar{q}(t), \bar{\omega}(t), \bar{\alpha}(t)]$
- Estimated accuracy of attitude parameters
- Transformation matrix (DCM) from sensor to platform frame (time-varying)
- Sensor slewing capability parameters (used to describe the sensor's ability to point to a target)
- Sensor inertia and other dynamic motion parameters
- Current storage capacity remaining
- Current power available to the sensor for collection
- Can the sensor be slewed independent of the platform?
- Must resources for this sensor be shared with other sensors?

As an example, let a particular sensor be specified and constructed using the following data vector with the categorical variable *Type* listed first and real variables following.

$$\boldsymbol{X}(t) = \begin{bmatrix} Type \\ \bar{r}(t), \bar{v}(t), \bar{a}(t) \\ \bar{q}_0(t), \bar{\omega}_0(t), \bar{\alpha}_0(t) \\ CollectSpd \text{ (tgt units/time units)} \\ MaxCollectRange \text{ (range units)} \end{bmatrix} \tag{4.20}$$

4.5.2 Nodes

For every node $i \in N_{tgt}$, the data vector from $P0$, $\boldsymbol{Y}_i$ is also now defined as a function of time. Some examples of time related or time-varying elements of $\boldsymbol{Y}_i(t)$ include:

- Position, velocity, acceleration of collect $[\bar{r}(t), \bar{v}(t), \bar{a}(t)]$
- Estimated accuracy of location knowledge
- Time constraints for collection (due date, no earlier than, no later then, etc.)
- Collection constraints by a particular sensor type (min/max angle, min/max resolution, etc.)
- Desired collection metrics from the customer (min resolution, max range, min/max angle, etc.)
- Priority of the collect (potentially time-varying)

If the sensor is defined per section 4.5.1, then each target can then be specified (with categorical data elements first, followed by real data elements) as

$$\boldsymbol{Y}_i(t) = \begin{bmatrix} Type \\ \bar{r}(t), \bar{v}(t), \bar{a}(t) \\ Priority \text{ (benefit units)} \\ TgtSize \text{ (tgt units)} \\ MaxCollectRange \text{ (range units)} \\ DesiredCollectRange \text{ (range units)} \end{bmatrix} \tag{4.21}$$

4.5.3 Node Benefit

Problem $P1$ no longer assumes a constant and equal benefit for every target. Thus, a unique benefit value function (BVF) must be defined for each node that captures the benefit to the overall collection plan of that particular node.

The BVF is a critical element in operational collection planning. The solution to the planning problem is fundamentally dependent and sensitive to the definition of the BVF. Any simple metric such as number of images or square kilometers, cannot adequately define the value of one collection plan over another. For instance, a collection plan may collect more square kilometers, but if those square kilometers are not being requested by a customer, then the value of that plan is diminished compared to a plan that collected more profit generating images but less overall area. Ultimately, the value of each collect must be defined in terms of benefit to the end user. Satisfied users produce more requests for collection products which translates to greater revenue and profit.

The BVF for each node must be defined and specified prior to commencing the planning tasks to ensure that the highest overall benefit is represented by the selected plan. It is indexed by i, BVF_i, and is defined as a function of node data for a given sensor. For example, the BVF of a particular target may be higher when collected by a certain sensor or sensor type than when it is collected by another type. The benefit of a high-resolution image may be quantifiably higher than a low resolution image of the same target. While the BVF for each node must be defined prior to planning, this does not preclude the benefit value from changing as new information is gained with feedback mechanisms. Because the BVF is defined as a function of both sensor and node data, it may also be time-varying. For example, if a user desires a collect on a particular date, then the value to that user diminishes with every passing day after the desired date. This time-dependent benefit can be represented by the example shown in Figure 4.6. Generally, the BVF is defined as a function of $(\boldsymbol{Y}_i(t), \boldsymbol{X}(t),$ and $t)$ and represented by $BVF_i(\boldsymbol{Y}_i(\cdot), \boldsymbol{X}(\cdot), t)$.

The BVF for a given node can be represented in many different ways. It can be a priority-based constant value or a simple function of time. These elementary forms do not demonstrate the full capabilities of the overall planning construct, thus, a more complicated BVF is shown as an example.

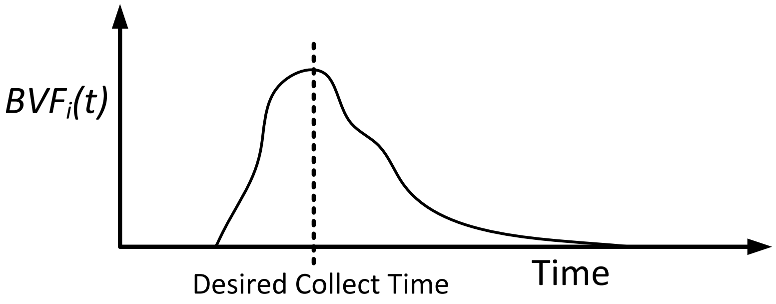

Figure 4.6: User Specified Time-dependent Benefit Value Function

The example function starts with the a simple priority-based BVF. A quality metric is then incorporated into the BVF. For space-based sensors, range is a simple measure of quality. The given distance between sensor and target equates to a certain spread of the sensor pixel across an area. A greater range means that the same number of pixels are collecting a larger area and therefore have a lower linear resolution per pixel. The range between target and sensor is a function of the sensor position, $\boldsymbol{X}(\bar{r}(t))$ and target position, $\boldsymbol{Y}_i(\bar{r}(t))$. This metric reduces the benefit when the range between target and sensor, $|\boldsymbol{X}(\bar{r}(t)) - \boldsymbol{Y}_i(\bar{r}(t))|$, is greater than the desired range. It also increases the benefit when the range is less than the desired range. In this way, range becomes a simple indicator of collection quality with the premise that the closer the target is to the sensor, the higher the quality of the image collected. The range from the sensor to an object varies over time as seen in Figure 4.7, although the shape may be slightly different for each target-sensor pair.

$$BVF_i\left(\boldsymbol{Y}_i(\cdot),\boldsymbol{X}(\cdot)\right) = RangeMult\left(\boldsymbol{Y}_i(\cdot),\boldsymbol{X}(\cdot)\right) * \boldsymbol{Y}_i(Priority) * \begin{cases} 1 & \text{if } \boldsymbol{Y}_i(Type) = \boldsymbol{X}(Type) \\ 0 & \text{if } \boldsymbol{Y}_i(Type) \neq \boldsymbol{X}(Type) \end{cases} \tag{4.22}$$

where

$$RangeMult(\boldsymbol{Y}_i(\cdot),\boldsymbol{X}(\cdot)) = \frac{\boldsymbol{Y}_i(DesiredCollectRange)}{|\boldsymbol{X}(\bar{r}(t)) - \boldsymbol{Y}_i(\bar{r}(t))|} \tag{4.23}$$

This single example of a BVF was intended to show the time-dependency and scope of possible functions. Ultimately, the definition of the BVF is critical to the solution and must be carefully defined based on the specific scenario and desired results.

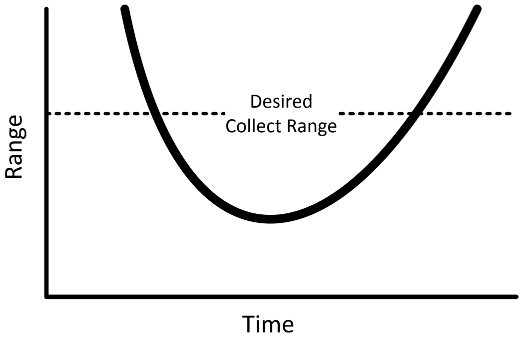

Figure 4.7: Range from Sensor to Target as a Function of Time

4.5.4 Node Servicing

In order to collect a node, it must be serviced [78]. This means that there is a finite amount of time that the sensor must spend at the node in order to collect the required information. From a space imaging perspective, servicing represents the time needed to collect the photons that will eventually equate to an image of the target. For other applications, it may represent the time needed to properly identify a target or search a given area [102]. In any case, it is represents time, specifically the time required to stay at a node. This servicing time is a function of both the node and a particular sensor (e.g., one sensor may be able to collect the same data in less time than another sensor). There is no requirement for every node to be defined identically. A particular node's servicing time may be based on its specific characteristics in conjunction with the sensors collecting it.

Normally, the variable t is used to denote time with subscripts or superscripts to identify particular times. However, in this case, the servicing time is a fixed time within the problem. In other words, it is data and not a variable. Thus, it will be expressed with a capital T to emphasize its nature as data, while the lower case t will be used to indicate variables of time. Generally, the servicing time of node i is represented by $T_i^S(\boldsymbol{Y}_i(t),\boldsymbol{X}(t))$.

The amount of time it takes to service a node represents the amount of time it takes a particular sensor to collect the data required for that target. It is based on node characteristics such as target size, as well as sensor performance characteristics such as how quickly a sensor can scan or collect a target of particular size.

There are many different ways to specify the servicing time based on the planning scenario and individual elements of $\boldsymbol{X}$ and $\boldsymbol{Y}$. One simple example of servicing time for node i can be defined by

$$T_i^S\left(\boldsymbol{Y}_i(t),\boldsymbol{X}(t)\right)=\frac{\boldsymbol{Y}_i(TgtSize)}{\boldsymbol{X}(CollectSpd)}*CollectSize\left(\boldsymbol{Y}_i(t),\boldsymbol{X}(t)\right) \tag{4.24}$$

where *CollectSize* is meant to demonstrate the unique nature of space-based imaging.

$$CollectSize\left(\boldsymbol{Y}_i(t),\boldsymbol{X}(t)\right)=\frac{|\boldsymbol{X}(\bar{r}(t))-\boldsymbol{Y}_i(\bar{r}(t))|}{\min\left[\,|\boldsymbol{X}(\bar{r}(t))-\boldsymbol{Y}_i(\bar{r}(t))| \quad \forall t\,\right]} \tag{4.25}$$

The look angle of a sensor and range to a target change the size of the sensor's footprint on the Earth thereby changing the amount of data being collected in one image or scan. *CollectSize* represents this changing parameter and is dependent on the relative range or distance between target and sensor. See illustration in Figure 4.8. The numerator of *CollectSize* is the scalar range between the sensor and target (i.e., the norm of the relative distance vector). In some cases, the denominator, $min\left[\,|\boldsymbol{X}(\bar{r}(t))-\boldsymbol{Y}_i(\bar{r}(t))| \quad \forall t\right]$, can be calculated *a priori*. This simple example assumes a satellite will have a minimum range at its closet point of approach to the target as shown in Figure 4.7.

4.5.5 Time Windows

Since the very nature of space image collection planning is time dependent, it follows that the ability to collect certain targets by a sensor is also dependent on time. This is seen most easily by observing that a satellite in orbit cannot see every point on the Earth at the same time. A satellite on the opposite side of the Earth cannot collect the target since it is blocked by the Earth itself. Thus, there is a window of time when the target is in view of the sensor and capable of being collected. This time window may be even more constrained because a target may have specific collection requirements that would further limit the availability (e.g., time of day or min/max angle). Therefore, each target-sensor pair must have certain time windows when the sensor is capable and allowed to collect a certain target. This may not be the case for every planning problem, but it does represent one of the most difficult scenarios for a collection planner. Each time window can be represented by an earliest and latest time that a sensor can collect a particular target [78, 104].

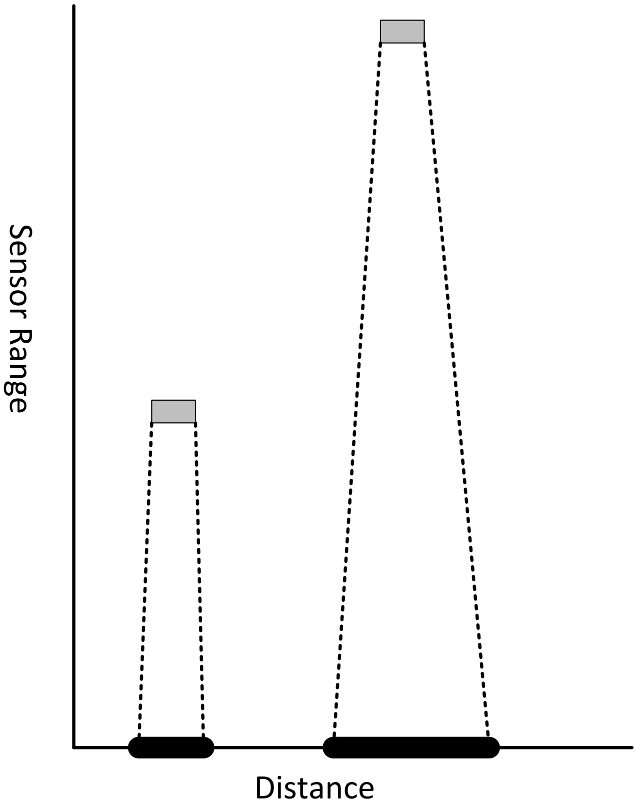

Figure 4.8: Satellite Footprint as a Function of Range

Time windows should also constrain a collection plan to ensure that the servicing of a node, with the duration T_i^S, must occur inside the time window. Because the windows are target specific, they must be indexed using i for the particular node. The specific mathematical formulation of the time windows will vary, but in general can be represented as an early time, $T_i^E\left(\boldsymbol{Y}_i(\cdot),\boldsymbol{X}(\cdot)\right)$, and a late time, $T_i^L\left(\boldsymbol{Y}_i(\cdot),\boldsymbol{X}(\cdot)\right)$. Note that there is nothing in the general formulation that precludes multiple time windows where T_i^E and T_I^L become vectors of times vice a pair of scalars.

The early and late window times represent a specific time, in time units, for the beginning and ending of a particular collection availability period between node *i* and the sensor. Because they are time data elements and not time decision variables, they employ the capital *T* nomenclature.

A simple example of a time window is a due date by a customer. In this case, the time window has a T_i^E and T_i^L which are constant but based solely on calendar time. This example is too simple for a space-based platform, but serves to illustrate the potential direct dependence on time.

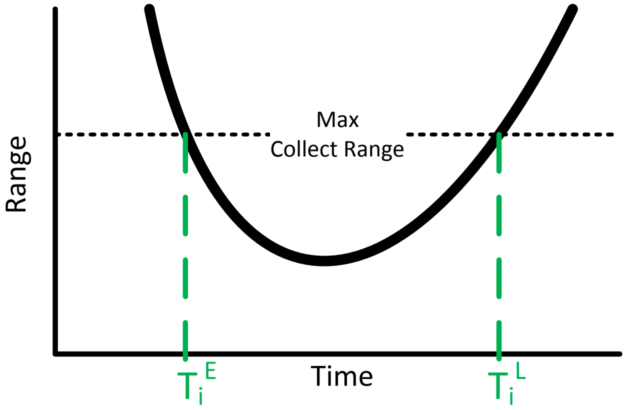

Figure 4.9: Example Time Window Defined as a Function of Range

As another example, let each target have at most one time window per planning period during which its collection by a particular sensor is allowed. In this case, the time windows are dependent on the range between the target and the sensor (which changes with time), but not explicitly on time (see Figure 4.9).

The early window time is specified as the earliest (minimum) time that a sensor can collect node *i* because the range from the sensor to the target is less than the maximum allowable collect range for that node.

$$T_i^E\,(\boldsymbol{Y}_i(\cdot),\boldsymbol{X}(\cdot)) = \min_t\ [\ |\boldsymbol{X}(\bar{r}(t)) - \boldsymbol{Y}_i(\bar{r}(t))| \leq \boldsymbol{Y}_i(MaxCollectRange) \quad \forall t\ ] \tag{4.26}$$

The late window time is specified as the latest (maximum) time that the sensor can collect node i because it is still within the maximum range constraint.

$$T_i^L(\boldsymbol{Y}_i(\cdot),\boldsymbol{X}(t\cdot)) = \max_t \;[\; |\boldsymbol{X}(\bar{r}(t)) - \boldsymbol{Y}_i(\bar{r}(t))| \leq \boldsymbol{Y}_i(MaxCollectRange) \quad \forall t \;] \tag{4.27}$$

By definition, a relationship exists between the early and late times such that $T^E \leq T^L$. This relationship holds even with multiple windows per planning period, though only for the specific pair that covers a single window and not across different windows. These examples assume an overhead sensor (i.e., the inertial radius of the sensor is always greater than the target's inertial radius, as measured for the center of the earth).

4.5.6 Decision Variables in Time

The space imaging application, like many other applications [102], uses time as a commodity to measure both travel between nodes and the functions occurring at a node. Therefore, the time associated with specific collection events is critical to executing a given plan.

Slew Time Between Nodes

For every arc $(i, j) \in A$, let δt_{ij} be defined as the time it takes to travel from node i to node j. This value is a non-negative real number. For an operational space imaging application, this transit time cannot be known in advance since the time to slew is fundamentally based on the attitude, rate, and acceleration associated with the departing node as well as those associated with the arriving node. Not only is δt_{ij} dependent on the time of departure and arrival, but it is significantly affected by the beginning and ending rates as well (as demonstrated in Chapter 3.6 and derived in Chapter 2).

Section 3.6 described the formulation and setup for an optimal control maneuvering problem, thus, δt_{ij} can be written as a function of the arguments from the optimal control solution with control, $\boldsymbol{u}(t)$.

$$\delta t_{ij} = \underset{\boldsymbol{u}(t)}{\operatorname{argmin}} \;\; J_{slew}\left[\boldsymbol{X}(\cdot),\boldsymbol{Y}_i(\cdot),\boldsymbol{Y}_j(\cdot),\boldsymbol{u}(t),t_0,t_f\right] \tag{4.28}$$

Specifically, $\delta t_{ij} = t_f - t_0$, where t_f and t_0 are the initial and final times from the maneuver optimization solution. One of the benefits of using the optimal control framework is that it allows for tremendous flexibility in calculating δt_{ij}. The planner is free to choose the level of model fidelity and cost function, J_{slew}, that results in the overall performance that best meets the stated requirements. This dissertation used a minimum time cost function in order to design STMs in chapter 3, but this formulation allows any conceivable cost or objective function in designing the individual maneuvers. Thus, the STM can be tailored to the operational constraints of interest to the individual planning scenario.

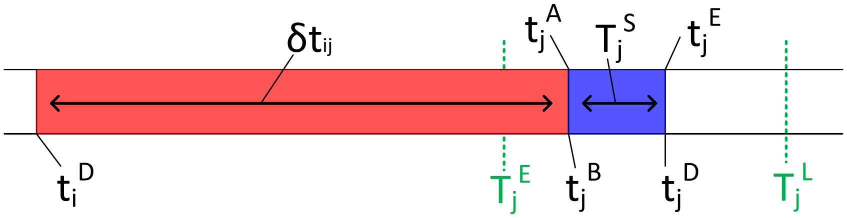

Figure 4.10: Example of a Simple Timeline

Event Timing Variables

Figure 4.10 illustrates four distinct events that need a time stamp during a collection plan, with the time spent in transit between nodes shown in red and the time spent collecting a target in blue. These relationships must be established and maintained for every node so each time stamp is indexed by node. These timestamps are the beginning of a collect at node j (t_j^B), the end of a collect (t_j^E), the specific time of departure from a node (t_j^D), and time of arrival at a given node (t_j^A). These four times are not completely independent and disregarding any waiting time, they are related as follows:

$$\begin{aligned} t_j^E &= t_j^B + T_j^S\left(\boldsymbol{Y}_j(\cdot), \boldsymbol{X}(\cdot)\right) \\ t_j^D &= t_j^E \\ t_j^A &= t_i^D + \delta t_{ij} \\ t_j^B &= t_j^A \end{aligned} \tag{4.29}$$

Note the subscripts i and j are used to denote sequencing with the assumption the arc *(i, j)* was used. Recall that T_j^S is the servicing time for a given node and represents the time required to collect a node. Relating to (4.28) in the optimal control solution to the individual maneuver, $t_i^D := t_0$ and $t_j^A := t_f$.

However, the most general planning framework should allow a sensor to wait and not be forced into constant motion if the overall benefit does not warrant it. A sensor would not wait during a collect, so waiting between t_j^B and t_j^E is not feasible. Waiting before a collect [78] or after a collect would be reasonable and should be allowed as options. Ultimately, the four distinct opportunities for waiting can be captured in two particular waiting periods, because of the relationships in (4.29) and are shown in Figure 4.11. The second equation in (4.29) means that waiting before the depart time or after completing a collect is the same period of time. Similarly, the fourth equation in (4.29) means that waiting before beginning a collect or after arriving at a node is equivalent. Rather than create an additional variable, we simply allow waiting by transforming the equalities into inequalities. Particularly,

$$\begin{aligned} t_j^D &\geq t_j^E \\ t_j^B &\geq t_j^A \end{aligned} \tag{4.30}$$

In other words, the departure time must be greater (later) than or equal to the end of the collect time. This is intuitive, since the sensor cannot depart before it has finished collecting, but is free to depart any time after finishing its collect. Similarly, the begin collect time must be later (greater) than or equal to the arrival time. Again, intuition confirms that a sensor cannot begin collecting before it has actually arrived at the node, but is free to start collecting at any time after it has arrived. Combining (4.29) and (4.30), the relationships can now be written to include waiting.

$$t_j^D \geq t_j^B + T_j^S\left(\boldsymbol{Y}_j(\cdot), \boldsymbol{X}(\cdot)\right) \quad \forall j \quad \in N_{tgt} \tag{4.31}$$

$$t_j^B \geq t_i^D + \delta t_{ij} \qquad \forall i, j \in N_{tgt} \tag{4.32}$$

Additionally, these time decision variables must also account for any limitations or restrictions placed on the plan by the time windows $\left[\ T_j^E(\cdot)\ ,\ T_j^L(\cdot)\ \right]$.

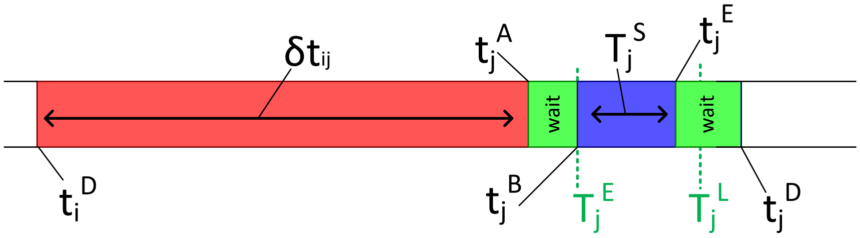

Figure 4.11: Example of a Timeline with Waiting

This results in two additional constraints on the time decision variables.

$$t_j^B \geq T_j^E \left(\boldsymbol{Y}_j(\cdot), \boldsymbol{X}(\cdot)\right) \quad \forall j \in N_{tgt} \tag{4.33}$$

$$t_j^B + T_j^S \left(\boldsymbol{Y}_j(\cdot), \boldsymbol{X}(\cdot)\right) \leq T_j^L \left(\boldsymbol{Y}_j(\cdot), \boldsymbol{X}(\cdot)\right) \quad \forall j \in N_{tgt} \tag{4.34}$$

where (4.33) prevents a collect from starting before the time window opens up and (4.34) prevents a collect after the time window has closed. The collect (i.e., node servicing) must be completed within the allowable time window for that node.

One final constraint is placed on the time variables is that they cannot be negative. Time must always have a positive real value and so must t_j^B and t_j^D. Because these constraints enforce a constantly increasing value in time as the sequence of targets progresses, they effectively eliminate internal subtours (i.e., loops that do not include the start and stop nodes).

4.5.7 Time Variable Constraints

Equations (4.31)-(4.34) articulate the constraints on a particular node's time decision variables. However, not all nodes are visited and therefore not all time decision variables need to be constrained. These time decision variable constraints are now written to apply for all visited nodes by invoking the filter of Δ_{ij}.

The most straightforward of the time constraints are the ones associated with the time windows. A node's time window is only an active constraint if the node is actually visited. Otherwise, the time window is irrelevant. Consequently, the begin collect time at node i

is only restricted when $\sum_j \Delta_{ji} = 1$. If the node is not visited, then $\sum_j \Delta_{ji} = 0$ and t_i^B is undefined and can take on any non-negative value. Additionally, by using Δ_{ij} as a switch, the constraints can now encompass the start and stop nodes, using the set N.

$$t_i^B \geq \sum_{j \in N} \Delta_{ji} \ T_i^E \left(\boldsymbol{Y}_i(\cdot), \boldsymbol{X}(\cdot)\right) \quad \forall i \in N \tag{4.35}$$

Any collection effort must be started and completed within the allowable access time window for a particular node. Therefore, rearranging terms from (4.34) and applying the requirement that the node must be visited yields

$$t_i^B \leq \sum_{j \in N} \Delta_{ji} \ \left(T_i^L \left(\boldsymbol{Y}_i(\cdot), \boldsymbol{X}(\cdot)\right) - T_i^S \left(\boldsymbol{Y}_i(\cdot), \boldsymbol{X}(\cdot)\right) \right) \quad \forall i \in N \tag{4.36}$$

When node i is not visited, then (4.35) and (4.36) together become a hard constraint [94] on t_i^B, forcing it to zero since $\sum_j \Delta_{ji} = 0$.

Similarly, the node departure time, t_i^D is only constrained if a node is visited, otherwise it can take on any non-negative value. Hence, (4.31) becomes

$$t_i^D \geq \sum_{j \in N} \Delta_{ji} \left[t_i^B + T_i^S \left(\boldsymbol{Y}_i(\cdot), \boldsymbol{X}(\cdot)\right) \right] \quad \forall i \in N \tag{4.37}$$

The fourth time decision variable constraint, (4.32), involves both the collection begin time and node departure time plus the slew time for the associated arc between nodes. It can be rearranged and written as a constraint on t_i^D rather than t_j^B.

$$t_i^D \leq t_j^B - \delta t_{ij} \quad \forall i, j \in N$$

The slew time, δt_{ij}, connecting nodes i and j, is dependent on whether or not the particular arc (i, j) was used to get to node j. If the arc (i, j) was not used, the slew time δt_{ij} has no effect on t_j^B or t_i^D. Applying the discriminator Δ_{ij}, which represents whether or not arc (i, j) was traveled, yields

$$t_i^D \leq \left(t_j^B - \delta t_{ij} \Delta_{ij} \right) \quad \forall i, j \in N \tag{4.38}$$

Thus, the node departure time, t_i^D, is required to be early enough to transit for δt_{ij} time along arc (i, j) and start collecting at t_j^B, given the previously defined constraints on t_j^B. This form of the constraint intuitively presents itself as an upper bound on t_i^D complementing the lower bound of (4.37). If node i is not visited, then $\Delta_{ij} = 0$ for all other nodes, $j \in N$, driving both the upper and lower bounds on t_i^D to zero.

Although it is a simplification that is not necessarily desired, it must be mentioned that without waiting, (4.37) - (4.38) become equalities instead of inequalities. In fact, there would be no need for t_i^D at all and (4.37) - (4.38) collapse to a single constraint on t_j^B.

$$t_j^B = \left(t_i^B + T_i^S(\boldsymbol{Y}_i(\cdot), \boldsymbol{X}(\cdot)) + \delta t_{ij}\right) \Delta_{ij} \quad \forall i, j \in N$$

As previously discussed, it is essential that all time variables be constrained to non-negative values. Consequently, the following constraints must be included in any formulation:

$$\begin{aligned} \Delta_{ij} &\in \{0,1\} \quad \forall i, j \in N \\ t_i^B &\geq 0 \quad \forall i \quad \in N \\ t_i^D &\geq 0 \quad \forall i \quad \in N \\ \delta t_{ij} &\geq 0 \quad \forall i \quad \in N \end{aligned} \tag{4.39}$$

4.5.8 Objective Function

The overall objective of the time-varying graph problem remains the same as the static problem (i.e., maximize overall plan benefit). However, the value for each node is no longer identical and fixed. Instead, each node's value is unique and free to change over time. The benefit gained from a single visit to j is defined by $BVF_j\left(\boldsymbol{Y}_j(\cdot), \boldsymbol{X}(\cdot), t_j^B\right)$. The benefit gained by the entire collection plan becomes the sum of the individual BVFs over all target nodes visited with the specific time for collecting a node (t_j^B) being dependent on the control history ($\boldsymbol{u}_{ij}(t)$). The objective for the planner becomes

$$\max_{\Delta_{ij}, \boldsymbol{u}_{ij}(t)} \quad \sum_{j \in N} \sum_{i \in N} \Delta_{ij} \; BVF_j\left(\boldsymbol{Y}_j(\cdot), \boldsymbol{X}(\cdot), t_j^B\right) \tag{4.40}$$

4.5.9 Start and Stop Nodes

The start/stop nodes must remain transparent to the planner. The collection plan generated will include these start/stop nodes, but they are removed before handing the plan over to a particular platform to be executed. The implication is that the sensor platform must define its own maneuver to the first target in order to arrive on the collect node at its begin time for collection, t_i^B. The platform must determine when and where to maneuver after the departure time, t_i^D, from the final collect node. This allows the platform to choose how to enter or exit an assigned collection plan. It can also be thought of as placing the pre-collection and post-collection maneuvers outside the scope of the collection planner.

In addition to zero benefit, $BVF_0 = 0.0$, the transparency of start node 0 requires that it can have no impact with servicing time ($T_0^S = 0$), because it will never be collected as a target [78]. The early and late window times must be included, but since they are not active constraints, they can be set at infinite extremes, $[T_0^E, T_0^L] = [0.0, +\infty)$. If the start node is not allowed to affect the planning decisions, there can be no slew time required from the start node to every target node, thus, $\delta t_{0j} = 0.0 \;\; \forall j \in N$. This constraint includes the arc proceeding from the start node directly to the stop node and ensures that there exists at least one feasible path through the entire set of targets, even if it yields no overall benefit and has no travel time.

Similar to the start node, the stop node f must remain transparent. It must have no benefit, $BVF_f = 0.0$, or impact to servicing time ($T_f^S = 0$). The early and late times are set identically to the start node. Because there are no feasible arcs leading out of the stop node, there is no need to constrain δt_{fj}. However, every arc leading into the stop node must be set to zero transit time, $\delta t_{if} = 0.0 \;\; \forall i \in N$. The start and stop node data are summarized in Table 4.2.

4.5.10 Special Situations

This section seeks to address scenarios that are outside the traditional point-target space imaging application used to motivate the previous planning formulation.

Start Node, 0	Stop Node, f
$\boldsymbol{Y}_0 = []$	$\boldsymbol{Y}_f = []$
$BVF_0 = 0$	$BVF_f = 0$
$T_0^S = 0$	$T_f^S = 0$
$[T_0^E, T_0^L] = [0.0, +\infty)$	$[T_f^E, T_f^L] = [0.0, +\infty)$
$\sum_{j \in N} \Delta_{0j} = 1$	$\sum_{i \in N} \Delta_{if} = 1$
$\Delta_{i0} = 0 \;\; \forall i \in N$	$\Delta_{fj} = 0 \;\; \forall j \in N$
$\delta t_{0j} = 0.0 \;\; \forall j \in N$	$\delta t_{if} = 0.0 \;\; \forall i \in N$

Table 4.2: Start/Stop Node Specifications and Constraints

Multiple Collects of a Single Target

There may be a scenario when a planner desires to collect a particular target more than once. This is especially true if the collects use different sensors. The inherent relationship of the node-sensor pair naturally forces the planner to create a unique node for each sensor type. For example, if a planner wanted a RADAR collect and an EO collect of the same Earth-based location, two target nodes would be created. Each node would be specific to the target and the sensor collecting it.

When multiple collects are desired from the same sensor or type of sensor, the planner can create a distinct node for each instance of desired collection with the appropriate node data in $\boldsymbol{Y}_i(t)$. Care should be taken to distinguish the nodes from themselves. This can be done in a variety of ways, but the easiest is through different time windows for each node. For example, if three collects were desired of a particular target, each collect can be specified with non-overlapping time windows, prior to the planning effort. Thus, the planner is able to potentially gain three different collects on the same target.

Stereo Imaging

Stereo imaging is a special kind of image collection that takes advantage of the space-based sensor's movement to create a pair of images that are later synthesized into a single product. The idea is illustrated in Figure 4.12. For instance, the IKONOS commercial imaging satellite describes it as "each stereo pair contains an image collected at a low elevation angle (above 60 degrees) as well as an image collected at a higher elevation angle (above 72 degrees)" [105]. These stereo image products have been used for 3-D mapping and creating digital terrain models that are used in exploration, mining, transportation, and environmental mapping.

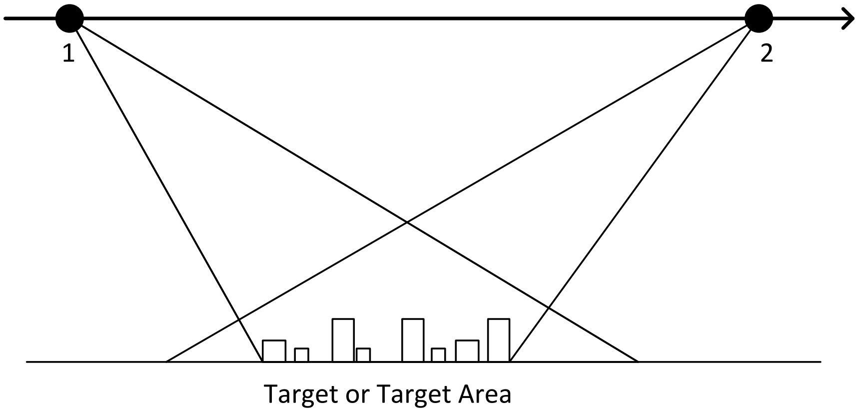

Figure 4.12: Stereo Imaging Illustration

In order to include the ability to plan for a stereo collect, the planner has to create a target node for each individual image with specific constraints on the node that specify the desired angle or range of angles for the sensor to capture the appropriate image. The collect can even be constrained to a single sensor on a single pass, depending on how the planner wishes to specify $\boldsymbol{Y}_i(t)$.

BVF_i has, thus far, been defined for a single node as a function of $\left(\boldsymbol{Y}_i(\cdot), \boldsymbol{X}(\cdot), t_i^B\right)$. The stereo collect is an example of when a planner might want a target's benefit to be dependent on additional variables, such as another target's collection or another sensor. If the only purpose of the collect is a stereo image, there is no benefit for collecting one node without the other. In this case, the BVF of one node is dependent on a second node [106]. Therefore, the formulation of the general node benefit is expanded to include multiple nodes

$$BVF_i\left(\boldsymbol{Y}_i(\cdot), \boldsymbol{Y}_j(\cdot), \boldsymbol{X}(\cdot), \boldsymbol{t}^B\right) \tag{4.41}$$

where $\boldsymbol{t}^B$ is the vector of t_i^B values for every $i \in N$. The subscripts of BVF_i remain the same because the benefit is still attributable to a particular node-sensor pair. This expanded formulation allows the introduction of as many additional target nodes as desired to fully define the benefit of this particular node's collect, though only two are shown above.

Specifically for a stereo collect, let the index of the two stereo nodes be represented by p and q, then the node benefit may be defined as

$$BVF_p = \boldsymbol{Y}_p(Priority) * \frac{1}{2} \begin{cases} StereoBenefit & \text{if } \sum_i \Delta_{ip} + \sum_i \Delta_{iq} = 2 \\ 0 & \text{if } \sum_i \Delta_{ip} + \sum_i \Delta_{iq} < 2 \end{cases} \tag{4.42}$$

where $StereoBenefit$ is a predetermined benefit for collecting the stereo image. The BVF for the other stereo node can be written in an identical manner, since they share equally in the overall benefit of the stereo collect. The benefit is gained only if the sensor collects both nodes and no benefit is gained when only one node is collected. Flexibility remains in the definition of the BVF to allow a positive benefit for a single collect only, with an increased benefit for the stereo collect.

Scan Based Targets

Unlike a point target, a scan collect requires the sensor to hit a specific begin-scan node and then proceed in a specific manner to an end-scan node before being allowed to depart. See Figure 4.13 for an illustration.

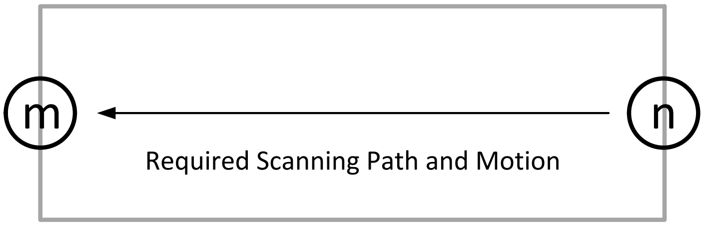

Figure 4.13: Example Scan Node Pair

Let a single scan be defined by a pair of nodes, the begin-scan and end-scan nodes, which are indexed by n and m, respectively. If the start-scan node n is visited, the sensor must to travel along the single feasible arc directly to the end-scan node m. All other arcs are declared infeasible by

$$\Delta_{nj} = 0 \quad \forall j \in \{N_{tgt}, N_f, j \neq m\} \tag{4.43}$$

$$\Delta_{im} = 0 \quad \forall i \in \{N_0, N_{tgt}, i \neq n\} \tag{4.44}$$

The benefit for collecting the scan, $ScanBenefit$, is allocated to the end-scan node, meaning the entire scan must be completed before any benefit is accrued.

$$BVF_n = 0 \quad \text{and} \quad BVF_m = ScanBenefit \tag{4.45}$$

The early and late window times for each node are defined normally per the node and sensor. Waiting is allowed before starting the collect at node n or after node m is serviced, but not in between the scan nodes. The required motion and fixed time between nodes are defined by the scan parameters. This restriction on waiting changes two of the time variable constraints, (4.37) and (4.38) (though in the same form as (4.32)), into equalities. Specifically, the depart time of the begin-scan node, t_n^D, and the begin time of the end-scan node, t_m^B, for each scan pair must be constrained by

$$t_n^D = \sum_{j \in N} \Delta_{jn} \left[t_n^B + T_n^S(\boldsymbol{Y}_n(\cdot), \boldsymbol{X}(\cdot)) \right] \tag{4.46}$$

$$t_m^B = t_n^D + \delta t_{nm} \tag{4.47}$$

The constraints on t_n^B and t_m^D remain inequalities as previously defined in (4.37)- (4.38).

The time spent scanning by the sensor, $ScanTime$, is allocated to the single arc as transit time connecting n and m.

$$\delta t_{nm} = ScanTime \tag{4.48}$$

Because the time required to collect the scan is included as the transit time between scan nodes, the servicing time for the begin-scan node is simply the reconfiguration time required before a scan is collected. This can be zero, or a non-zero value representing any required setup or settling time before collecting the scan by a given sensor. The same opportunity exists to specify a reconfiguration time for the end-scan node before it departs the node. This reconfiguration time period is not explicitly called out in the formulations of sections 4.2.1 since it is normally included in the node servicing time, T_i^S.

$$T_n^S = \text{begin-scan reconfiguration time} \tag{4.49}$$

$$T_m^S = \text{end-scan reconfiguration time} \tag{4.50}$$

4.6 Formulation of Time-Varying Planning Problem, $P1$

The time-varying operational collection planning problem, $P1$, can now be formulated with constraints as finding the target sequence, Δ_{ij} and control history for the sensor, $\boldsymbol{u}(t)$, that maximizes the objective function subject to a set of constraints.

$$\max_{\Delta_{ij},\boldsymbol{u}_{ij}(t)} \quad \sum_{j\in N}\sum_{i\in N}\Delta_{ij}\, BVF_j\left(\boldsymbol{Y}_i(\cdot),\boldsymbol{Y}_j(\cdot),\boldsymbol{X}(\cdot),t_j^B\right) \tag{4.51}$$

subject to

$$\sum_{i\in N}\Delta_{ij} \le 1 \quad \forall j\in N \tag{4.52}$$

$$\Delta_{i0} = \Delta_{fi} = \Delta_{ii} = 0 \quad \forall i\in N \tag{4.53}$$

$$\sum_{j\in N}\Delta_{0j} = \sum_{i\in N}\Delta_{if} = 1 \tag{4.54}$$

$$\sum_{i\in N}\Delta_{ij} - \sum_{i\in N}\Delta_{ji} = 0 \quad \forall j\in N_{tgt} \tag{4.55}$$

$$t_i^B - \sum_{j\in N}\Delta_{ji}[T_i^L(\boldsymbol{Y}_i(\cdot),\boldsymbol{X}(\cdot)) - T_i^S(\boldsymbol{Y}_i(\cdot),\boldsymbol{X}(\cdot))] \le 0 \quad \forall i\in N \tag{4.56}$$

$$t_i^B - \sum_{j\in N}\Delta_{ji}T_i^E(\boldsymbol{Y}_i(\cdot),\boldsymbol{X}(\cdot)) \ge 0 \quad \forall i\in N \tag{4.57}$$

$$t_i^D - \left(t_j^B - \delta t_{ij}\Delta_{ij}\right) \le 0 \quad \forall i,j\in N \tag{4.58}$$

$$t_i^D - \sum_{j\in N}\Delta_{ji}\left(t_i^B + T_i^S(\boldsymbol{Y}_i(\cdot),\boldsymbol{X}(\cdot))\right) \ge 0 \quad \forall i\in N \tag{4.59}$$

$$t_i^A - t_i^B \le 0 \quad \forall i\in N \tag{4.60}$$

$$\delta t_{ij} = \underset{\boldsymbol{u}_{ij}(\cdot)}{\operatorname{argmin}} \; J_{slew}\left[\boldsymbol{X}(\cdot),\boldsymbol{Y}_i(\cdot),\boldsymbol{Y}_j(\cdot),\boldsymbol{u}_{ij}(\cdot),t_i^D,t_j^A\right] \quad := t_j^A - t_i^D \tag{4.61}$$

$$\delta t_{0j} = \delta t_{if} = 0.0 \quad \forall\{i,j\} \in N \tag{4.62}$$

$$\Delta_{ij} \in \{0,1\} \quad \forall\{i,j\} \in N \tag{4.63}$$

$$t_i^B \geq 0 \quad \forall i \in N \tag{4.64}$$

$$t_i^D \geq 0 \quad \forall i \in N \tag{4.65}$$

$$\delta t_{ij} \geq 0 \quad \forall i \in N \tag{4.66}$$

$$t_i^A \geq 0 \quad \forall i \in N \tag{4.67}$$

Equation (4.52) ensures that the single visit path constraint holds for the sensor. This means that the sensor is allowed to collect a given node's benefit only once. Equation (4.53) prevents the infeasible arcs and self-loops from being used. Equation (4.54) forces every sensor to begin and finish at the designated nodes and includes the ability to proceed from the start node directly to the stop node as a feasible path. Equation (4.55) ensures that if a sensor arrives to collect a node, it must also leave that node. Equations (4.56) - (4.57) constrain the begin collection times for each node. Equations (4.58) - (4.59) constrain the departure time for each node. Equation (4.60) is an additional constraint that ensures node arrival precedes its servicing. Together, (4.56) - (4.60) ensure time is increasing and eliminate subtours. Equation (4.61) defines the individual transit time between nodes as the argument of the optimal control problem, J_{slew} and its solution. Equation (4.62) fixes the transit time between start or stop node and every other node at zero. It also creates at least one feasible path through all the collect nodes, directly between start node 0 and stop node f with zero transit time. Equations (4.63)- (4.67) ensure all variables are non-negative.

4.7 Summary

This chapter introduced several elements of graph theory using the base problem, $P0$. In $P0$, the concepts of nodes, arcs, Δ_{ij}, and constraints were applied to a simple space-based image collection problem. Start and Stop nodes were presented and formulated such that they did not interfere with the collection plan solution but maintained flexibility for the planner in how to formulate the overall problem. Slew or transit time was defined as the arguments of an optimal control maneuvering problem.

An original planning problem, $P1$, was presented which expanded $P0$ to include operational factors that made the whole scenario time-varying. The node BVF was presented as critical to proper planning. Target availability was captured in time windows and time-based decision variables were defined for events including the ability for a sensor to wait before or after a collection period. Slew or transit time remained the arguments of an optimal control maneuvering problem. Special image collection cases were discussed including stereo imaging and scan-based collection. Finally, the formulation for this new time-varying space-based image collection problem was presented as a hybrid optimal control problem.

CHAPTER 5:
Illustration of Planning Elements

Chapter 3 demonstrated the improvements available to a satellite planner using optimal control for nine individual maneuvers, but this improved time is not the sum of the benefit. In fact, when the rapid maneuvering is used in a planning scenario, the entire plan can benefit from each improved maneuver. This chapter will combine the elements from Chapters 1 - 3 with the collection planning concepts from Chapter 4 to illustrate how everything can work together to enhance the capacity of an imaging system.

5.1 Case Study: Satellite Collection Planning Problem

A set of targets is given as 14 cities in the western states of the U.S., specified in Table 5.1 and shown in Figure 5.1. Customer and Operational requirements dictate the scan direction based on geometry and size of the target. Rather than attempting to define each target individually, a random scan direction with a constant scan speed of 4.2 km/s (approximately $0.5°/s$ at the sensor) was assigned to each collect node. The direction vectors of each scan are shown in Table 5.1

Tgt #	Target Name	Latitude	Longitude	Local Scan Direction
1	Boise, ID	43.61° N	116.20° W	27.9° N of E
2	Carson City, NV	39.16° N	119.77° W	55.5° S of W
3	Cheyenne, WY	41.14° N	104.82° W	88.0° N of W
4	Denver, CO	39.74° N	104.99° W	19.6° N of E
5	Helena, MT	45.59° N	112.04° W	75.3° S of E
6	Los Angeles, CA	34.05° N	118.25° W	22.4° S of E
7	Olympia, WA	47.04° N	122.90° W	75.1° N of E
8	Phoenix, AZ	33.45° N	112.07° W	45.9° S of W
9	Sacramento, CA	38.58° N	121.49° W	8.0° N of W
10	Salem, OR	44.94° N	123.04° W	31.6° S of W
11	Salt Lake City, UT	40.76° N	111.89° W	72.0° N of W
12	San Fransisco, CA	37.78° N	122.42° W	18.9° S of E
13	Santa Fe, NM	35.69° N	105.94° W	43.2° S of W
14	Seattle, WA	47.61° N	122.33° W	9.3° S of E

Table 5.1: Case Study Target Set

Figure 5.1: Case Study Set of Available Targets

Let a sequence of 10 collect nodes from the set of 14 targets be specified by target number as $[7,1,10,9,2,11,3,4,13,8]$ and shown in the OP in Figure 5.2. The corresponding Δ_{ij} values for this solution are given in Table 5.2.

The BVF of each target was defined to be a constant value. If the target was a state capital, its value was 10. Other cities were valued at 1. The scenario epoch, t_{epoch}, was set at 15 APR 2012 18:15:00 UTCG. The start node depart time of $t_{epoch} + 120$ seconds ($t_0^D = 120.0$) or 18:17:00 UTCG for all three maneuver types from Chapter 3 (ISM, STM, and γ ISM). Since the start node requires no transit time to the first node, due to its transparency, this time is also the start of the collection at the first collect node (t_7^B).

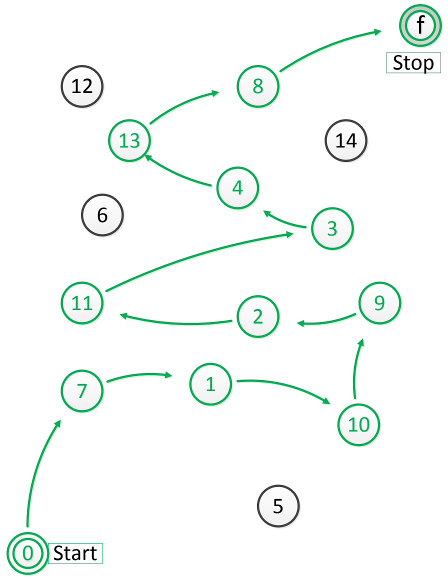

Figure 5.2: Orienteering Graph of Case Study Example Solution

Node	0	1	2	3	4	5	6	7	8	9	10	11	12	13	14	f
0	0	0	0	0	0	0	0	0	0	0	0	0	0	0	0	0
1	0	0	0	0	0	0	0	$\boxed{1}$	0	0	0	0	0	0	0	0
2	0	0	0	0	0	0	0	0	0	$\boxed{1}$	0	0	0	0	0	0
3	0	0	0	0	0	0	0	0	0	0	0	$\boxed{1}$	0	0	0	0
4	0	0	0	$\boxed{1}$	0	0	0	0	0	0	0	0	0	0	0	0
5	0	0	0	0	0	0	0	0	0	0	0	0	0	0	0	0
6	0	0	0	0	0	0	0	0	0	0	0	0	0	0	0	0
7	$\boxed{1}$	0	0	0	0	0	0	0	0	0	0	0	0	0	0	0
8	0	0	0	0	0	0	0	0	0	0	0	0	0	$\boxed{1}$	0	0
9	0	0	0	0	0	0	0	0	0	0	$\boxed{1}$	0	0	0	0	0
10	0	$\boxed{1}$	0	0	0	0	0	0	0	0	0	0	0	0	0	0
11	0	0	$\boxed{1}$	0	0	0	0	0	0	0	0	0	0	0	0	0
12	0	0	0	0	0	0	0	0	0	0	0	0	0	0	0	0
13	0	0	0	0	$\boxed{1}$	0	0	0	0	0	0	0	0	0	0	0
14	0	0	0	0	0	0	0	0	0	0	0	0	0	0	0	0
f	0	0	0	0	0	0	0	0	$\boxed{1}$	0	0	0	0	0	0	0

Table 5.2: Case Study Δ_{ij} Matrix

Each sensor type was allowed to proceed to the next node as soon as it was finished servicing the current node. Servicing time was set at 4.0 seconds for every node. Therefore, the sensor must remain on a target for the full $T_i^S = 4.0$ seconds in order to collect the benefit before it is allowed to proceed to the next target.

The time windows for each collect node were set to maximize the opportunity of collection. Specifically, every node was identically defined with $T_i^E = 120$ and $T_i^L = 360$ seconds past epoch.

The resource constraint was specified as a maximum collection time and set to four minutes ($T_{max} = 240.0$) or $t_{epoch} + 360$ seconds, ending at 18:21:00 UTCG. The platform and sensor specifics are detailed in Chapter 3.

The sensor COEs as well as the node coordinate data from Table 5.1 were converted to Cartesian coordinates for a particular time using algorithms from [37]. The attitude, body rates and accelerations for each individual slew maneuver were then generated using the targeting equations from Chapter 2 evaluated at the specific time of arrival or departure at the target.

5.2 ISM Based Maneuver Plan

The spherical limits used for the ISM in this case study were developed in section 3.3. Within the maximum time constraint, the ISM based maneuver plan was able to collect eight of the ten assigned targets. The overall benefit for the ISM plan was 80. In order to collect all ten targets, the maximum time would have to be increased at least 36 seconds to 276 seconds (an increase of more than 15 percent above the 240 second T_{max})

Figure 5.3 shows the quaternion trajectory for the ISM based collection of all 10 targets. The periods of target or node servicing are annotated by large circles. Note the time axis starts at 120 seconds and also that the servicing time of the last two collects are beyond the max time allowed (T_{max}) but included for completeness. The ISM plan was en-route to the ninth collect node (Santa Fe), but did not complete the collection before T_{max}. Therefore, no benefit was gained from the last two targets.

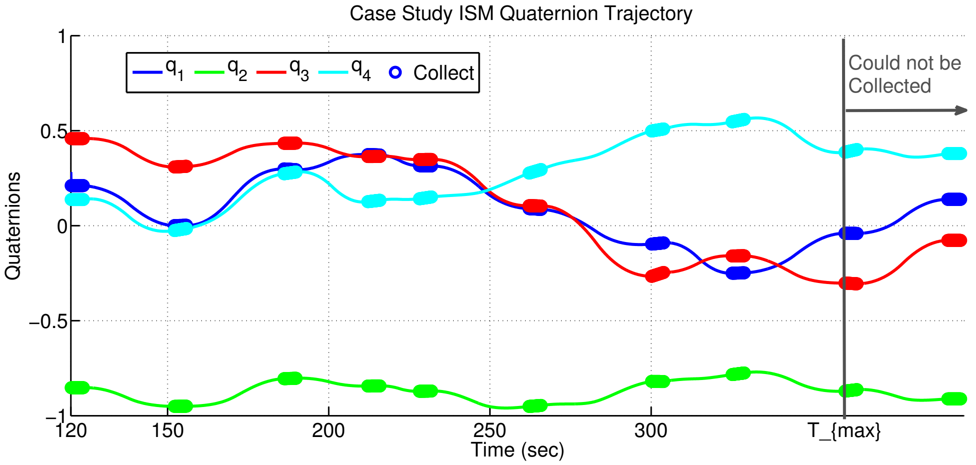

Figure 5.3: ISM Based Maneuver Plan: Quaternion Trajectories

Figure 5.4 shows the body rate trajectory for the ISM based collection of all 10 targets with the same servicing time annotations. The black dotted line is the overall rate magnitude.

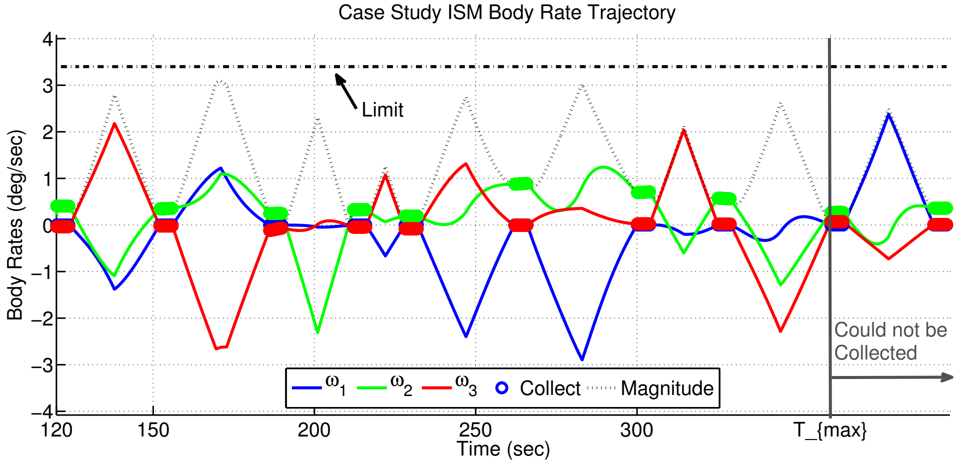

Figure 5.4: ISM Based Maneuver Plan: Rate Trajectories

Figure 5.5 shows the body acceleration trajectory for the ISM based collection of all 10 targets with the same servicing time annotations. The magnitude is shown as a black dotted line and remains at or near the limits shown as the black dash-dot line.

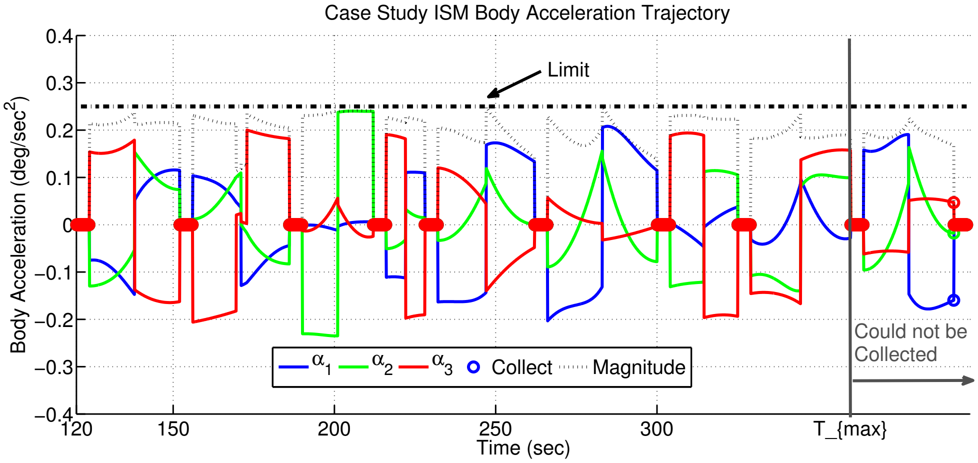

Figure 5.5: ISM Based Maneuver Plan: Acceleration Trajectories

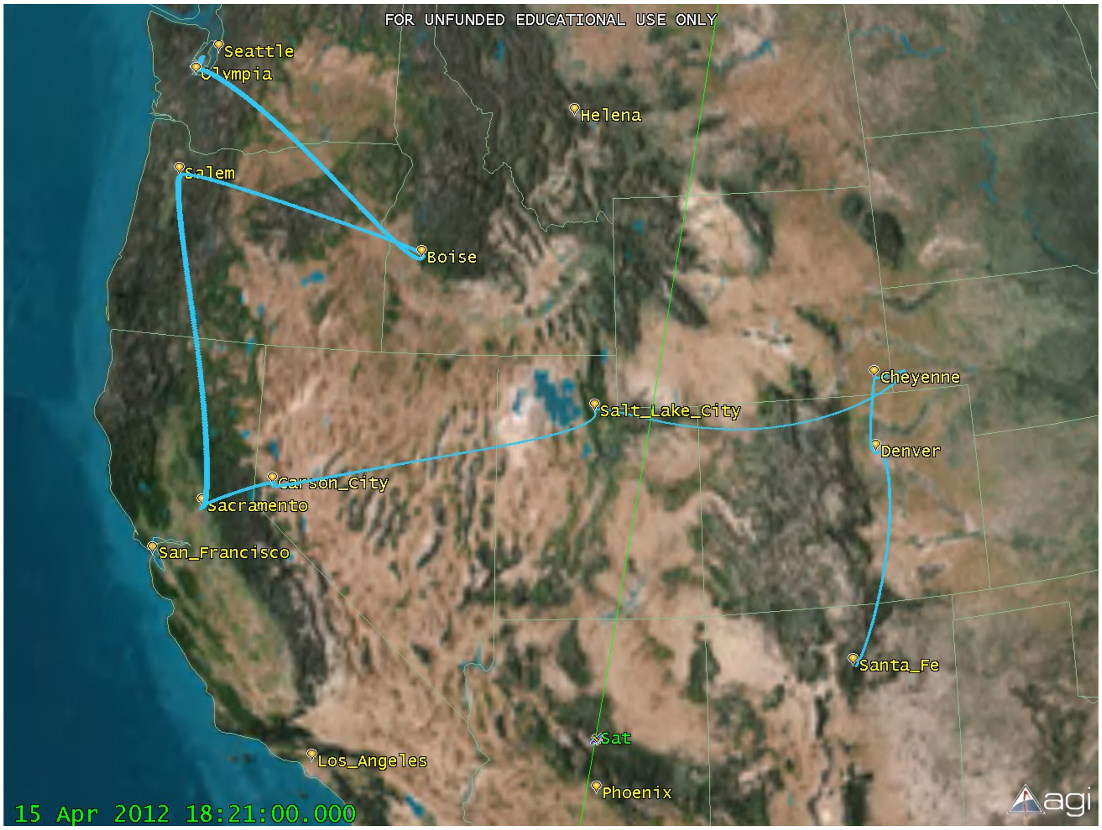

Figure 5.6: ISM Based Maneuver Plan Boresight Trace at T_{max}

Because quaternions are not intuitive, the boresight trace (in blue) of the sensor was plotted in Figure 5.6 as a better illustration of the sensor motion over the Earth. The figure was created using the Analytical Graphics, Inc. Systems Tool Kit (STK), provided through the Educational Alliance Partnership Program. The maneuver sequence was designed off-line and STK was used simply to display the results. In Figure 5.6, the satellite (sensor) orbital path over the ground is shown as a green line and the sensor attitude as a projection of the boresight proceeding from the sensor to the earth.

5.3 STM Based Maneuver Plan

In contrast to the ISM, the STM based maneuver plan collected all 10 assigned targets in 226 seconds. The overall benefit of the STM plan was 100. Figure 5.7 shows the quaternion trajectory for the STM based collection of all 10 targets with the servicing annotated by large circles.

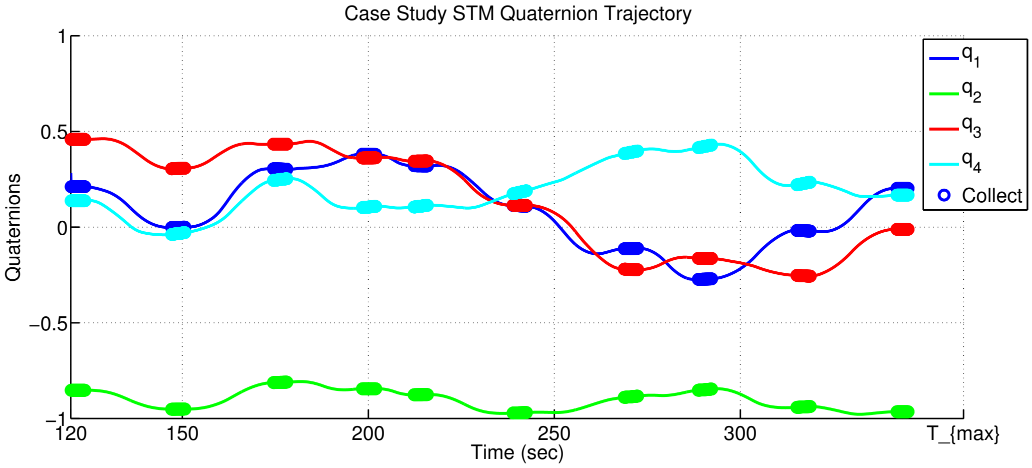

Figure 5.7: STM Based Maneuver Plan: Quaternion Trajectories

Figure 5.8 shows the body rate trajectory for the STM based collection of the targets with the same servicing time annotations. The black dotted line is a overall magnitude of the rates and rises above the ISM shperical limit (dash-dot line) on several maneuvers.

Figure 5.9 shows the body acceleration trajectory for the STM based collection of all 10 targets with the same servicing time annotations. The magnitude is shown as a black dotted line and remains at or near the limits shown as the black dash-dot ISM spherical acceleration maximum line. Note that the STM consistently uses more acceleration than the ISM spherical limit would have allowed for each maneuver. This increased acceleration allows the body rate to be greatly increased as compared to the ISM.

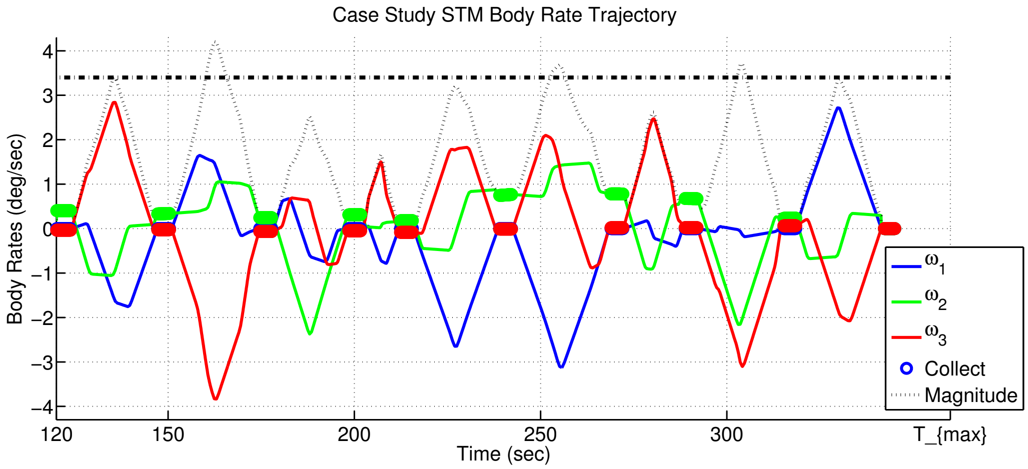

Figure 5.8: STM Based Maneuver Plan: Rate Trajectories

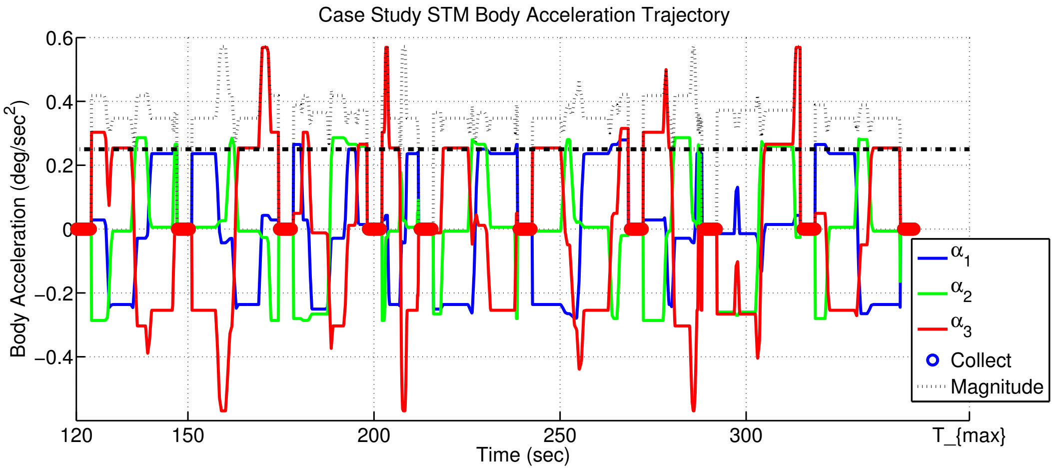

Figure 5.9: STM Based Maneuver Plan: Acceleration Trajectories

The boresight trace of the STM sensor (in yellow) is shown in Figure 5.10 and stopped at the completion of all 10 collects.

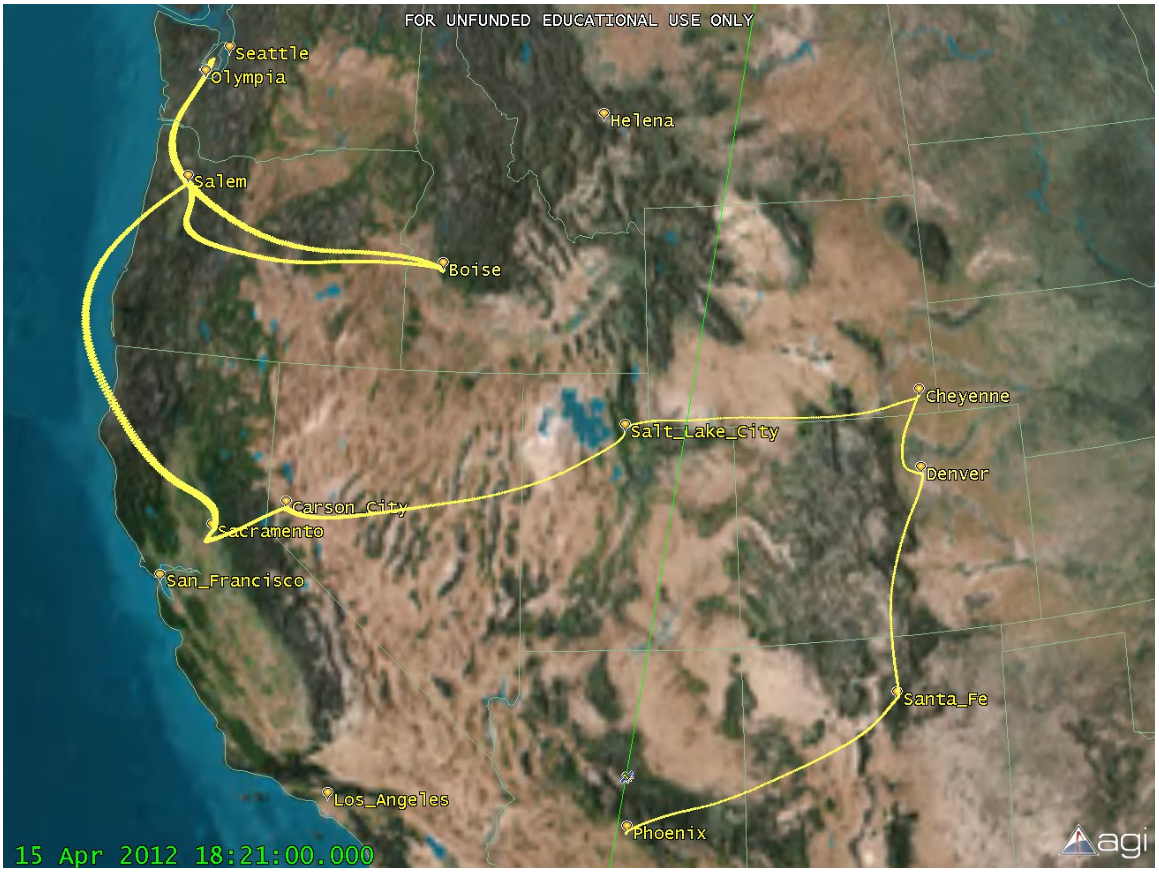

Figure 5.10: STM Based Maneuver Plan Boresight Trace at Completion of Collects

Most of the maneuvers presented were within the acceleration limited region, thus, acceleration is the limiting performance characteristic for the ISM. Conversely, the STM in limited by the capability of the reaction wheel system capability. These limits are direction dependent, as seen in the agilitoid (Figure 3.7), and the STM takes advantage of the full agiltoid in designing the time-optimal maneuver. Figure 5.11 shows the commanded RW torque for each of the four reaction wheels in the example system. Note that the reaction wheels are consistently at the maximum torque values, allowing the sensor to execute each maneuver in minimum time. While the accelerations in Figure 5.9 may look somewhat erratic, this is due to the time scale in the figure. Figure 5.11 demonstrates that the commanded torque profile is very benign. A more detailed look at the RW commanded torque is included in the subsequent examination of two particular maneuvers.

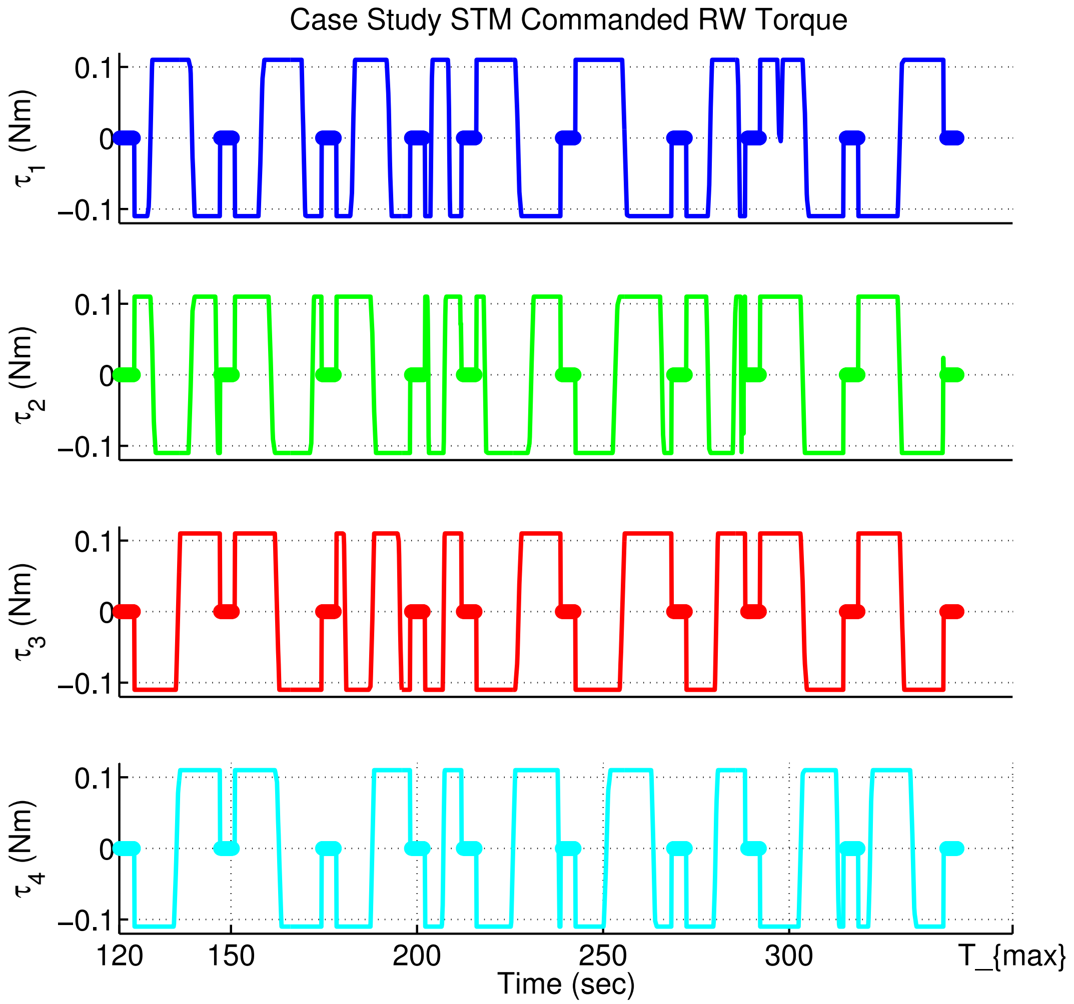

Figure 5.11: STM Reaction Wheel Torque Command Trajectory

5.4 Comparison between the ISM and STM Plans

The comparison between the ISM and STM plans starts with a comparison of the time to complete each maneuver. The results are shown in Figure 5.12(a) and listed in Table 5.3. The values in Table 5.3 that are boxed are shown for reference but because the node was visited after the time window had expired, the ISM sensor gained no benefit from these nodes. The time required by the ISM plan to collect all 10 targets 276 seconds compared to the STM plan completion in 226 seconds. Figure 5.12(b) compares the relative performance as a function of η.

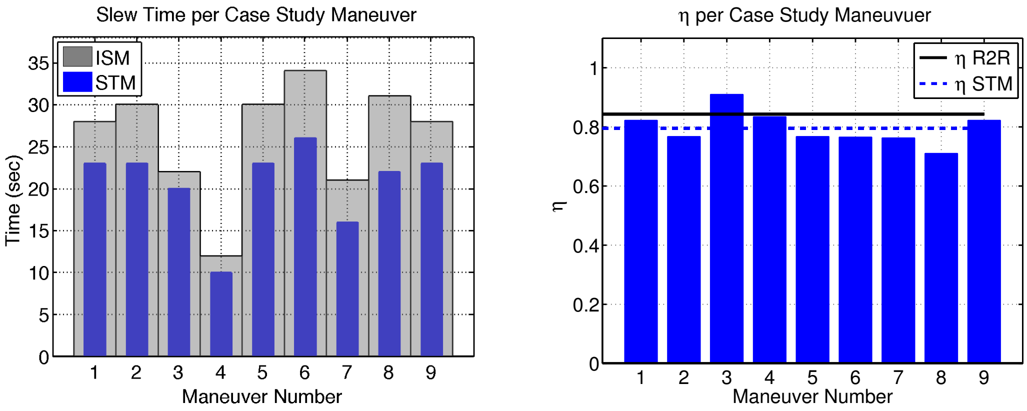

(a) (b)

Figure 5.12: Individual Maneuver Comparison Between ISM and STM in Time (a) and η (b)

	ISM		STM	
Node	t^B	t^D	t^B	t^D
1	152	156	147.1	151.1
2	228	232	212.2	216.2
3	300	304	268.8	272.8
4	325	329	288.7	292.7
5	0	0	0	0
6	0	0	0	0
7	120	124	120.0	124.0
8	$\boxed{392}$	$\boxed{396}$	342.1	346.1
9	212	216	198.4	202.4
10	189	190	174.4	178.4
11	262	266	238.9	242.9
12	0	0	0	0
13	$\boxed{360}$	$\boxed{364}$	315.1	319.1
14	0	0	0	0

Table 5.3: Node Collect Times in Seconds After t_{epoch} for ISMs and STMs

The solid black line in Figure 5.12(b) is the value of the R2R ISM η derived in section 3.5.3 ($\eta = 0.84$). The blue dashed line represent the value for η as the average of the nine STMs and its value is 0.79. The STM performance resulted in a decrease in the time spent slewing by 21 percent (186 seconds (STM) versus 236 seconds (ISM) slewing for all 10 targets). The time savings confirm the average η calculated in Figure 5.12(b). Any decrease in time between collections means that there is more time available for collecting nodes and producing revenue.

The magnitude of the respective rates are compared in Figure 5.13. The STM consistently uses a higher rate for each maneuver, and in some case achieves even higher rates than the ISM spherical rate limit would have allowed.

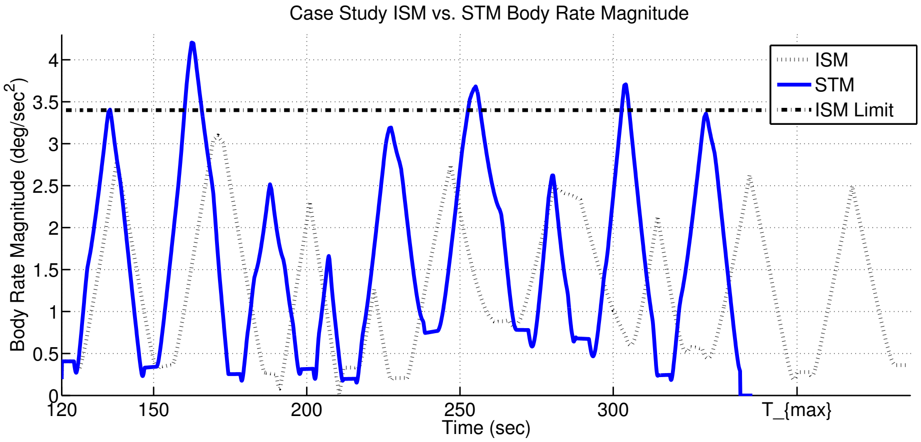

Figure 5.13: Body Rate Magnitude Comparison Between ISM and STM

A similar comparison of the acceleration magnitudes in Figure 5.14 yields the most significant difference between the ISM and STM plans. The acceleration magnitude of the ISMs must be within the spherical limit, by design, but the STMs maximize the available acceleration to achieve the higher performance. The red line in Figure 5.14 is the maximum possible acceleration as defined by the agilitoid. Because the STM attempts to find direction of maximum available acceleration in the agiltoid, it will always strive toward this line, but can never cross it. The time scale needed in Figure 5.14 is such that the detailed shape of each maneuver is compressed. Figures 5.19 and 5.23 expand the time scale and are better representations of individual STM acceleration profiles.

Figure 5.15 overlays the boresight trace of the STM sensor (in yellow) with the ISM sensor (in blue) for direct comparison of the paths.

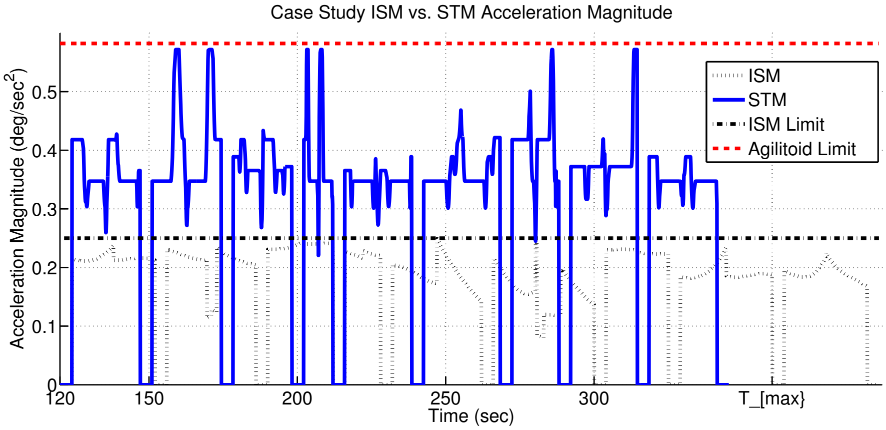

Figure 5.14: Body Acceleration Magnitude Comparison Between ISM and STM

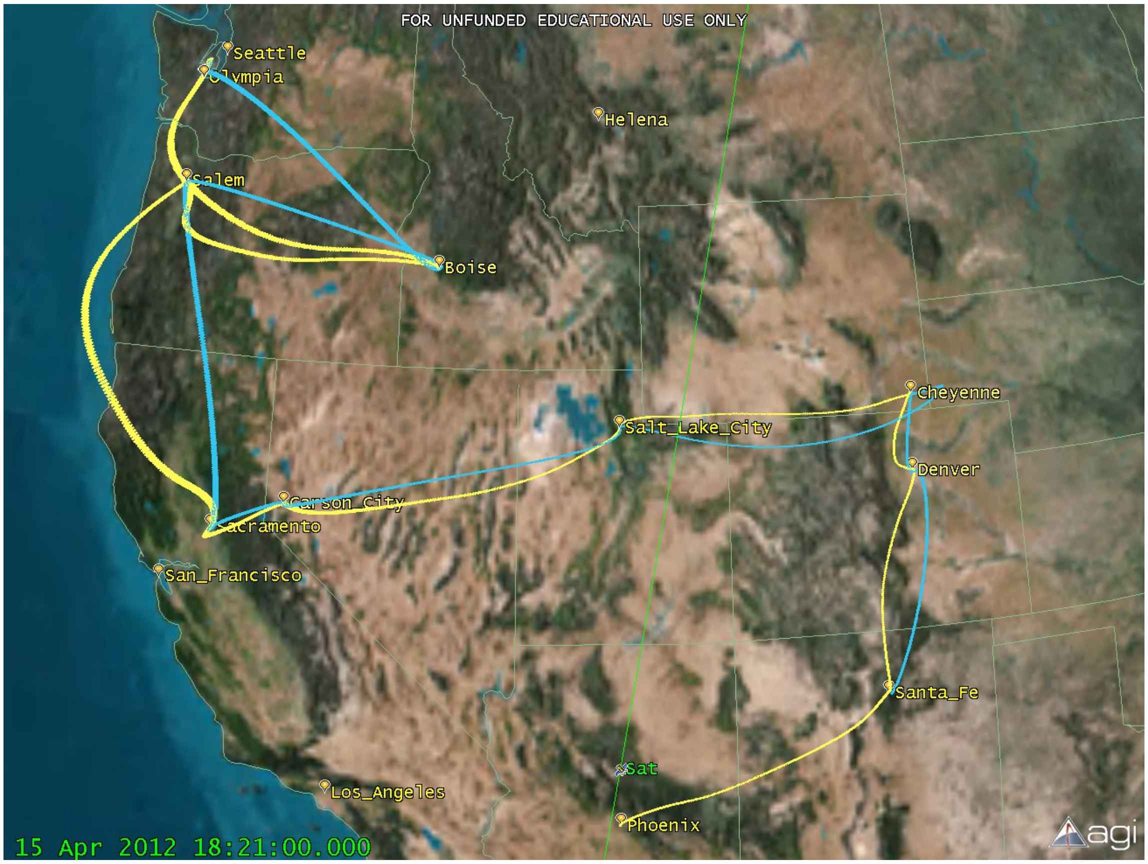

Figure 5.15: ISM (blue) versus STM (yellow) Boresight Traces at T_{max}

Detailed Examination of Two Maneuvers

Examining specific maneuvers will help to further demonstrate the difference between the ISM and STM. Maneuver 2 (between Boise and Salem) is the first maneuver considered.

The trajectories of the respective quaternions are shown in Figure 5.16, with the ISM quaternions as dotted lines and the STM quaternions using a plus symbol. It should be noted that due to relative motion effects, the final quaternions are not the same between these two maneuvers (most evident in q_1). This difference is due to the time that each maneuver arrives at the intended target node for collection (see Chapter 1). Other differences, other than completion time, are not readily apparent by looking at the quaternions, which is why the boresight traces of Figure 5.15 are helpful in understanding the sensor motion over the Earth.

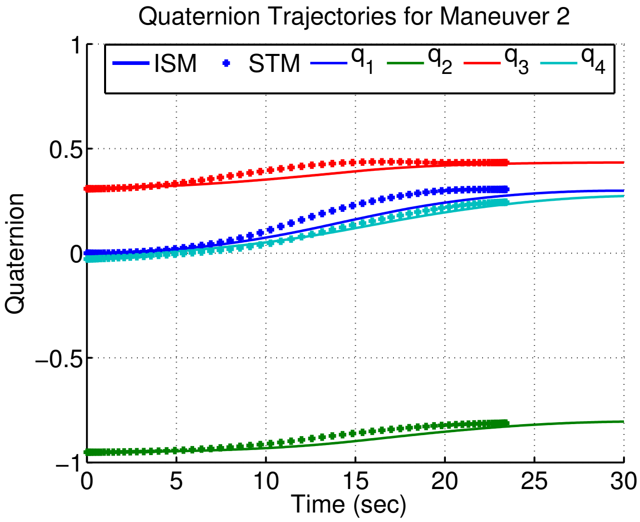

Figure 5.16: Quaternion Trajectories for Maneuver 2 using ISM and STM

The body rate trajectories for maneuver 2 are shown in 5.17. Specifically, Figure 5.17(a) shows the characteristically higher STM magnitude compared to the ISM. The overall rate of the STM was not just higher than the ISM, but achieved a greater rate than possible using the ISM because it peaked higher than the spherical limit imposed by the ISM. This was one of the primary reasons why the STM executed this maneuver faster than the ISM. The motion about X and Z axes were significantly faster than the ISM motion. This off-eigenaxis motion resulted in the boresight sweeping motion seen in Figure 5.15.

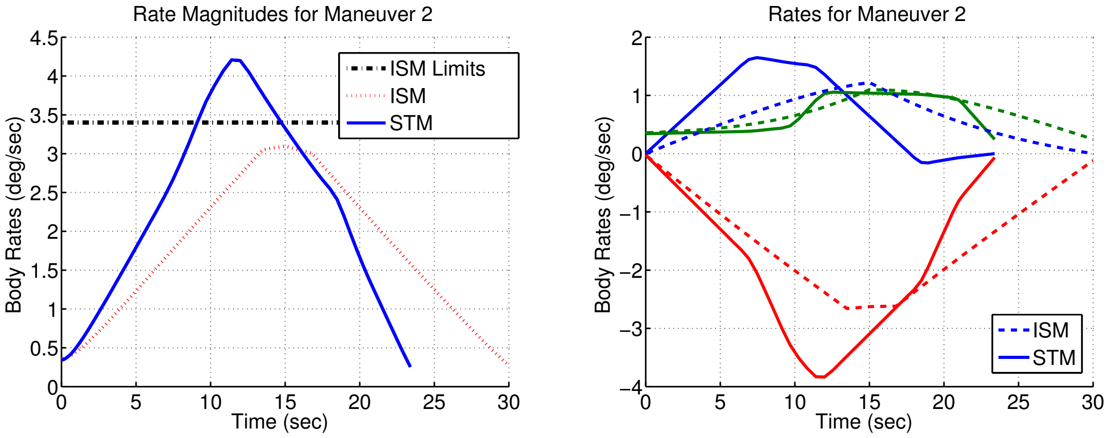

(a) (b)

Figure 5.17: Body Rate Trajectories for Maneuver 2 in Magnitude (a) and Body Axes (b)

The body acceleration magnitudes are compared in Figure 5.18(a) and demonstrate the expected higher STM magnitude (in blue) compared to the ISM (in red). The STM magnitude remained above the ISM spherical limit (in black). Body acceleration trajectories for maneuver 2 are also shown in 5.18(b) for all three axes. Note that the scale of the upper graph was increased to provide visibility into the ISM acceleration performance.

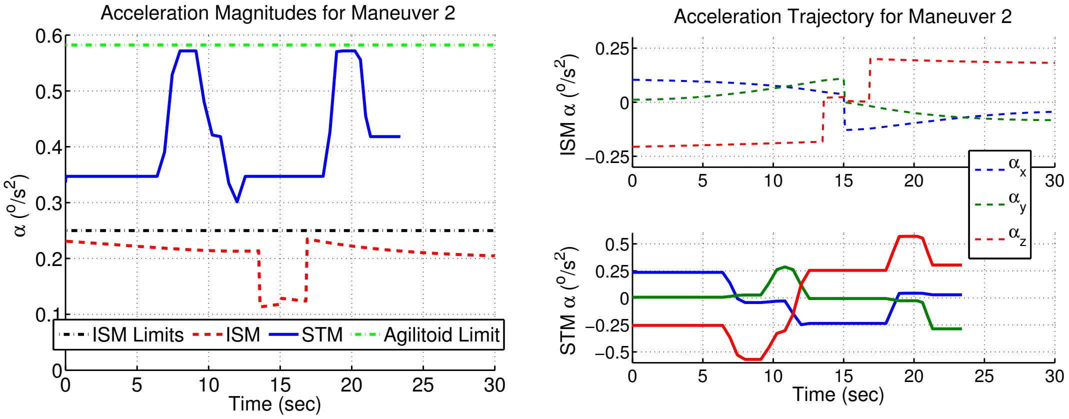

(a) (b)

Figure 5.18: Body Acceleration Trajectories for Maneuver 2 in Magnitude (a) and Body Axes (b)

This higher acceleration was the primary means of achieving the higher rates in Figure 5.17 and subsequent speed of execution. Because the STM allocated torque commands to each RW independently, in accordance with the problem formulation in (3.28), it achieved a higher acceleration by using the optimal combination of RW torques. The acceleration magnitude from Figure 5.18(a) was expanded to focus only on the STM in Figure 5.19(a). The specific RW torque commands used to achieve this acceleration are shown in Figure 5.19(b) (individual RW torque capacity is 0.11 Nm). Because the RWs were switching independently, the STM was able to realize a higher overall acceleration. Note that the agilitoid limit is the theoretical limit, thus, it can never be exceeded. The STM, however, will always strive toward this limit in an effort to execute the maneuver more quickly.

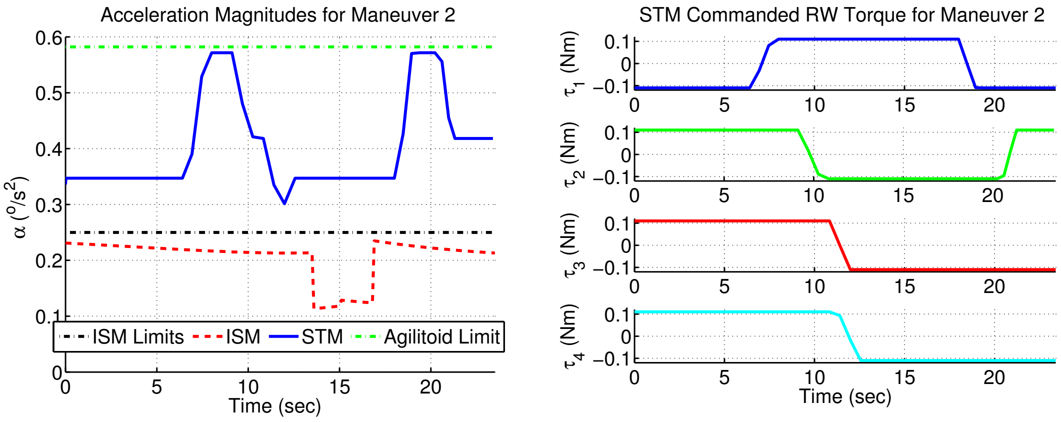

(a) (b)

Figure 5.19: Maneuver 2 Acceleration Zoomed-In (a) versus Reaction Wheel Torques (b)

The second maneuver presented is the transit between Salem and Sacramento (maneuver 3) because it has the most significant deviation in boresight path as seen in Figure 5.15.

The overall motion of ISM 3 was equivalent to an eigenaxis maneuver about the axis $\hat{\boldsymbol{e}} = [-0.007,\ 0.999,\ -0.010]$ for 23.8° of rotation. The STM equivalent angular distance for maneuver 3 was only 21.7°, but because the ISM and STM departed and arrived at the respective target nodes at different times, the equivalent angular distance was not expected to be the same. The values of $\hat{\boldsymbol{e}}$ indicate the overall change in attitude was primarily in the Y axis with very little motion in either X or Z axes. Specifically, this eigenaxis is a vector mostly aligned with the Y axis and less than 0.6° in either the X or Z axes.

The trajectories of the respective quaternions for maneuver 3 are shown in Figure 5.20, with the ISM quaternions as dotted lines and the STM quaternions using a plus symbol. The difference, other than completion time, is not readily apparent by looking at the quaternions, thus, the boresight plots of Figure 5.15 are essential.

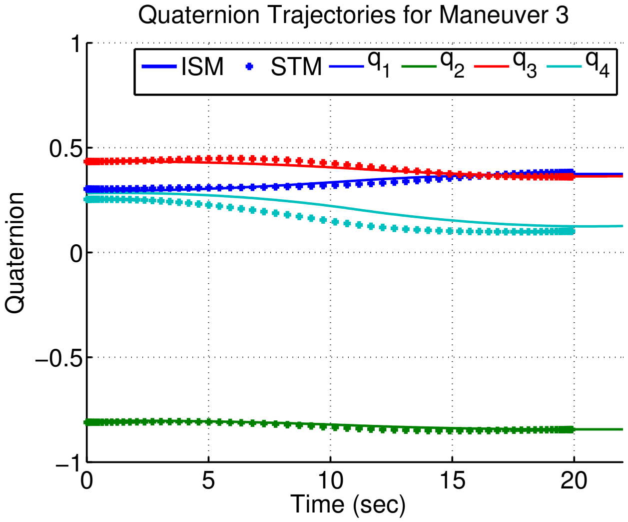

Figure 5.20: Quaternion Trajectories for Maneuver 3 using ISM and STM

Because this maneuver was almost a single-axis maneuver, the eigenaxis based ISM attempted to control the motion along each axis independently. Thus, the ISM drove the maneuver to be along the Y axis (in the direction of $\hat{\boldsymbol{e}}$) regardless of whether or not there was additional acceleration available in another axis. By definition, the ISM did not look for a higher agility axis, but transited about the $\hat{\boldsymbol{e}}$ axis as close to the spherically limited acceleration as possible. The STM remains free to choose the motion that best satisfies its constraints and maximizes its performance. This freedom from the bounds of eigenaxis motion is one of the fundamental characteristics of the STM [48]. By taking advantage of the additional capability within the agilitoid, the STM is able to maneuver more quickly. Figures 5.21(b) - 5.22 present precisely this behavior.

Similar to the previous maneuver example, Figure 5.21 contrasts the magnitude and individual axis performance of the body rates for each maneuver type. The ISM rates were primarily in the Y axis, as expected, but the STM motion utilized all three axes. The overall magnitude of the rate was not significantly higher, in contrast to the resulting shape of the boresight trajectory (i.e., away from the straight line path between the targets).

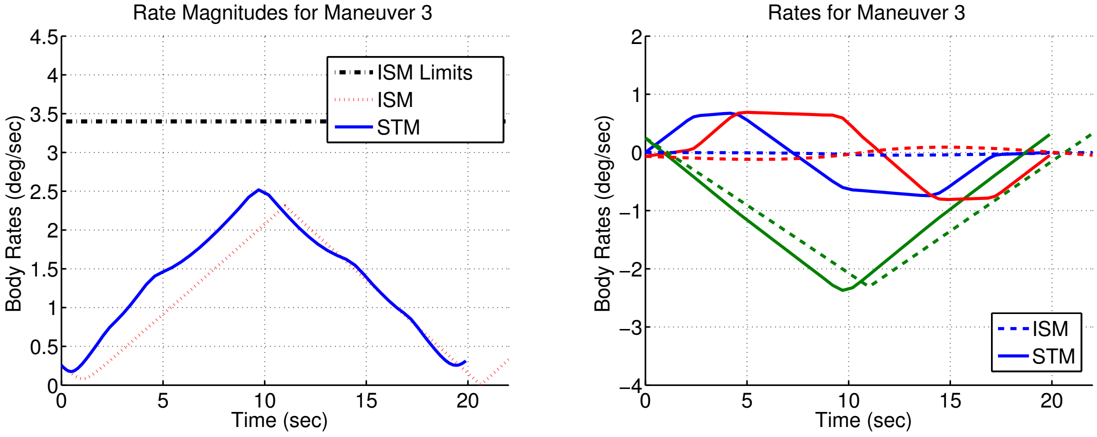

(a) (b)

Figure 5.21: Body Rate Trajectories for Maneuver 3 in Magnitude (a) and Body Axes (b)

Figure 5.22(a) clearly shows the increased acceleration possible using the STM (blue) because it used the more of the agilitoid than the ISM. The ISM acceleration remained at or close to the spherical limit, as expected. In Figure 5.22(b), the ISM acceleration (dashed lines) was primarily in the Y axis (in green) while the STM used all three axes simultaneously.

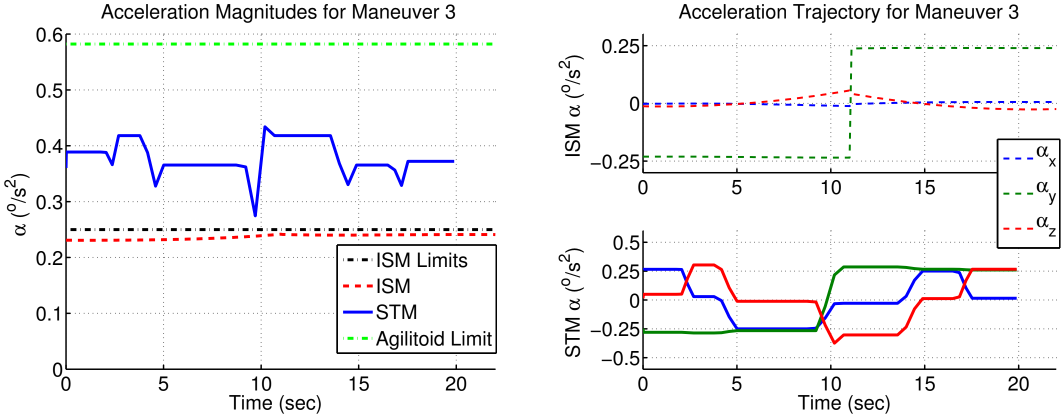

(a) (b)

Figure 5.22: Body Acceleration Trajectories for Maneuver 3 in Magnitude (a) and Detail (b)

The acceleration magnitude from Figure 5.22(a) was expanded to focus only on the STM (Figure 5.23(a)). The specific RW torque commands used to achieve this acceleration are shown in Figure 5.23(b). In contrast to the previous maneuver, however, the optimal switching time for three out of four RWs were at about 10 seconds.

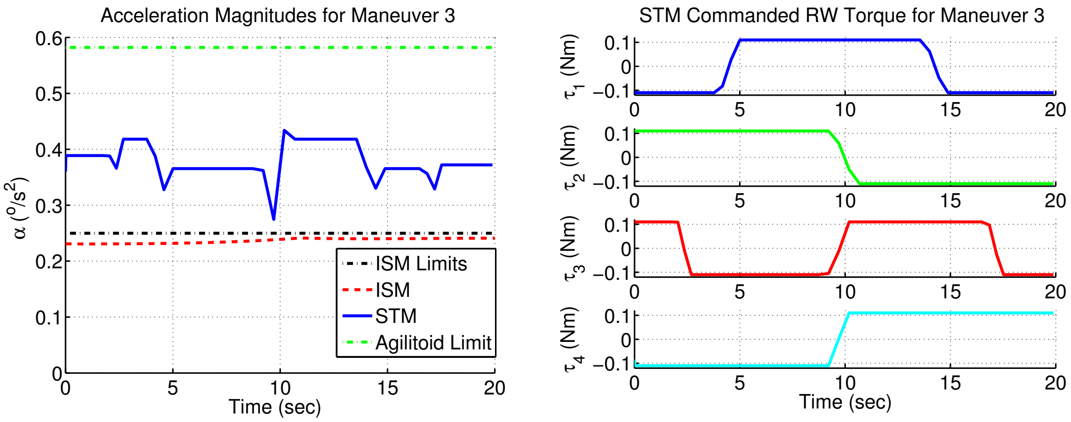

(a)

(b)

Figure 5.23: Maneuver 3 Acceleration Zoomed-In (a) versus Reaction Wheel Torques (b)

The off-eigenaxis motion and acceleration about the X and Z axes allowed the STM to utilize the axis of greatest agility and achieve better performance than the spherical limited ISM. This motion also created the boresight profile in Figure 5.15.

5.5 The γ ISM Plan

Finally, the performance of a third maneuver plan, shown in Figure 5.24 as the smaller magenta bars, was designed using ISMs but increased by the γ factor of 1.41. This plan represents a sensor with a 1.41 times larger RWs. The value for gamma was derived from the agilitoids in section 3.5.3.

The γ ISM based maneuver plan collected all ten targets in 237 seconds with specific node collection times listed in Table 5.4. Unvisited nodes are not listed in Table 5.4 for brevity.

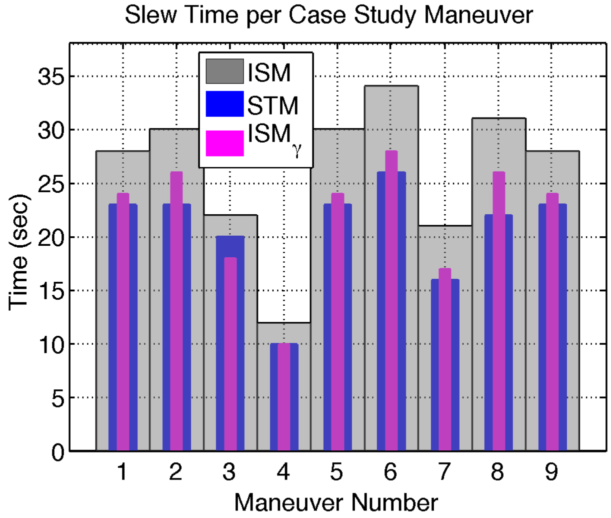

Figure 5.24: Individual Maneuver Time Comparison Between ISM, STM, and γ ISM

	ISM		STM		γ ISM	
Node	t^B	t^D	t^B	t^D	t^B	t^D
1	152	156	147.1	151.1	148	152
2	228	232	212.2	216.2	214	218
3	300	304	268.8	272.8	274	278
4	325	329	288.7	292.7	295	299
7	120	124	120.0	124.0	120	124
8	$\boxed{392}$	$\boxed{396}$	342.1	346.1	353	357
9	212	216	198.4	202.4	200	204
10	189	190	174.4	178.4	178	182
11	262	266	238.9	242.9	242	246
13	$\boxed{360}$	$\boxed{364}$	315.1	319.1	325	329

Table 5.4: Node Collect Times in Seconds After t_{epoch} for ISMs, STMs, and γ ISMs

The magnitude of the rates and accelerations are shown in Figures 5.25 - 5.26 against the ISM and STM plans respectively. Figure 5.25 demonstrates how the γ ISMs achieve very similar rate magnitudes to the STMs including values greater than the ISM spherical limit. This is to be expected due to the increase in size of the RWs. Figure 5.26 illustrates the effect of the γ factor in that the acceleration magnitudes are above the spherical limit for all maneuvers. Figure 5.27 shows all three maneuver plan types simultaneously and better illustrates the specific path taken by each maneuver plan. The γ ISM maneuver plan generally follows a similar path as the ISM plan, but employs larger α_{max} and ω_{max} values resulting in a faster transit times.

This increased performance of the γ ISM resulted in the less than 4.6 percent deviation from the overall time savings of the STM based plan (within 11 seconds over a 240 time window), demonstrating that STM performance can be estimated by the γ factor.

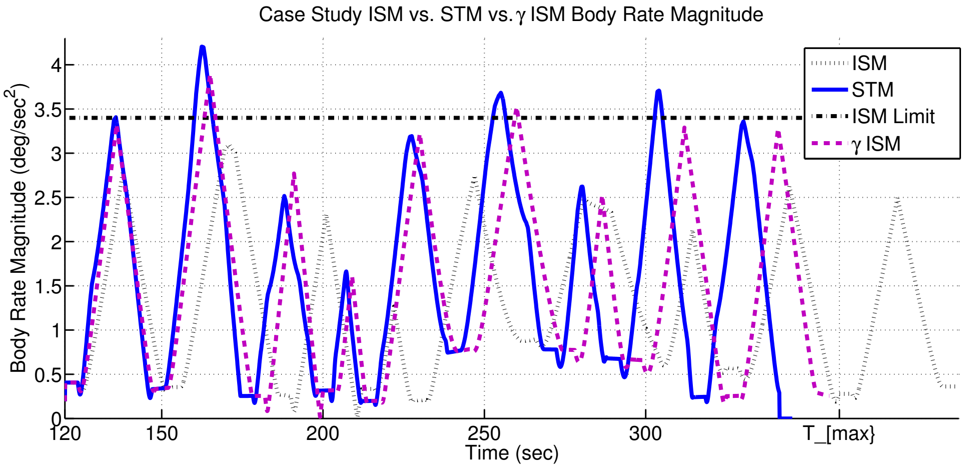

Figure 5.25: Body Rate Magnitude Comparison Between ISM, STM, and γ ISM

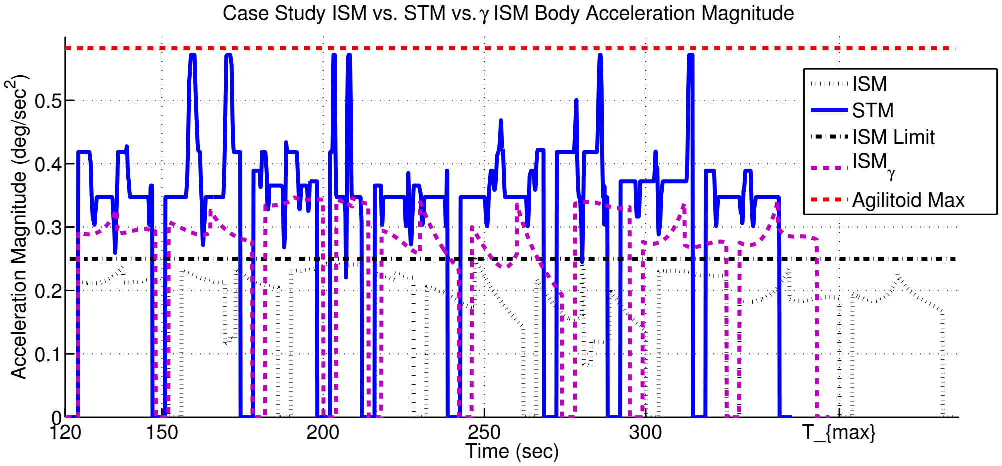

Figure 5.26: Body Acceleration Magnitude Comparison Between ISM, STM, and γ ISM

5.6 Summary

While the time saved and η performance is important, the most important result of using STMs is the ability to take more images or collects. Figure 5.27 shows that in same amount of time it took the STM sensor to collect all 10 targets, the same sensor was capable of only collecting eight targets implementing ISMs. Thus, the ability to collect targets is directly related to the agility of the sensor. Increasing the sensor agility using optimal control and being able to plan for the increased performance will increase the overall collection capability of a system. This chapter illustrated the elements of one possible solution to the space-based image collection planning problem presented in Chapter 4. By comparing ISMs with STMs as well as the new γ ISMs, it also demonstrated that the overall performance of STMs can be estimated with a simple factor, γ.

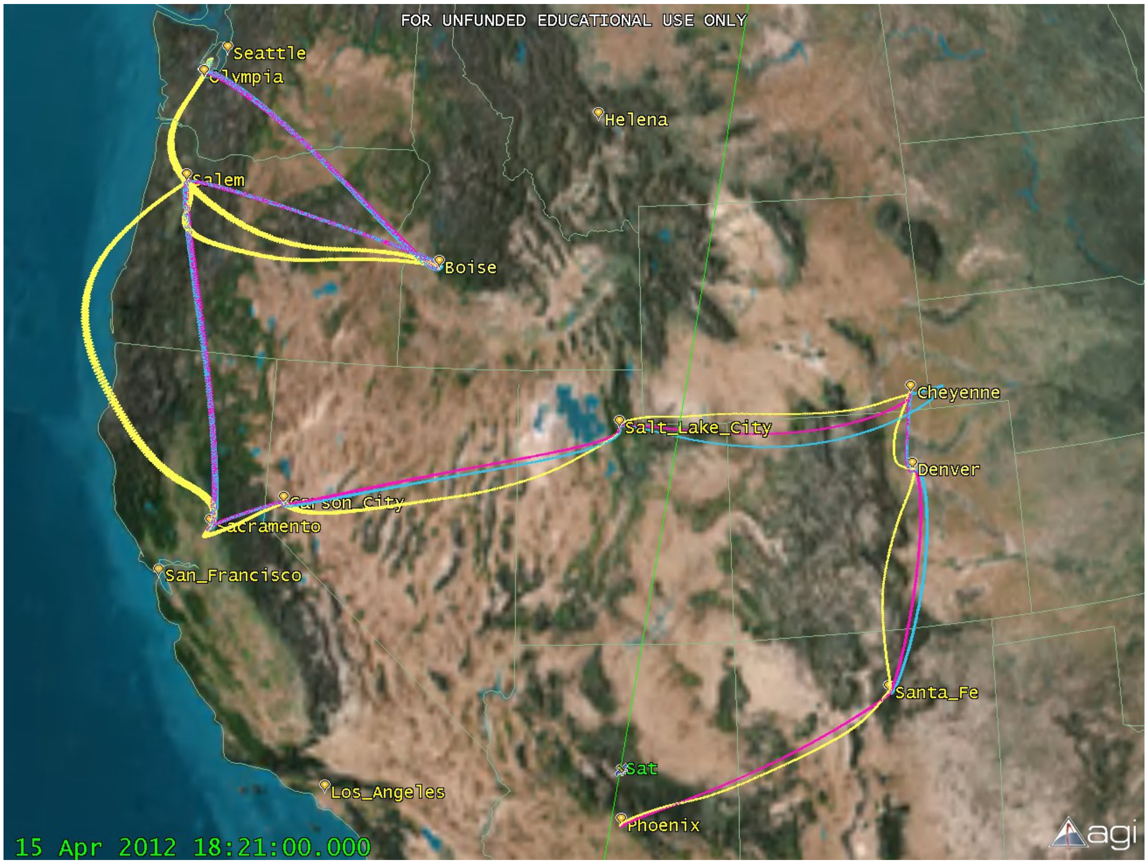

Figure 5.27: Relative Performance of ISM (blue), STM (yellow), and γ ISM (magenta) Collection Plans at T_{max}

CHAPTER 6:
Summary, Conclusions, and Future Work

6.1 Summary and Conclusions

This dissertation presented a new way to look at space-based image collection planning. A new set of equations for overhead targeting were presented that allowed the sensor attitude, rates and accelerations to be determined for a given target at a given time. These equations accommodate stationary or moving point targets as well as area scans using a scanning sensor.

The ability to increase a spacecraft's agility using optimal control was discussed in detail, beginning with the standard R2R maneuvers. The performance of optimal control and eigenaxis maneuvers were compared with each other. The concept of an agilitoid was presented and a new method for estimating the performance of optimal control maneuvers was derived and validated. Additionally, an original figure of merit, γ_a was defined for comparing the agility of two systems. This figure of merit was validated with over 1500 maneuvers across a variety of different conditions.

For the example system, the value of γ_a was 1.41, though results will vary with each system because the agilitoid is unique in shape and size for a particular system configuration and maneuvering algorithm. Several factors including: the individual reaction wheel capability, number, and configuration, the platform inertia values, and control allocation are all required to calculate the agiltoid.

The concept of γ_a can be applied in two primary ways. First, if a system is already deployed, γ_a represents the average performance increase that can be expected from the current system by using optimal control maneuvering. In other words, optimal control maneuvering yields the same average performance a larger version of the current system (torque and momentum), multiplied by γ_a, would achieve.

The second way to apply the γ_a concept is in the system design phase or pre-deployment. The γ_a represents the average decrease in size, weight, and power in reaction wheels using optimal control that can be expected to perform at the current level of performance. In other words, optimal control may allow a design to meet the desired specification while saving size, weight, or power in the attitude control system, multiplied by $1/\gamma_a$.

Optimal control NR2NR maneuvers were formulated and demonstrated (including specific maneuvers to connect sequential area scans), contributing to the body of time-optimal control literature beyond R2R. Finally, operational NR2NR maneuvers were designed and analyzed. These maneuvers overcame the inaccuracies of simply arriving at the same attitude earlier by calculating the correct attitude required at the given arrival time using the new targeting equations from Chapter 2. The NR2NR maneuvers resulted in a higher performance than the R2R maneuvers, specifically with slew maneuver time saved (η). However, it was also shown that γ_a is a valid figure of merit for estimating even NR2NR maneuvers. The increase in benefit from R2R to NR2NR implies that the closer one models the real operational system and constraints, the larger the benefit optimal control can provide.

Chapter 4 presented the problem of collection planning (i.e., how and which targets to collect from a sensor) while using optimal control maneuvers. Graph theory elements were introduced and examples were given for the space-based sensor application. The introductory problem was expanded to include more realistic elements that vary with time and are capable of incorporating time-optimal maneuvers. Problem $P1$ represents a new formulation of the time-varying overhead collection planning problem. The formulation for this new time-varying space-based image collection problem was presented as a hybrid optimal control problem.

Finally, a case study was presented to illustrate elements of a solution to the time-varying collection planning problem. A comparison was made between different maneuvering types and the overall performance of each using an operational real-world scenario was presented. In the case study, the collection window ended with the STM and γ_a ISM collecting 10 targets while the ISM was enroute to the eighth target, thus, the STM and γ_a ISM collected 20 percent more targets than the ISM (8/10). This simple example illustrated that while higher agility is often the immediate goal, a more agile collection capacity is the desired end result.

6.2 Future Work

Increasing the Sample Size for Agilitoid Development

This dissertation used a single spacecraft as a consistent example throughout. However, the agilitoid concepts and γ_a calculations should be validated across the entire span of different platforms and overhead sensors.

Explore the NR2NR Maneuver Space

New time-optimal NR2NR maneuvers were presented and demonstrated in Chapter 3, but additional work may be warranted to further explore the possible limits of NR2NR maneuvers. Specifically, there may be agility limitations based on the starting rates or accelerations, ending rates or acceleration. The difference between starting and ending motion may also be an agility limiting factor. The available agility is most likely affected by stored momentum (a byproduct of initial and final rates), but exactly how is currently not known.

Operational Planning Constraints

Additional variables, functions, or constraints may be necessary, depending on the complexity of the desired planning problem, and may also be placed on the collect effort by a requesting user. For example, if the planning problem incorporates a capacity constraint for on-board storage by the sensor, then a capacity impact for each node must be also be defined [78, 107, 108]. The capacity of the system may be defined in other terms such as electrical power or simply time available to collect. The latter is an example of a specific dependence on time. In the most general sense, it would represented by $C_i\left(\boldsymbol{Y}_i(\cdot), \boldsymbol{X}(\cdot)\right)$.

Many operational constraints may be successfully incorporated into the access window constraints or into a time varying BVF.

Another aspect of operational constraints are that they allow for unique behaviors. For instance, even with a capacity constraint on the sensor, it may be desirable to include the ability to down-link data within the overall planning cycle and thus increase its overall capacity. These special capacity reducing nodes must be defined carefully and will most likely require multiple visits or variable servicing time. Another example is a power available constraint. In this case, a sun-pointing node would be defined with no collection benefit, but an impact on the power available.

Multi-Sensor Planning

This dissertation developed the time-varying graph planning problem for a single sensor. The need for a more complete solution to the greater problem drives an expansion of the single sensor planning problem to include multiple sensors. These sensors may be on the same platform or on entirely different platforms. In fact, the multi-sensor planning problem should be capable of multiple and varied platforms to include satellites, airborne collectors, and even ground based sensors. Any conceivable sensor may be included if the motion and pointing dynamics relative to its intended targets can be specified.

If a single sensor collection planning problem is similar to an OP then the multi-sensor planning problem corresponds to a team orienteering problem (TOP). In the TOP, each sensor must find its own targets and sequence. However, the objective is the team's overall benefit and not the collected benefit of a single sensor. The first to use the team orienteering label for multiple players or sensors was [109]. The single OP has been show to be an NP-hard problem [84] and because the TOP reduces to the OP for a single sensor, it is also an NP-hard problem.

For every sensor, $k \in K$, a subscript is added to the sensor data defined under the single sensor formulation. For example, $\boldsymbol{X}_k(t)$ represents the data vector of sensor k.

The BVF of a node must be adjusted for a particular sensor, $BVF_{ik}(\cdot)$, and thus a sensor preference or restriction can be introduced into the planning process. Adding the sensor subscript k to all other node and planning elements (including servicing time, time windows, operational constraints like capacity, etc.) allows any sensor-node relationships to be captured. Each sensor may have its own capability to maneuver between target nodes and directly affects the time it takes to travel (slew) from one node to the next. Thus, δt_{ijk} becomes the time it takes sensor k to transit between nodes i and j.

$$\delta t_{ijk} = \text{ argmin } J_{slew}\left[\boldsymbol{X}_k(\cdot), \boldsymbol{Y}_i(\cdot), \boldsymbol{Y}_j(\cdot), \boldsymbol{u}_k(\cdot), t_0, t_f\right] \tag{6.1}$$

Table 6.1 shows a possible form for the data vectors and variables for the multi-sensor problem.

Nomenclature	Definition
$\boldsymbol{X}_k(t)$	Data vector of sensor k
$\boldsymbol{Y}_i(t)$	Data vector of node i
$BVF_{ik}\left(\boldsymbol{Y}_i(\cdot),\boldsymbol{X}_k(\cdot),\boldsymbol{t}^B\right)$	Benefit of collecting node i by sensor k
$C_{ik}\left(\boldsymbol{Y}_i(\cdot),X_k(\cdot)\right)$	Capacity impact of node i to sensor k
$T^S_{ik}\left(\boldsymbol{Y}_i(\cdot),\boldsymbol{X}_k(\cdot)\right)$	Servicing time required at node i by sensor k
$T^E_{ik}\left(\boldsymbol{Y}_i(\cdot),\boldsymbol{X}_k(\cdot)\right)$	Early (start of) time window of node i for sensor k
$T^L_{ik}\left(\boldsymbol{Y}_i(\cdot),\boldsymbol{X}_k(\cdot)\right)$	Late (completion of) time window of node i for sensor k
δt_{ijk}	Maneuver time from node i to node j by sensor k
$J_{slew}\left[\boldsymbol{X}_k(\cdot),\boldsymbol{Y}_{ik}(\cdot),\boldsymbol{Y}_{jk}(\cdot),\boldsymbol{u}_k(t),t_0,t_f\right]$	Objective function for slew maneuver
$\boldsymbol{u}_k(t)$	Control history for sensor k that minimizes J_{slew}
t^B_{ik}	Begin collection time for sensor k in collecting node i
t^D_{ik}	Departure time for sensor k from node i
Δ_{ijk}	$\{1\}$ if sensor k traveled on arc (i,j); $\{0\}$ otherwise

Table 6.1: Multi-Sensor Formulation Nomenclature

A multi-sensor can then be formulated similar to (4.51) - (4.67) with the appropriate k subscripts, summations and constraints added. For example, the overall plan benefit in (4.51) would also be summed over all $k \in K$ for a multi-sensor benefit.

THIS PAGE INTENTIONALLY LEFT BLANK

References

[1] J. C. Pemberton and L. G. Greenwald, “On the need for dynamic scheduling of imaging satellites,” *International Archives of Photogrammetry Remote Sensing and Spatial Information Sciences*, vol. 34, no. 1, pp. 165–171, 2002.

[2] Orbital Sciences Corp. (2014). GeoEye-1 : Highest resolution commercial imager launched to date. [Online]. Available: https://www.orbital.com/SatelliteSpaceSystems/Publications/GeoEye-1_factsheet.pdf

[3] J. Sanchez, *Space Image Processing*. Boca Raton, FL: CRC Press, 1999.

[4] H.-S. Wong, Y. L. Yao, and E. S. Schlig, “TDI charge-coupled devices: Design and applications,” *IBM Journal of Research and Development*, vol. 36, no. 1, pp. 83–106, 1992.

[5] W. J. Larson and J. R. Wertz, Eds., *Space Mission Analysis and Design*, 2nd ed. Torrance, CA: Microcosm, Inc, 1992.

[6] G. C. Holst, *CCD Arrays, Cameras, and Displays*, 2nd ed. WinterPark, FL: Bellingham, WA: JCD Pub., 1998.

[7] I. Bayir, “IKONOS collection capability with the direct tasking from a regional operation center,” in *International Conference on Recent Advances in Space Technologies*, 2003, pp. 30–33.

[8] Hamamatsu Photonics. (No Date). Board-level TDI camera c10000-201. [Online]. Available: http://www.hamamatsu.com/jp/en/product/alpha/B/C10000-201/index.html

[9] Fairchild Imaging. (2012). CCD 5061. [Online]. Available: http://www.fairchildimaging.com/catalog/focal-plane-arrays/ccd/tdi-ccds/ccd-5061

[10] G. Lerner, “Three-axis attitude determination,” in *Spacecraft Attitude Determination Control*, J. R. Wertz, Ed. Dordrecht, The Netherlands: Reidel Publishing Co., 1978, pp. 420–428.

[11] T. Strikwerda, K. Strohbehn, K. Fowler, and D. Skillman, “Space telescope moving target tracking,” in *AIAA Guidance, Navigation and Control Conference*, vol. 1, Aug 1985, pp. 67–72.

[12] J. R. Etter, “A solution of the time-optimal euler rotation problem,” in *Proceedings of the AIAA Guidance, Navigation, and Control Conference*, vol. 2, 1989, pp. 1441–1449.

[13] G. Creamer, P. DeLaHunt, S. Gates, and M. Levenson, “Attitude determination and control of clementine during lunar mapping,” *Journal of Guidance, Control, and Dynamics*, vol. 19, no. 3, pp. 505–511, 1996.

[14] S. Ristz and J. Bracken, “GLAST observatory slew rate and pointing knowledge issues,” NASA Goddard Space Flight Center, Greenbelt, MD, May 2000.

[15] B. Wie, D. Bailey, and C. Heiberg, “Rapid multitarget acquisition and pointing control of agile spacecraft,” *Journal of Guidance, Control, and Dynamics*, vol. 25, no. 1, pp. 96–104, Jan. 2002.

[16] I. M. Ross, P. Sekhavat, A. Fleming, and Q. Gone, “Optimal feedback control: Foundations, examples, and experimental results for a new approach,” *Journal of Guidance, Control, and Dynamics*, vol. 31, no. 2, pp. 307–321, 2008.

[17] T. Lee, M. Leok, and N. H. McClamroch, “Time optimal attitude control for a rigid body,” in *American Control Conference*, 2008, pp. 5210–5215.

[18] J. E. Sedalk and M. B. Houghton, “Lunar reconnaissance orbiter (LRO) attitude maneuver planning,” in *International Symposium on Spaceflight Dynamics*, Toulouse, France, Sep. 2009.

[19] Y. Kim and C. Ahn, “Point targeting of multisatellites via a virtual structure formation flight scheme,” *Journal of Guidance, Control, and Dynamics*, vol. 32, no. 4, pp. 1330–1344, Jul. 2009.

[20] B. M. Yutko and R. G. Melton, “Optimizing spacecraft reorientation maneuvers using a pseudospectral method,” *Journal of Aerospace Engineering*, vol. 2, no. 1, pp. 1–14, 2010.

[21] M. Karpenko, A. Fleming, S. Bhatt, N. Bedrossian, and I. M. Ross, “First flight results on time-optimal spacecraft slews,” *Journal of Guidance, Control and Dynamics*, vol. 35, no. 2, pp. 367–376, Mar. 2012.

[22] N. S. Ibrahim, “Attitude and orbit control of small satellites for autonomous terrestrial target tracking,” Master’s thesis, Dept. Inst. Aerospace Stud., University of Toronto, Toronto, Canada, 2013.

[23] M. D. Shuster and S. D. Oh, “Three-axis attitude determination from vector observations,” *Journal of Guidance, Control, and Dynamics*, vol. 4, no. 1, pp. 70–77, Jan. 1981.

[24] F. L. Markley and D. Mortari, “How to estimate attitude from vector observations,” in *AAS/AIAA Astrodynamics Specialist Conference*, vol. 99-427, Aug. 1999.

[25] F. L. Markley, “Fast quaternion attitude estimation from two vector measurements,” *Journal of Guidance, Control, and Dynamics*, vol. 25, no. 2, pp. 411–414, 2002.

[26] M. D. Shuster, “The QUEST for better attitudes,” *Journal of the Astronautical Sciences*, vol. 54, no. 3-4, pp. 657–683, 2006.

[27] W. Jerkovsky, “A computationally efficient pointing command law,” *AIAA Paper 88-2208*, Aug. 1983.

[28] H. Hablani, “Design of a payload pointing control system for tracking moving objects,” *Journal of Guidance, Control and Dynamics*, vol. 12, no. 3, pp. 365–374, May 1989.

[29] W. G. Breckenridge and G. K. Man, “Quaternions for galileo scan platform control,” in *AAS Paper 83-321*, Jan. 1984.

[30] H. Weiss, “Quaternion-based rate/attitude tracking system with application to gimbal attitude control,” *Journal of Guidance, Control, and Dynamics*, vol. 16, no. 4, pp. 609–616, Jul. 1993.

[31] H. Schaub, R. D. Robinett, and J. L. Junkins, “Globally stable feedback laws for near- minimum-fuel and near-minimum-time pointing maneuvers for a landmark-tracking spacecraft,” *The Journal of the Astronautical Sciences*, vol. 44, pp. 443–462, 1996.

[32] L. Schimelevich, “Attitude update for pointing systems while lock-in at stationary targets,” in *AIAA Guidance, Navigation and Control Conference and Exhibit*, Denver, CO, Aug. 2000.

[33] M. R. Long, “Spacecraft attitude tracking control,” Master’s thesis, Dept. Aerospace and Ocean Eng. Virginia Polytechnical Institute and State Universtiy, Blacksburg, VA, 1999.

[34] B. Goeree and B. Shucker, “Geometric attitude control of a small satellite for ground tracking maneuvers,” in *Proceedings of the 13 th AIAA/USU Conference on Small Satellites*, Logan, UT, Aug. 1999.

[35] X. Chen, W. Steyn, and Y. Hashida, “Ground-target tracking control of earth-pointing satellites,” in *AIAA Guidance, Navigation and Control Conference and Exhibit*, Denver, CO, Aug. 2000.

[36] M. D. Shuster, “A survey of attitude representations,” *The Journal of the Astronautical Sciences*, vol. 1, no. 4, pp. 439–517, Dec. 1993.

[37] D. A. Vallado, *Fundamentals of Astrodynamics and Applications*, 2nd ed. El Segundo, CA: Microcosm Press, 2001.

[38] B. Wie, *Space Vehicle Dynamics and Control*. Reston, VA: AIAA, 2008.

[39] M. J. Sidi, *Spacecraft Dynamics and Control: A Practical Engineering Approach*. New York: Cambridge University Press, 2000.

[40] R. R. Bate, D. D. Mueller, J. E. White, and W. W. Saylor, *Fundamentals of Astrodynamics*. New York: Dover Publications, Inc, 2013.

[41] T. R. Kane, *Dynamics, Theory and Applications*, ser. McGraw-Hill Series in Mechanical Engineering. New York: McGraw-Hill, Inc, 1985.

[42] H. B. Hablani, "Target acquisition, tracking, spacecraft attitude control, and vibration suppression with IPFM reaction jet controllers," in *Proceedings of the AIAA Guidance, Navigation, and Control Conference*, Aug. 1992.

[43] G. M. Siouris, *Aerospace Avionics Systems: a Modern Synthesis*. Academic Press, 1993.

[44] K. D. Bilimoria and B. Wie, "Time-optimal three-axis reorientation of a rigid spacecraft," *Journal of Guidance, Control, and Dynamics*, vol. 16, no. 3, pp. 446–452, Jun. 1993.

[45] H. Shen and P. Tsiotras, "Time-optimal control of axisymmetric rigid spacecraft using two controls," *Journal of Guidance, Control and Dynamics*, vol. 22, no. 5, pp. 682–694, 1999.

[46] R. J. Proulx and I. M. Ross, "Time-optimal reorientation of asymmetric rigid bodies," in *Advances in the Astronautical Sciences*, vol. 109, 2001, pp. 1207–1227.

[47] F. Fahroo and I. M. Ross, "Costate estimation by a legendre pseudospectral method," *Journal of Guidance, Control, and Dynamics*, vol. 24, no. 2, pp. 270–277, 2001.

[48] A. Fleming and I. M. Ross, "Optimal control of spinning axisymmetric spacecraft: A pseudospectral approach," in *AIAA Guidance, Navigation and Control Conference and Exhibit*, Honolulu, HI, Aug. 2008.

[49] M. Karpenko, S. Bhatt, N. Bedrossian, A. Fleming, and I. Ross, "Flight implementation of pseudospectral optimal control for the TRACE space telescope," in *AIAA Guidance, Navigation, and Control Conference*, Portland, OR, Aug. 2011.

[50] M. Karpenko, S. Bhatt, N. Bedrossian, and I. Ross, “Design and flight implementation of operationally relevant time-optimal spacecraft maneuvers,” in *AIAA/AAS Astrodynamics Specialist Conference*, Girdwood, AK, Aug 2011.

[51] N. Bedrossian, S. Bhatt, M. Lammers, L. Nguyen, and Y. Zhang, “First ever flight demonstration of zero propellant maneuver(TM) attitute control concept,” in *AIAA Guidance, Navigation and Control Conference and Exhibit*, Hilton Head, SC, Aug. 2007.

[52] Surrey Space Technologies, Ltd. (No Date). SSTL microwheels. [Online]. Available: http://www.sstl.co.uk/getattachment/f31aaa67-3750-4a8a-9742-c1cd800c0a5b/Microwheels

[53] F. L. Markley, R. G. Reynolds, F. X. Liu, and K. L. Lebsock, “Maximum torque and momentum envelopes for reaction wheel arrays,” *Journal of Guidance, Control, and Dynamics*, vol. 33, no. 5, pp. 1606–1614, Oct. 2010.

[54] A. Bryson and Y. Ho, *Applied Optimal Control*. Waltham, MA: Balisdel, 1969.

[55] M. Karpenko and M. Ross, “Implementation of shortest-time maneuvers for generic CMG steering laws,” in *AIAA/AAS Astrodynamics Specialist Conference*, Mineapolis, MN, Aug. 2012.

[56] A. Fleming, P. Sekhavat, and I. M. Ross, “Minimum-time reorientation of a rigid body,” *Journal of Guidance, Control, and Dynamics*, vol. 33, no. 1, pp. 160–170, Jan. 2010.

[57] S. R. Crews, “Increasing slew performance of reaction wheel attitude control systems,” Master’s thesis, Dept. Mech. and Aerospace Eng., Naval Postgraduate School, Monterey, CA, 2013.

[58] I. M. Ross, *A Primer on Pontryagin’s Principle in Optimal Control*. Carmel, CA: Collegiate Publishers, 2009.

[59] L. S. Pontryagin, *Optimal control and differential games: collection of papers*. Providence, RI: American Mathematical Society, 1990, vol. 185.

[60] I. M. Ross and M. Karpenko, “A review of pseudospectral optimal control: From theory to flight,” *Annual Reviews in Control*, vol. 36, no. 2, pp. 182–197, Dec. 2012.

[61] I. M. Ross, “A beginner’s guide to DIDO: A MATLAB application package for solving optimal control problems,” Elissar, LLC, Monterey, CA, Tech. Rep. TR-711, 2007.

[62] H. B. Hablani, “Tracking system for tracking targets with a spacecraft,” U.S. Patent 5 400 033, Mar. 21, 1995.

[63] Astrium. (2012). Astrium GEO-information services SPOT international price list. [Online]. Available: http://www2.astrium-geo.com/files/pmedia/public/r146_9_pricelist_spot_en_2012.pdf

[64] P. Palmer, *The Complete Orienteering Manual*. Ramsbury, Wiltshire, England: Crowood Press, 1997.

[65] D. Feillet, P. Dejax, and M. Gendreau, “Traveling salesman problems with profits,” *Transportation Science*, vol. 39, no. 2, pp. 188–205, May 2005.

[66] M. Gendreau, G. Laporte, and F. Semet, “A branch-and-cut algorithm for the undirected selective traveling salesman problem,” *Networks*, vol. 32, no. 4, pp. 263–273, Dec. 1998.

[67] S. Kataoka, T. Yamada, and S. Morito, “Minimum directed 1-subtree relaxation for score orienteering problem,” *European Journal of Operational Research*, vol. 104, no. 1, pp. 139–153, 1998.

[68] E. Balas, “The prize collecting traveling salesman problem,” *Networks*, vol. 19, no. 6, pp. 621–636, Oct. 1989.

[69] P. Vansteenwegen, W. Souffriau, and D. V. Oudheusden, “The orienteering problem: A survey,” *European Journal of Operational Research*, vol. 209, no. 1, pp. 1–10, Feb. 2011.

[70] S. Rojanasoonthon, J. F. Bard, and S. D. Reddy, “Algorithms for parallel machine scheduling: a case study of the tracking and data relay satellite system,” *Journal of the Operational Research Society*, vol. 54, no. 8, pp. 806–821, Aug. 2003.

[71] D. Long and M. Fox, “The 3rd international planning competition: Results and analysis,” *Joint Artificial Intelligence Research*, vol. 20, pp. 1–59, 2003.

[72] S. Zilberstein, J. Koehler, and S. Koenig, Eds., *International Planning Competition*, Whistler, BC, Canada, Jun. 2004.

[73] B. A. Conway, C. M. Chilan, and B. J. Wall, “Evolutionary principles applied to mission planning problems,” *Celestial Mechanics and Dynamical Astronomy*, vol. 97, no. 2, pp. 73–86, Dec. 2006.

[74] B. J. Wall and B. A. Conway, “Genetic algorithms applied to the solution of hybrid optimal control problems in astrodynamics,” *Journal of Global Optimization*, vol. 44, no. 4, pp. 493–508, Sep. 2008.

[75] C. M. Chilan and B. A. Conway, “Using genetic algorithms for the construction of a space mission automaton,” in *IEEE Congress on Evolutionary Computation*, 2009, pp. 2316–2323.

[76] J. Wang, X. Zhu, and D. Qiu, “Emergency scheduling of multiple imaging satellites with dynamic merging,” in *SpaceOps 2012 Conference*, Stockholm, Sweden, Jun. 2012.

[77] J. A. Englander, B. A. Conway, and T. Williams, “Automated mission planning via evolutionary algorithms,” *Journal of Guidance, Control, and Dynamics*, vol. 35, no. 6, pp. 1878–1887, Nov. 2012.

[78] J. F. Cordeau, “A branch-and-cut algorithm for the dial-a-ride problem,” *Operations Research*, vol. 54, no. 3, pp. 573–586, May 2006.

[79] D. B. West, *Introduction to Graph Theory*, 2nd ed. Upper Saddle River, N.J: Prentice Hall, 2001.

[80] P. Vansteenwegen, W. Souffriau, G. V. Berghe, and D. V. Oudheusden, “A guided local search metaheuristic for the team orienteering problem,” *European Journal of Operational Research*, vol. 196, no. 1, pp. 118–127, Jul. 2009.

[81] R. Ramesh, Y.-S. Yoon, and M. H. Karwan, “An optimal algorithm for the orienteering tour problem,” *ORSA Journal on Computing*, vol. 4, no. 2, pp. 155–165, May 1992.

[82] Y. Dumas, J. Desrosiers, E. Gelinas, and M. M. Solomon, “An optimal algorithm for the traveling salesman problem with time windows,” *Operations Research*, vol. 43, no. 2, pp. 367–371, Mar. 1995.

[83] M. Gendreau, A. Hertz, G. Laporte, and M. Stan, “A generalized insertion heuristic for the traveling salesman problem with time windows,” *Operations Research*, vol. 46, no. 3, pp. 330–335, 1998.

[84] B. L. Golden, L. Levy, and R. Vohra, “The orienteering problem,” *Naval Research Logistics*, vol. 34, no. 3, pp. 307–318, 1987.

[85] A. F. Herz and A. Mignogna, “Collection planning for the OrbView-3 high resolution imagery satellite,” in *SpaceOps 2006 Conference*, Rome, Italy, Jun. 2006.

[86] W. Martin, “Satellite image collection optimization,” *Optical Engineering*, vol. 41, no. 9, pp. 2083–2087, 2002.

[87] C. Chekuri and M. Pal, “A recursive greedy algorithm for walks in directed graphs,” in *IEEE FOCS*, 2005, pp. 245–253.

[88] U.S. Geological Survey. (2013, May). Landsat: A global land-imaging mission. [Online]. Available: http://pubs.usgs.gov/fs/2012/3072/

[89] Y. Mai and P. Palmer, "Fast algorithm for prediction of satellite imaging and communication opportunities," *Journal of Guidance, Control, and Dynamics*, vol. 24, no. 6, pp. 1118–1124, Nov. 2001.

[90] J. Mann, D. Berkenstock, and S. Augenstein, "Satellite scheduling system using crowd-sourced data," U.S. Patent 20 140 040 282, Aug, 2013.

[91] J. DeGumbia, M. Woodard, and S. Stezelberger, "A COTS-based attitude dependent contact scheduling system," in *Space Ops 2006 Conference*, Rome, Italy, Jun. 2006.

[92] P. B. de Selding, "DigitalGlobe raising GeoEye-1's orbit to keep up with commercial imagery demand," *Space News*, Aug. 2013. [Online]. Available: http://www.spacenews.com/article/financial-report/36906digitalglobe-raising-geoeye-1%E2%80%99s-orbit-to-keep-up-with-commercial

[93] M. M. Solomon and J. Desrosiers, "Survey paper—time window constrained routing and scheduling problems," *Transportation Science*, vol. 22, no. 1, pp. 1–13, 1988.

[94] T. Shima and S. J. Rasmussen, *UAV Cooperative Decision and Control: Challenges and Practical Approaches*. Philadelphia, PA: Society for Industrial and Applied Mathematics, 2009.

[95] F. V. Fomin and A. Lingas, "Approximation algorithms for time-dependent orienteering," *Information Processing Letters*, vol. 83, pp. 57–62, 2001.

[96] A. J. Coles, A. Coles, M. Fox, and D. Long, "Temporal planning in domains with linear processes," in *Proceedings of the Twenty-First International Joint Conference on Artificial Intelligence*, 2009, pp. 1671–1676.

[97] C. Chekuri, N. Korula, and M. Pál, "Improved algorithms for orienteering and related problems," *ACM Transactions on Algorithms*, vol. 8, no. 3, pp. 1–27, Jul. 2012.

[98] J. Li, "Model and algorithm for time-dependent team orienteering problem," in *Advanced Research on Computer Education, Simulation and Modeling*. Berlin, Germany: Springer Berlin-Heidelberg, 2011, pp. 1–7.

[99] J. Li, "Research on team orienteering problem with dynamic travel times," *Journal of Software*, vol. 7, no. 2, pp. 249–255, Feb. 2012.

[100] C. Schumacher, P. R. Chandler, S. J. Rasmussen, and D. Walker, "Task allocation for wide area search munitions with variable path length," in *American Control Conference*, vol. 4, 2003, pp. 3472–3477.

[101] E. H. Kivelevitch, K. Cohen, and M. Kumar, "A market-based solution to the multiple depots, multiple traveling salesmen problem with profits," in *AIAA Infotech @ Aerospace Conference*, Boston, MA, Aug. 2013.

[102] J. Pietz, "A generalized orienteering problem for optimal search and interdiction planning," Ph.D. dissertation, Dept. Operations Research, Naval Postgraduate School, Monterey, CA, Sep. 2013.

[103] C. M. Chilan and B. A. Conway, "Automated design of multiphase space missions using hybrid optimal control," *Journal of Guidance, Control, and Dynamics*, vol. 36, no. 5, pp. 1410–1424, Sep. 2013.

[104] M. Savelsbergh, "Local search in routing problems with time windows," *Annuls of Operations Research*, vol. 4, no. 1, pp. 285–305, Dec. 1985.

[105] Satellite Imaging Corp. (No Date). IKONOS stereo satellite imagery. [Online]. Available: http://www.satimagingcorp.com/svc/ikonos-stereo-satellite-images.html

[106] M. B. Do, J. Benton, M. Van Den Briel, and S. Kambhampati, "Planning with goal utility dependencies." in *International Joint Conferences on Artificial Intelligence*, Hyderabad, India, 2007, pp. 1872–1878.

[107] S. Ropke, J. F. Cordeau, and G. Laporte, "Models and branch-and-cut algorithms for pickup and delivery problems with time windows," *Networks*, vol. 49, no. 4, pp. 258–272, Jul. 2007.

[108] C. Tarantilis, F. Stavropoulou, and P. Repoussis, "The capacitated team orienteering problem: A bi-level filter-and-fan method," *European Journal of Operational Research*, vol. 224, no. 1, pp. 65–78, Jan. 2013.

[109] I. Chao, B. L. Golden, and E. A. Wasil, "The team orienteering problem," *European Journal of Operational Research*, vol. 88, no. 3, pp. 464–474, 1996.

THIS PAGE INTENTIONALLY LEFT BLANK

Initial Distribution List

1. Defense Technical Information Center
   Ft. Belvoir, Virginia

2. Dudley Knox Library
   Naval Postgraduate School
   Monterey, California